Investigation of ferroelectric domains and polar nanoregions in barium titanate oxide by Bragg coherent X-ray diffraction imaging

(Transfer report)

Department of Physics and Astronomy

University College London

University of London

Name: Jiecheng Diao

Supervisor: Ian Robinson

Date: Sept. 19th, 2021

Contents

Chapter 1. Principles of X-ray

X-rays conform with wave-particle duality in quantum physics, where both wave and particle (photon) properties can be quantified. Considering the wave properties, X-rays are a form of electromagnetic radiation and its frequency spans from 30PHz (10^{12}Hz) to 30EHz (10^{18}Hz) in the spectrum. They obey the general optical laws including reflection, refraction and diffraction. When considering the photon properties, X-rays can interact with matter by scattering (either elastic or inelastic) and absorption (fluorescence, photo-electron emission, Auger electrons). Important for experiments, X-rays can be counted.

Rontgen discovered the X-ray in 1895, which earned him the first Nobel prize in physics in 1901. Later on, Rontgen found the X-ray is produced by using high energy electrons to hit a material target. This is still the efficient way to produce X-ray, as the typical lab-based X-ray tube using electrons to hit copper anode for this purpose. There are two types of X-rays generated through hitting the atom: characteristic X-rays and bremsstrahlung. When an electron hit on an atom, it could knock out the electron at the inner shell. The outer shell electron would then fill the inner vacancy and emit X-ray radiation that is characteristic according to the element. This is the so-called characteristic X-ray, which was discovered by Barkla in 1909 and won the Nobel prize in 1917. An empirical law was put forward by Moseley in 1913, which describes the frequency of characteristic X-ray been proportional to the square of atomic number ($f \propto Z^2$). Different to characteristic X-ray, Bremsstrahlung radiation doesn't have a typical frequency, but rather a broad distribution. This is produced when the incoming electron is slowed down when hitting the atom rather than knocking out electron on shell. According to the energy conservation, the energy of emitted X-ray would be the same with the energy loss due to the slowing down of electron.

The high penetration property of X-ray was immediately exploited to take transmission photo for medical application after the discovery. Hongzhang Li is the first Chinese to take the X-ray photo, who was a Chinese diplomat visiting Germany at that time. He took the X-ray photo seven month after the discovery of X-ray, in which he saw a bullet directly in his left face. He wrote the first description of X-ray in Chinese: Clothes, flesh, blood, wood and stone are all gone away. The only thing left in photo are hardware and bones (凡衣服、血肉、木石诸质，尽化烟云；所留存镜中者，惟五金类及骨殖全副而已). He called this X-ray method "bone photography" in Chinese (照骨术). We now know that the photoelectric absorption of the X-ray beam is roughly proportional to the cube of atomic number and inverse cube of energy ($\tau \propto \left(\frac{Z}{E}\right)^3$). The harmful effect of X-ray to human tissues was gradually found, after cases of burns, hair loss and even death been reported due to continuous exposure to X-ray. Therefore, the static X-ray photo is usually performed instead of a dynamic one in modern medical radiography to reduce the exposure dose.

In this chapter, the scattering process is emphasized, which is directly linked to our present works.

1.1 X-ray Scattering

1.1.1 Classical scattering theory

Classical scattering is also termed as coherent scattering or Thomson scattering. As a transverse electromagnetic wave, X-ray can be diffracted to form constructive or

destructive interferences. The only essential particle that interacts with the X-ray is the electron (as discussed below). Diffractions from other sources, such as atom, molecule, crystal or glass, can be viewed as the geometric and mathematical combination of the electron scattering. Different form factors are also developed to mathematically deduce the relations, as shown in below.

(a) An electron

The classical way to evaluate the scattering from a free electron is to put it in the X-ray beam and treat it as radiation source by vibration. Then the amplitude and intensity at a given point is formed. The intensity per unit area per unit time is an observable quantity and given by the Thomson scattering equation:

$$I_e = I_0 r_0^2 P \tag{1.1}$$

I_0 is the intensity at electron source. P is the polarization factor. For unpolarized X-ray beam, this factor is $\frac{(1+cos^2\psi)}{2}$. r_0 is the classical radius, or Thomson scattering length, given by:

$$r_0 = \frac{e^2}{4\pi\varepsilon_0 mc^2} = 2.82 \times 10^{-5}\text{Å} \ \ (SI) \tag{1.2}$$

e is the elementary charge (1.602×10^{-19}C). m is the electron mass (9.109×10^{-31}kg). ε_0 is the permittivity of free space (8.854×10^{-12}F/m). c is speed of light (2.998×10^{8}m/s).

The first interesting fact is that the above equations prove the electron to be the only essential particle for diffracting X-rays, because the scattered intensity is direct proportional to charge and inverse proportional to the density mass. The neutron has no charge, so it will not scatter the incident X-ray. The proton has the same charge as electron, but the density mass is 1836 times bigger, making its scattering intensity 1836^2 times smaller.

The second interesting fact is that the Thomson scattering equation describes the total scattering from free electron. When consider the bounded electron in atom, the Thomson scattering equation still works. However, it split into coherent scattering part (Thomson scattering) and incoherent scattering part (Compton scattering).

$$I_e = I_{coh} + I_{Incoh} = I_e f^2 + I_e(1 - f^2) \tag{1.3}$$

f is the **scattering factor of an electron** and can be expressed as a function of scattering vector Q at point r:

$$f = \int \rho(r) e^{iQr} dv \tag{1.4}$$

Scattering vector is defined as:

$$Q = k_i - k_f \tag{1.5}$$

Here the $\rho(r)$ means the electron density inside the electron cloud, which can be thought of as a probability distribution. k_i and k_f are the incident and scattered wave vectors.

(b) An atom

The scattering from an atom with Z electrons can be viewed as a superposition of scattering from each electron. Therefore, the total coherent scattering can be expressed as:

$$I_{coh} = \sum_{j=1}^{Z} f_j^2 I_e = \left(\iint \rho_j(r) e^{iQr} dv \right)^2 I_e \tag{1.6}$$

The sum of these scattering factor from different electrons is usually defined as the **atomic form factor**, given by

$$f^0(Q) = \sum_{j=1}^{Z} f_j = \int \rho_a(r) e^{iQr} dr \tag{1.7}$$

Here the $\rho_a(r)$ means the electron density in the atom.

(c) A unit cell

Similarly, the scattering from a unit cell with Z atoms can be viewed as the sum of each atom. This will form a new factor called **unit cell structure factor**, given by:

$$F_u(Q) = \sum_{j=1}^{Z} f_j^0 = \int \rho_u(r) e^{iQr} dr \tag{1.8}$$

Here the $\rho_u(r)$ means the electron density in unit cell.

(d) A crystal

The interesting story happens in the scattering of a crystal, where it has periodic structure. A single electron has no periodicity, so is the atomic orbitals in one atom. The primitive unit cell will not have periodicity according to its definition. The lattice vector can be defined as:

$$R_n = n_1 a_1 + n_2 a_2 + n_3 a_3 \tag{1.9}$$

Due to the periodicity of the lattice, the **scattering factor of a crystal** can be factorized as the product of unit cell form factor and lattice sum:

$$F_c(Q) = \sum F_u(Q) e^{iQr} \sum e^{iQR_n} \tag{1.10}$$

The lattice sum is described by Bragg's law or Laue equation next, after which the unit cell form factor is discussed.

Bragg's law is first proposed by W.H. Bragg (the father) and W.L. Bragg (the son) in 1913, who won the Nobel prize in 1915 for determining crystal structure using X-ray. Figure 1.1 shows a typical diagram for illustrating Bragg's law. The incident X-ray beam is scattered by the plane of atoms. The optical path length difference (OPLD) for the scattering from two adjacent crystal planes is the function of d-spacing and incident angle. If the scattering from two adjacent crystal plane is in phase, or equivalently the OPLD equals to integer multiple of X-ray wavelength, then the constructive interference occurs and yields the strongest intensity. This relation is described by Bragg's equation:

$$L_{OPLD} = 2dsin\theta = n\lambda \tag{1.11}$$

For fulfil this equation, there is clearly an upper limit for the X-ray wavelength:

$$\lambda < 2d \tag{1.12}$$

Bragg's law only involves the lattice point in real space and the diffraction condition can be simply deduced from geometry. Therefore, it gives a clean image of how diffraction happens in the view point of crystal plane.

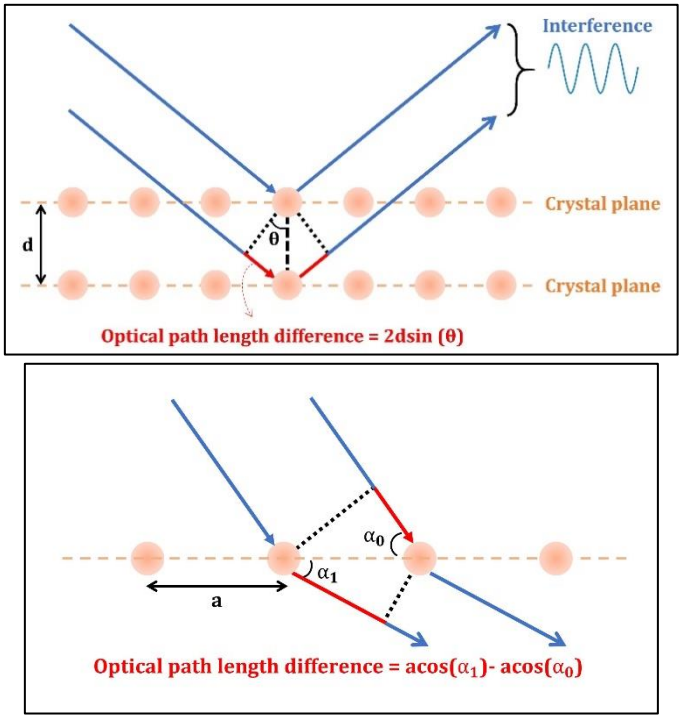

Figure 1.1. The schematic diagram to illustrate constructive diffraction condition. (a) Bragg geometry. (b) Laue geometry.

Laue deduced a similar relation between incident and diffracted X-ray beam, which is now termed as Laue equations. Laue also received Nobel prize in 1914 for the discovery of X-ray diffraction by crystals, one year ahead of Bragg. (This Nobel prize medal was dissolved by aqua regia in World War II and recast in 1952 using the same gold.)

A complete derivation of Laue's equations is shown in reference [1]. Here only a simple view of Laue's equation is given. From equation in X, the scattered intensity from a crystal is given by the multiplication of lattice sum and unit cell form factor. If only the lattice sum is considered, which is given by:

$$F_{l.s.} = \sum e^{iQR_n} \tag{1.13}$$

This equation would reach the maximum if

$$Q \cdot R_n = 2\pi x \ (x \ is \ integer) \tag{1.14}$$

Mathematically, a reciprocal space lattice can be generated similar to real space equation in:

$$G_m = mb_1 + m_2b_2 + m_3b_3 \tag{1.15}$$

The new lattice constants are defined as:

$$b_1 = 2\pi \frac{a_2 \times a_3}{a_1 \cdot (a_2 \times a_3)};\ b_2 = 2\pi \frac{a_3 \times a_1}{a_2 \cdot (a_3 \times a_1)};\ b_3 = 2\pi \frac{a_1 \times a_2}{a_3 \cdot (a_1 \times a_2)} \tag{1.16}$$

According to this definition, the real space and reciprocal space constant satisfy:

$$a_i \cdot b_i = 2\pi \ (i = 1,2,3) \tag{1.17}$$

This gives:

$$G_m \cdot R_n = 2\pi y \ (y \ is \ integer) \tag{1.18}$$

Combing the equation and gives the famous Laue condition:

$$Q = G \tag{1.19}$$

Figure 1.b is a schematic diagram for deriving Laue equation in one dimension. When the optical path length difference for the two adjacent atoms are the integer times of X-ray wavelength, then the diffracted X-rays are in phase and give constructive interference:

$$L_{OPLD} = a \cdot \cos\alpha_1 - a \cdot cos\alpha_0 = n\lambda \tag{1.20}$$

This equation can be expressed in vector view, which gives:

$$a \cdot \left(k_i - k_f\right) = a \cdot Q = h\lambda \tag{1.21}$$

This is the Laue equation in one dimension. The Bragg condition is a special case of Laue condition, where the Bragg's law can be deduced from Laue equation. Combining equations and proper multiplying the two sides gives

$$G^2 = 2k_i \cdot G = -2k_f G \tag{1.22}$$

Substituting G with Laue equation gives the Bragg's laws.

1.1.2 Other scattering effects

(a) Compton scattering

Compton scattering is one example of incoherent scattering or inelastic scattering. In such case, the scattered photon has lower energy or longer wavelength than the incident photon. This relationship is deduced by Compton in 1923:

$$\lambda_{in} - \lambda_{out} = \frac{h}{m_e c}(1 - cos\theta) \tag{1.23}$$

The Compton scattering length is defined from this equation as:

$$r_c = \frac{h}{m_e c} = 2.42 \times 10^{-2}\text{Å} \tag{1.24}$$

Sometimes the reduced the Compton scattering length is used, which involved replacing the Planck constant h in equation with reduced Planck constant $\hbar$. This gives a value of 3.86×10^{-3}Å.

Cross-section is a term to quantitatively describe the probability of a process happens during the collision of two particles. For example, the scattering cross-section can be defined as the possibility of an incoming photon been scattered by an atom. The scattering cross-section of barium element is given in Figure 1.2. At 9KeV, the Thomson scattering is still the major part that contribute to the total scattering. However, the Compton scattering cross-section exceeds Thomson scattering at about 100KeV.

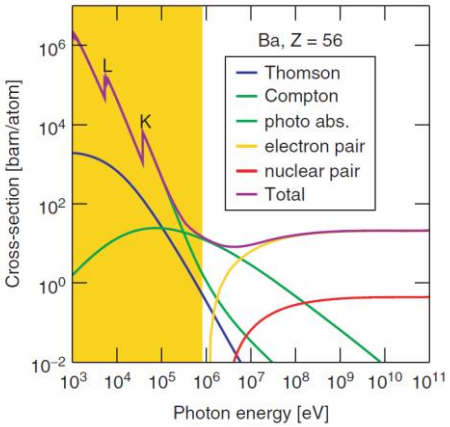

Figure 1.2. Cross-section of X-ray interaction with barium element. Image from [2].

(b) Debye-Waller factor

From a lattice dynamic point of view, the actual atoms in crystal have thermal vibrations instead of being static at lattice node. This fluctuation can be added into consideration by modifying the atomic form factor. The so-called Debye-Waller factor is usually added for compensating the thermal vibration, which takes the form of $e^{-\frac{Q^2\langle u^2\rangle}{3}}$. Q is the scattering vector and $\langle u^2\rangle$ is the mean square displacement from the scattering center. The value of Debye-Waller factor varies on temperature and atomic species.

1.2 X-ray sources and instrumentations

1.2.1 Lab X-ray source

Figure 1.3 shows a Rigaku Smartlab X-ray diffractometer at the UCL physics department. In X-ray tube, the tungsten filament first generates electrons upon heating. These electrons are then accelerated by electrical field towards the rotating copper anode. With a proper electron energy, X-ray comprising of a white radiation and characteristic radiations would be generated. Different monochromators can be applied to select the radiation needed. For example, Ge monochromator can be used on the incident beam side to select only Cu $K_{\alpha 1}$ radiation, which has an energy of 8.04KeV and a wavelength of 1.54056Å. Graphite single crystal monochromator can be applied on the receiving side to select both Cu $K_{\alpha 1}$ and $K_{\alpha 2}$ (λ=1.54439Å), but eliminating K_{β} (λ=1.39222Å) and most of Bremsstrahlung radiation. The vertical divergence of 0.01° is reached by a combination of a parabolically bent multi-layer mirror (Gobel mirror) and double crystal Ge monochromator. The horizontal divergence of 0.5° is achieved, which is determined by Soller slits. The length limiting slits are used to reduce the X-ray footprint.

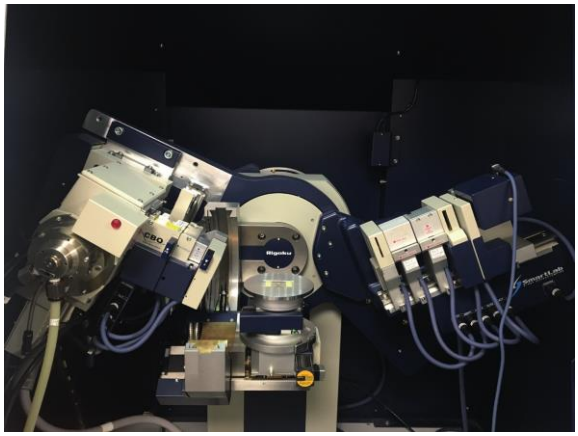

Figure 1.3. A photo of Rigaku X-ray diffractometer at UCL physics department.

1.2.2 Synchrotron radiation source

Synchrotron radiation has many unique properties comparing with lab X-ray, the most prominent ones being the tunability (freedom to choose the X-ray wavelength) and brilliance. Unlike the lab X-ray, synchrotron X-ray radiation is generated through the radically acceleration of relativistic electrons. There are approximately 70 synchrotrons in construction or in use worldwide.

The synchrotron radiation source has several key components: electron gun; linear accelerator (LINAC); booster ring; storage ring and beamline hutches. Same as lab X-ray, the electron gun uses heated filaments to generate electrons. The generated electrons are injected into linear accelerator, where the electrons are packed in bunches and accelerated to an order of hundred million electron volts. For example, the LINAC in the Advanced Photon Source (APS) is designed to accelerate electrons to 200MeV at 48 pulses per second. Then these electrons are put into the booster ring and further accelerated to the final designed energy. For example, Diamond Light Source (DLS) is a medium energy synchrotron working at 3GeV. European Synchrotron Radiation Facility (ESRF) and APS works at 6GeV and 7GeV, respectively. Booster ring originally works a few times per day to refill the storage ring, where the electrons are kept in a closed path and in operation to generate X-ray. For now, most synchrotrons use top-up mode, in which the booster ring works more frequently or continuously to provide constant beam current. The closed path can be usually divided into tens of segments, each contacting an arc path by bending magnets and a straight path used for insertion devices.

(a) Bending magnet

A bending magnet is used to create a homogeneous magnetic field over a distance, which mainly used to bend the trajectory of electrons to form a closed loop. It can also create a pencil beam in flattened cone shape.

First to be noted, the relativistic electrons moves at a speed close to the light. The Lorenz factor can be expressed as

$$\gamma = \frac{E}{mc^2} = 1957E \tag{1.25}$$

, where E is the storage ring energy. Therefore, for diamond light source, the Lorenz factor is about 5871.

Secondly, the relativistic Doppler effect changes the wavelength. The Doppler effect causes the sound wave more compact or an increase in frequency towards approaching the observer (red shift), comparing with a decrease in frequency when moving away from observer (blue shift). For the synchrotron electrons moving at a speed close to the speed of light, the doppler shift would modify the wavelength with an order of $(2\gamma)^{-1}$.

Thirdly, the Doppler effect also changes the radiation angle or the beam divergence. For relativistic electrons, the large Lorenz factor gives a small beam divergence in the order of γ^{-1}. This beam divergence defines the beam shape in the vertical direction. In the horizontal direction, there are electron angular changes which make the beam elongated horizontally.

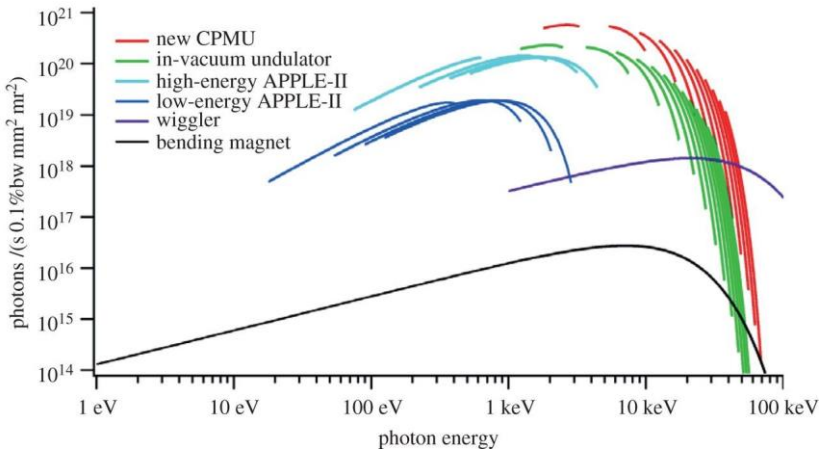

Figure 1.4. Bending magnets and insertion devices spectral. Image from [3].

The bending magnet offers radiation with a broad frequency but a lower brightness, as shown in Figure 1.4. Therefore, the bending magnets beamline is helpful when large energy range is favoured or the brightness is not the priority. For example, the APS 11-BM, which we use to do X-ray scattering and PDF study of BTO nanocrystal, is a bending magnet beamline.

(b) Insertion devices

Insertion devices are put in the straight path of the segment in a storage ring, which are the characteristics of third generation synchrotrons. The X-ray generated by the insertion devices are several orders of magnitude brighter than by the bending magnets, as can be seen in Figure 1.4. The two typical insertion devices are wiggler and undulator, both of which are made of a stack of magnets arrays. In both cases, the electrons are forced to vibrate horizontally through the insertion devices. The X-ray generated from each pair of magnets would add up in the forward direction, thus enhance the flux. The difference of a wiggler and an undulator is the degree of electron moved from their straight path.

For a wiggler, the electron is moved at an angle larger than the natural opening angle. Assuming the wiggler has N pair of magnets with same length and field, the generated radiations would be increased by a factor of 2N. Because such electron vibration happens in horizontal direction, the angular distribution is also increased by a factor of 2N horizontally.

For an undulator, the electron is moved with a degree smaller than the natural opening angle. In this case, the generated X-ray from each pair of magnets are in phase with each other. Therefore, the brightness is no longer the adding of intensity, but the square, due to adding amplitude.

1.2.3 Beamline optics

For different scientific purposes, various beamline optics could be applied.

Monochromator can be termed as an energy filter. The coherence application of X-ray requires all the beam to have the same wavelength or photon energy. The X-ray generated from an undulator is the pink beam and need to be filtered by a monochromator. Both APS 34-ID-C and DLS I13-1 use the Si (111) double crystal monochromator (DCM). It consists of two silicon crystals setting parallel to each other. The incident X-ray beam is diffracted by 111 Bragg reflection of silicon, where the X-ray with exact wavelength will be collected at Bragg condition. A second monochromator is used to both further filtering the energy and keep the X-ray beam to be straight. In the real case, the collimation of incident X-ray beam and crystal imperfection such as mosaicity would introduce the spread of X-ray beam, but silicon is close to perfect. The energy resolution for a typical Si (111) DCM is 2×10^{-4}.

As for focusing optics, because the real part of X-ray refractive index is small but very close to unity, it's hard to effectively bend the X-ray beam. The focal length for a conventional lens would be too large to be practical. To achieve the bending of X-ray so as to focus the beam, various methods have been developed by either refraction, total external reflection or diffraction.

(a) Compound refractive lens (CRL)

Because one conventional lens cannot substantially bend X-ray due to refractive index, one way to get around is to use many lenses. The European X-ray Free electron Laser (XFEL) Materials Imaging and Dynamic (MID) beamline uses two CRLs (primary lens stack CRL-1 and secondary lens stack CRL-2) to focus the X-ray beam. These CRLs are fabricated by drilling holes onto the beryllium block. The axes of these holes are coplanar and the beryllium are used for low X-ray absorption. The advantage of CRL is easy alignment, because it doesn't divert the X-ray beam. The disadvantage is that the absorption and intensity loss. CRLs are used widely in XFEL, where the brilliance is strong enough to compensate the loss. It's also used in synchrotrons like Diamond light source beamline I13-1.

(b) Kirkpatrick-Baez (K-B) mirrors

APS beamline 34-ID-C uses a pair of K-B mirrors to focus the pencil beam to around 600nm in both horizontal and vertical direction [4-5]. Figure 1.5 shows a diagram of K-B mirror pairs with two cylindrical mirrors [6]. The X-ray beam comes at grazing angle and is reflected by the two mirrors placing horizontally and vertically, respectively. The advantage of such design including decoupling of vertical and horizontal focusing, small intensity loss and easily manufactured.

(c) Parabolic/toroidal mirrors

Such two mirrors system can be reduced to one to minimize the length of mirror system. ESRF ID-09 use both parabolic and toroidal mirrors to focus the incident beam. Figure 1.5 shows a figure of the toroidal mirror used in ID-09, which has a light bending along

the beam path and strong bending perpendicular to the beam path. However, such bending surface is hard to manufacture and often induce aberrations.

(d) Fresnel zone plate (FZP)

FZP uses diffraction instead of reflection or refraction to focus the beam and is widely used in photography. FZP consists of numerous circular gratings which works like the famous Young's double slits experiment. The size of gratings can be controlled to be close to X-ray wavelength, so that the constructive interference can be achieved at a focal point downstream. The FZP has a good focal length which could go down to tens of nanometers. An order sorting aperture (OSA) is usually needed to define the beam after the FZP and before the sample. Diamond beamline I13-1 uses a 400um diameter FZP with 150nm outer zone width and 20um OSA downstream [8].

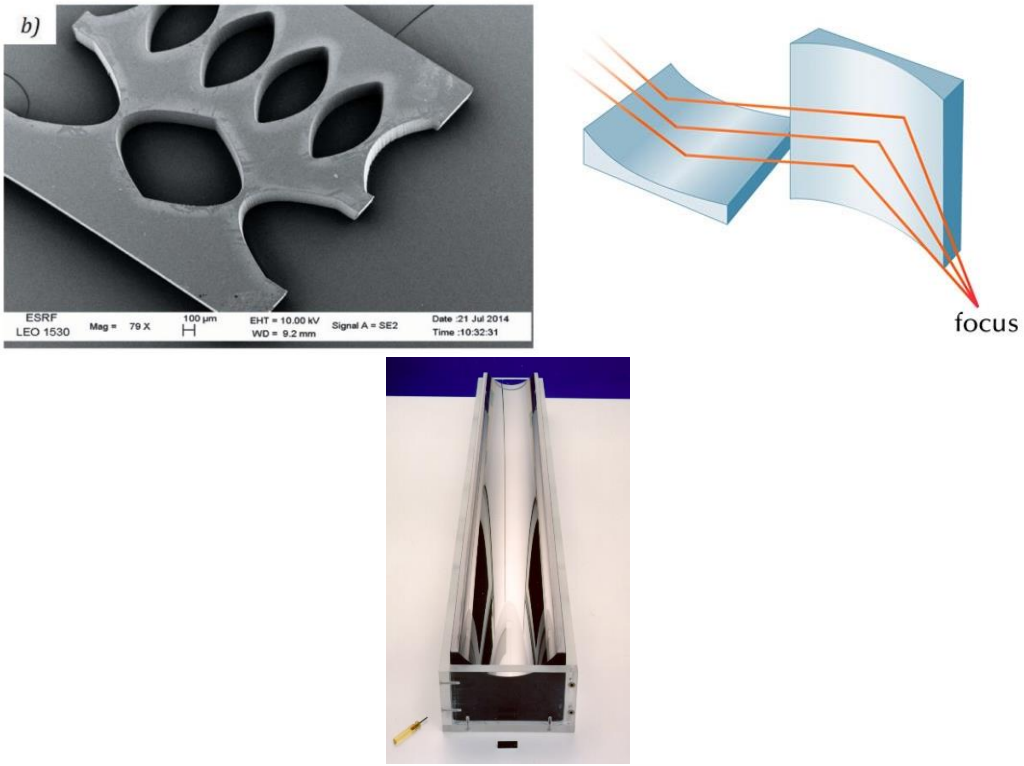

Figure 1.5. (a) CRL made on diamond plate at ESRF. Image from [7] (b) KB mirror pairs. (c) Toroidal mirror. Image from [9].

1.3 X-ray scattering at Rigaku Smartlab

With the development of X-ray sources, so is the X-ray based methods and techniques. We are interested in using Lab-based X-ray diffractometer to determine the structure and quality of $BaTiO_3$(BTO) thin film samples. Therefore, this section is focused on the thin film related scattering techniques: θ-2θ scans, rocking curve scan, small angle x-ray reflectivity scan and reciprocal space map. A manual for operating these scans are shown in appendix A.

(a) θ-2θ Scan

In this case, θ means the incident beam angle and 2θ means the diffracted beam angle. For a Rigaku Smartlab, the incident angle is ω instead. The 2θ and ω are moving in a symmetry manner relative to the sample stage. The offset ω angle is set beforehand and kept to compensate the sample surface plane angle. The standard epitaxial BTO thin

films have tetragonal structure at room temperature with c axis pointing out-of-plane and a axis in-plane. Therefore, the θ-2θ scan is along 00L direction in reciprocal space. The two important pieces of information from a θ-2θ scan are the peak position and full width half maximum (FWHM), which correspond to the out-of-plane lattice constant and sample thickness, respectively. The peak position is related to the out-of-plane lattice constant via Bragg's law, as shown in equation 1.11. The relation between FWHM of diffraction peak and sample thickness is derived in details and shown below.

Taking BTO thin film as an example and assuming there are N layers of d_{001}, which form a certain thickness. The signal measured from the detector are the amplitude of X-ray, which can be derived as:

$$|A(Q)| = \left| \sum_j e^{iQ \cdot r_j} \right| = \left| \sum_{j=0}^{N-1} e^{iQjd} \right| = \left| \frac{1 - e^{iQNd}}{1 - e^{iQd}} \right| = \frac{sin\frac{QNd}{2}}{sin\frac{Qd}{2}} \tag{1.26}$$

The amplitude will reach the maximum if the denominator of equation X equals to 0. This gives the condition for the peak centre position:

$$Q_1 = \frac{2\pi}{d} n \ (n \ is \ integer) \tag{1.27}$$

The amplitude will decrease to zero if the numerator equals to 0. This gives the condition for the end of the peak:

$$Q_2 = \frac{2\pi}{Nd} n \ (n \ is \ integer) \tag{1.28}$$

Therefore, the full width half maximum of the centre peak (named ΔQ), or the full width of the fringes gives the sample thickness Nd by

$$Nd = \frac{2\pi}{\Delta Q} \tag{1.29}$$

Next inverse this equation to real space. Assuming the two angles at full width half maximum are 1 and 2, then

$$\Delta Q = \frac{4\pi}{\lambda}(sin\theta_1 - sin\theta_2) = \frac{8\pi}{\lambda} \cos\theta \ sin\frac{\theta_{FWHM}}{2} \tag{1.30}$$

Therefore the sample thickness is given by:

$$Nd = \frac{\lambda}{4\cos\theta \ sin\frac{\theta_{FWHM}}{2}} \tag{1.31}$$

This is the general equation for the sample thickness in thin film sample. In the limit of approaching 0, the thickness is expressed as

$$Nd = \lim_{\theta \to 0} \frac{\lambda}{2\theta_{FWHM}\cos\theta} \tag{1.32}$$

This is similar to the Scherrer equation, which stated as:

$$\tau = \frac{K\lambda}{\theta_{FWHM}\cos\theta} \tag{1.33}$$

The Scherrer equation works for polycrystalline materials, where τ stands for the average grain size and K is a dimensionless shape factor to account for integration over a given crystal shape. It can be used to minimize the difference between experiment and prediction.

(b) Rocking curve scan

Rocking curve scan is a scan over ω with fixed 2θ. Therefore, the rocking curve scan can follow H00 or 0K0 direction according to the sample stage rotation angle ϕ. A simple rocking curve scan perpendicular to 00L direction contains the information of domain size. The domain size is the same discussed in θ-2θ scan above. The only difference is the direction has changed from 00L to either H00, 0K0, or something in between. If the domain sizes are close enough and regularly distributed, this periodicity will also show up in a rocking curve scan as the fringes.

(c) Reciprocal space map

Reciprocal space map (RSM) is two-dimensional (2D) map instead of one-dimensional (1D) scanning in the above two scans. Because the Rigaku Smartlab is equipped with 1D detector, this 2D mapping is acquired by a combination of θ-2θ scan and rocking curve scan, either H step with L scans or L step with H scans. L direction contains the out-of-plane information while H scan contains the in-plane information. Therefore, the RSM contains a combined information including out-of-plane lattice constant, in-plane lattice constant, in-plane domain periodicity, in-plane strain state.

(d) X-ray reflectivity

Small angle X-ray scattering is usually performed to measure the reflectivity of thin film sample. Due to the finite size effect, the resulting oscillations are related to the film thickness by:

$$\theta^2 - \theta_c^2 = N^2 \left(\frac{\lambda}{2d}\right)^2 \tag{1.34}$$

1.4 Bragg coherent X-ray diffraction imaging

The Coherent Diffraction Imaging (CDI) was first proposed by Sayre dating back to 1952 and Ian Robinson performed the first Bragg Coherent Diffraction Imaging (BCDI) experiment on Au nanoparticles in 1991 [10-11]. Through 20 years development, BCDI is now a powerful X-ray technique for investigating the structures of nanocrystals in three dimensions on the 30 nm resolution scale using third generation synchrotrons. The advantage of BCDI is its high sensitivity to the distribution of nanoscale strains inside the nanocrystal under investigation [12]. BCDI is a 3-D imaging method that is particularly valuable for probing the responses of individual nanosized crystal grains embedded in an in-situ environment, such as a polycrystalline material, a battery electrode or a working catalyst particle [13-15].

(1) Prerequisites

A BCDI experiment requires a coherent or partially coherent beam. The coherence of X-ray beam can be quantitatively determined by two coherence lengths: the longitudinal coherence length (temporal coherence length) and transverse coherence length (spatial coherence length). The longitudinal coherence length arises from the fact that the X-ray beam from the monochromator does not have a single wavelength, but rather a distribution over a range. The typical Si DCM working at (111) reflection, the

wavelength distribution $\Delta\lambda/\lambda$ is about 1.3×10^{-4}. This results in a 500nm longitudinal coherence length []. The transverse coherence length is due to the X-ray source not being point-like, so that the incoming X-ray is not purely plane wave. For a coherence beamline like DLS I13, this length is larger than 30um. In order to secure the coherence of incoming X-ray beam, the sample size should be smaller than the coherence length.

The other relevant length is the beam size, which can be adjusted by beam-defining slits and focusing optics. The slits are set to equal the transverse coherence length, and the beam can be focussed smaller afterwards. The sample size should be also smaller than the beam size in a BCDI experiment. For coherent optics, the focal size scales inversely with the entrance beam size, which can be adjusted for larger samples. Typical JJ slits sizes and beam sizes at sample stage at APS 34-ID-C are given in Table 1.1.

Table 1.1 Horizontal and vertical slit sizes and their corresponding focus size at sample stage. Value measured by Wonsuk Cha.

Horizontal slits (um)	Horizontal focus (nm)	Vertical slit (um)	Vertical focus (nm)
30	690	70	450
25	810	60	550
20	970	50	670
15	1270	40	840
10	2500	30	960
		20	1510
		15	1960
		10	3580

(2) Measurements

After illumination by the coherent beam, the diffraction pattern is collected by an area detector at the far-field position around a Bragg peak. Generally, this is done by rotating the sample stage in small steps and collecting 2D diffraction patterns, which are then stacked into a 3D diffraction pattern. The fringes surrounding a Bragg diffraction peak, due to the external shape of the crystals, can be oversampled with respect to their spatial Shannon—Nyquist frequency. A detailed BCDI experiment procedures can be found in Appendix B.

(3) Diffraction pattern treatment

Several treatments are usually performed to raw diffraction patterns before feeding into the reconstruction scripts. Firstly, the white field corrections are needed to cancel out the variation due to the detector pixel sensitivity to the X-ray radiation. For example, APS 34-ID-C uses ASI Quad (512x512) Timpix chips with GaAs absorber, which needs to be corrected using a white field. Secondly, a dark field correction is done to remove the bad pixels on the detector. Thirdly, unwanted noise or diffractions from other crystals are cropped out. Then the binning of raw data is sometimes needed to lower down the data size, so as to decrease the working load of phase retrieval. Finally, zero padding can be used to adjust the pattern array size, which is also the size of reconstructed object array.

(4) Phase retrieval

Because the detector in use only records the intensity of diffracted X-ray, which is the square of the amplitude, the phase information is lost in the measurement. To retrieve the missing phase, Sayre proposed to oversampled the diffraction pattern at a frequency finer than $1/2a$, where a is the sample size [13]. As long as the question is overdetermined, there are two effective ways to get the phase back: One is through iterative phasing algorithms, which involve Fourier transforms between real space and reciprocal space back and forth. Figure 1.6 shows a typical phase retrieval loop. In this work, all the reconstructions are done through iterative phasing method. The other method is through machine learning, which does not involve Fourier transform [16].

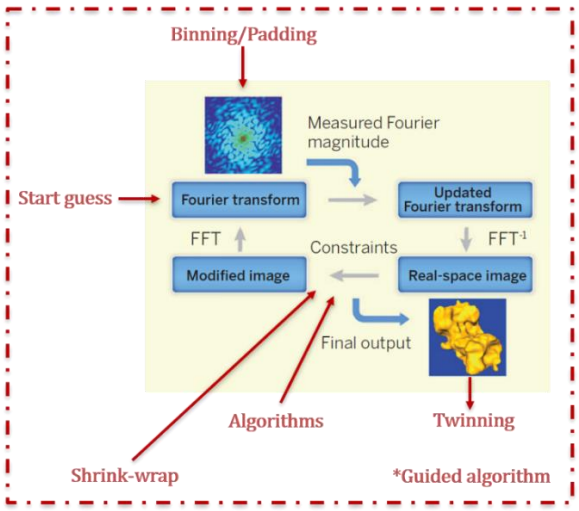

Figure 1.6. A schematic showing of iterative phasing loop. Image remade from [17].

The iterative phasing starts with a guess support, which is an initial guess of the crystal shape. A prior knowledge of the sample shape could aid the convergence of the solution. Without prior knowledge, it is normally set to be a box with half the array size as a flat start. The starting support can also be a random object with any phase. This can be used to test the reproducibility of reconstructed results by vary the starting support. The phase retrieval can also start from previous reconstructions or self-built support, which are used to deal with in-situ battery data and LBCO single crystal in our previous works.

After feeding into the loop, the initial support is transformed back and forth between two spaces while the constraints are applied. The reciprocal space constraint is the measured diffraction pattern amplitude, while keeping its phase. The real space constraint is where the different algorithms are applied. A list of algorithms available are listed in Appendix C. The two typical ones in use are Error Reduction (ER) algorithm and Hybrid Input-Output (HIO) algorithm. In the ER algorithm, the amplitude of reconstructed object is kept. The phase inside the object is also kept, but the amplitude and phase outside the support are set to 0. While in the HIO algorithm, such amplitude and phase are decreased by a factor rather than going to 0. Practically, different algorithms are combined together to help avoid stagnation at local minima. Figure 1.7 shows the error matrices changes through a combination of ER and HIO algorithms. Here the error matrices are defined in the reciprocal space, by comparing the measured diffraction pattern and the Fourier transform of the reconstructed objects:

$$\chi^2 = \frac{\sum_i ||A_{calc}(i)|^2 - |A_{meas}(i)|^2|}{\sum_i |A_{meas}(i)|^2} \tag{1.35}$$

A similar definition can be drawn to depict the difference between different reconstructions:

$$diff = \frac{\sum_i ||A_{calc1}(i)|^2 - |A_{calc2}(i)|^2|}{\sum_i |A_{calc1}(i)|^2} \tag{1.36}$$

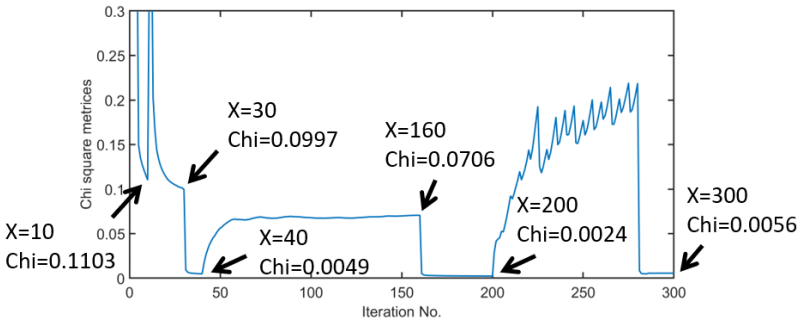

Figure 1.7 The error metrics of each iteration in a reconstruction using a combination of ER and HIO algorithms. The phasing starts with ER algorithm and triggers at iteration 10, 30, 40, 160, 201, 280.

Shrinkwrap (SW) can also be applied to help cropping out the low-density regions or noises in the reconstructed results. It is a way to periodically update the support. One way to achieve this is transforming the support into reciprocal space, doing convolution with a shape function (usually gaussian kernel) and then transforming back to real space. Figure 1.8a shows the SW thresholds and their corresponding error metrics of one crystal. The turning point is where the SW starts to cut the crystal. Figure 1.8b shows the difference between reconstructions using different SW threshold. The difference is big when SW has not touched the crystal, but becomes small when touching it. Figure 1.8c shows the reconstructed images of the crystals. When SW threshold is 0.05, there are noisy regions outside of crystal. With a threshold of 0.20 or 0.25, the crystal has well-defined facets. With even higher threshold, the reconstructed crystal starts to shrink and losing information.

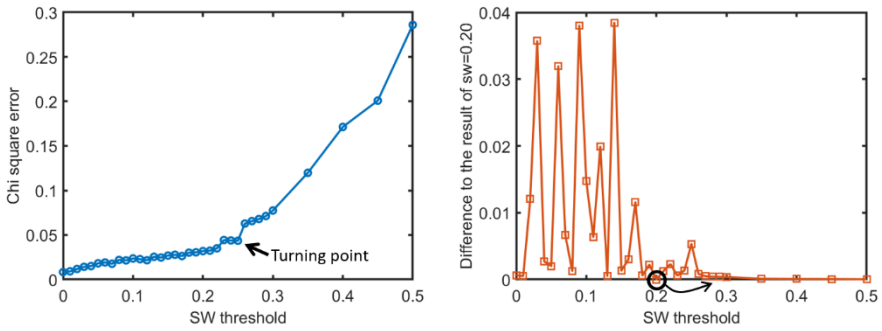

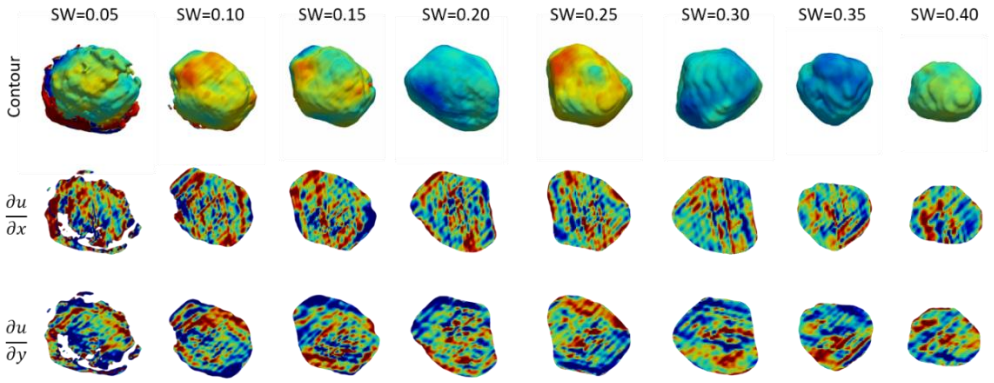

Figure 8. (a) Error matrices of reconstructions using different SW threshold. (b) Differences between reconstructions using different SW threshold. (c) The reconstructed images at different SW threshold.

Guided algorithms (GA) are also used in this work, which is schematic showed in Figure X. Instead of having one initial support, GA starts with several starting guess, or so-called populations. After each reconstruction block (called generations), it stopped and determine which is the best reconstruction result. The normally used criterions are chi square error matrices or sharpness. When the best result is determined, several supports are generated based on this result to feed into another generation and do reconstruction again. Low resolution method is usually used in first several generations to help reach the global minima faster.

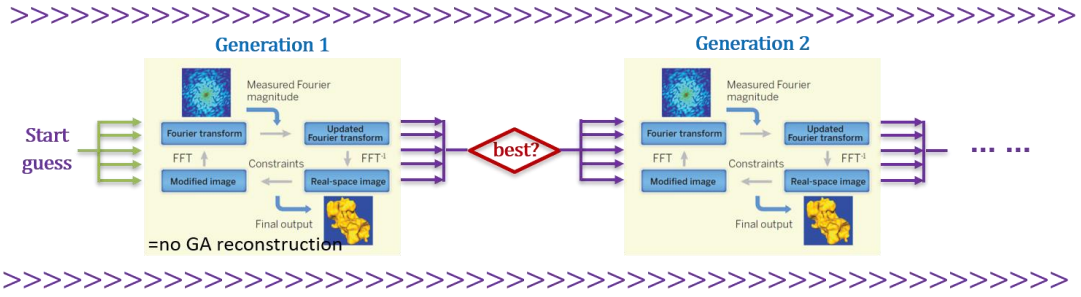

Figure 9. GA working flow. Image remade from [17].

The final reconstructed object is one set of the two conjugate results, as the two patterns with same amplitude and conjugate phase gives the same intensity. Therefore, the phase difference or derivative are more meaningful terms for discussion. In some cases when the phase range is over 2π, a script can be applied to unwrap the phase, based on its continuity in 2 or 3 dimensions.

To sum up, the phase retrieval is a case-to-case process. It works well for high-quality diffraction patterns, but for less good patterns some parameters may need to be optimized. Also, because the phase retrieval is prone to give multiple solutions, it's essential to always talk about the reconstructed results with their error metrics, usually the chi square defined above.

Reference

[1] J. Als-Nielsen and D. McMorrow, Wiley, New York, (2011). http://dx.doi.org/10.1002/9781119998365

[2] P. Willmott, Wiley, New York, (2011). http://dx.doi.org/10.1002/9781119970958

[3] G. Materlik, T. Rayment, D. I. Stuart, Phil. Trans. R. Soc. A, **373**, 20130161. (2015) http://dx.doi.org/10.1098/rsta.2013.0161

[4] X. Huang, M. Wojcik, N. Burdet, I. Peterson, G. R. Morrison, D. J. Vine, D. Legnini, R. Harder, Y. S. Chu and I. K. Robinson, Optics Express, **21**, 24038 (2012). https://doi.org/10.1364/oe.20.024038

[5] L. Li, Y. Xie, E. Maxey and R. Harder, Journal of Synchrotron Radiation, **26**, 220 (2019). https://doi.org/10.1107/S1600577518016697

[6] M. Ross, SLAC News (2011). https://www6.slac.stanford.edu/news/2011-10-11-kb-mirrors-harness-xrays-for-science.aspx

[7] Q. Zhang, M. Polikarpov, N. Klimova, H. B. Larsen, R. Mathiesen, H. Emerich, G. Thorkildsen, I. Snigireva and A. Snigiev, Journal of Synchrotron Radiation, **26**, 109 (2019). https://doi.org/10.1107/S1600577518014856

[8] D. J. Batey, S, Cipiccia, F. Van Assche, S. Vanheule, J. Vanmechelen, M. N. Boone, and C. Rau, Scientific Reports, **9**, 12278 (2019). https://doi.org/10.1038/s41598-019-48642-y

[9] ESRF ID09 website: http://www.esrf.eu/home/UsersAndScience/Experiments/CBS/ID09/OpticsHutch/mirror.html)

[10] D. Sayer, Acta Cryst., **5**, 843 (1952). https://doi.org/10.1107/S0365110X52002276

[11] I. K. Robinson, I. A. Vartanyants, G. J. Williams, M. A. Pfeizer, J. A. Pitney, Phys. Rev. Lett., **87**, 195505 (2001). https://doi.org/10.1103/PhysRevLett.87.195505

[12] I. Robinson and R. Harder, Nat. Mater., **8**, 291 (2009). https://doi.org/10.1038/nmat2400

[13] G. Xiong, O. Moutanabir, M. Reiche, R. Harder and I. Robinson, Adv. Mater., **26**, 7747 (2014). https://doi.org/10.1002/adma.201304511

[14] J. N. Clark, J. Ihli, A. S. Schenk, Y. -Y. Kim, A. N. Kulak, J. M. Campbell, G. Nisbet, F. C. Meldrum and I. Robinson, Nat. Mater., **14**, 780 (2015). https://doi.org/10.1038/nmat4320

[15] A. Ulvestad, A. Singer, J. N. Clark, H. M. Cho, J. W. Kim, R. Harder, J. Maser, Y. S. Meng and O. G. Shpyrko, Science, **348**, 1344 (2015). https://doi.org/10.1126/science.aaa1313

[16] L. Wu, P. Juhas, S. Yoo and I. Robinson, IUCrJ, **8**, 12 (2021). https://doi.org/10.1107/S2052252520013780

[17] J. Miao, T. Ishikawa, I. Robinson and M. Murnane, Science, **348**, 530 (2015) https://doi.org/doi/10.1126/science.aaa1394

Appendix

A. One set of procedures for alignment and measurement using Rigaku diffractometer

1. Alignment Procedure
   Steps:
   a. Control→Manual; Attenuator→Auto; All slits→0.03mm
   b. Determining Z-axis
      Moving θ/2θ, X, Y to 0
      Scanninging Z with range: ±1mm; Steps: 0.002mm; Normal Value: -1.78mm
   c. Determining ω-angle
      *Setting θ/2θ to 0.5°
      *Doing ω [-1°,1°] scan
      *Setting 2θ/ω to 0°
   d. Determining Z-axis again (Range: ±0.1mm; Steps: 0.002mm – half place)
   e. Determining Y-axis (Range: ±3mm; Steps: 0.01mm)
   f. Determining X-axis
      * Setting receiving slit to 0.3mm; Setting incidence slit to 0.5mm
      * Going to substrate Bragg angle
      (46.06° for DSO 110, 46.52° for STO, 45.52° for KTO, 45.22° for NSO)
      * Doing ω scan to adjust
      * Doing X scan with relative ±3mm
   g. Aligning Phi
      101 peak for 110 DSO [a'=3.94Å]: Chi=44.985°, 2th=32.069°;
      101 peak for 001 STO [a=3.905Å]: Chi=45°, 2th=32.397°;
      101 peak for 110 NSO [a'=4.010Å]: Chi=44.885°, 2th=31.565°;
      101 peak for 001 KTO [a=3.988Å]: Chi=45°, 2th=31.726°;

2. 2θ-ω scan
   Goal: Calculating average c lattice params and total thickness of thin film
   Way: Doing 2θ-ω scan with speed: 0.5°/min, range: absolute 15°-60°.

3. Rocking curve scan
   Goal: Assess the crystallinity of the sample (FWHM of a rocking curve peak)
   Way: Measuring intensity as a function of w (2θ fixed)
   2θ-ω goes to (001)/(002) interested film peak; ω scan in range of [-3°,3°] with speed: 0.5°/min, step:0.001°.

4. X-ray reflectivity
   Goal: Calculating thickness of thin film
   Way: Intensity oscillations have spacings related to the film thickness
   a. Setting θ/2θ to 0.5°
   b. Doing ω [-1°,1°] scan with speed 1°/min
   c. Doing 2θ-ω Absolute 0.1°-10°

5. Reciprocal space map
   Goal: Determine periodic domain structure, relaxation effect
   Way: In tetragonal, Qx(h=k) value of substrate and grown sample is same means coherent (no relaxation)
   STO 103 reflection origin: 2th=77.278°, w=57.074°;

NSO 103 reflection origin: 2th=73.6°, w=55.6°;

B. One set of procedures for doing BCDI at APS 34-ID-C

1. Optics alignment and preparation

The alignments of optics are usually done by the beamline staff prior to the user operation. Taking APS 34-ID-C as an example, the optics and equipment inside the experiment hutch are: Filter box → Fast shutter → JJ slit → KB mirror → Sample Stage → Vacuum X-ray Flight Path → Detector. In alignments, standard samples like Au are used. The slits and KB mirrors alignments can be down by scanning labx and check the intensity shape.

For making the BCDI measurement easier, the centre of rotation is also found in X and Y direction and marked in confocal microscope. This can be simply found by rotation the sample stage (theta). If there is no confocal microscope available and centre of rotation is not determined before the experiment, one can also find it using crystal diffraction by the following steps:

Changing theta angle a bit, then move LabX positive and negative to see the intensity change. If the intensity drops in both directions, then it's in the centre. If it drops one side and rise the other side, then it's misaligned and need to change LabY correspondingly:

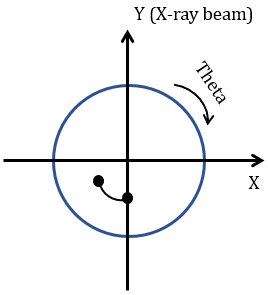

2. Sample mounting and set up experimental condition

Some general condition for an in-situ BCDI experiment includes temperature, voltage, pressure. We have tried heating, cooling and charging/discharging before at both APS 34-ID-C and I-13.

3. Sample flattening by using camera (X-ray eye) downstream

Aligning sample surface to be parallel to the X-ray beam. Generally, there are two ways to align.

Method 1:

(a) Set Phi=0°; Chi=90°; Theta=0°.

(b) Move SamZ to the position that just cutting the direct beam spot.

(c) Adjust Phi and tuning SamZ to make reflective spot and direct beam spot to coincide.

(d) Move Theta to 90°.

(e) Do (b) & (c) again, but this time adjust Chi instead of Phi.

Method 2:

(a) Set Phi=0°; Chi=90°; Theta=0°.

(b) Move SamZ to the position that just cutting the direct beam spot.

(c) Rotate Phi to completely cut direct beam spot at two side, phi1 and phi2, then change phi=phi1/phi2.

(d) Move Theta to 90°.

(e) Do (b) & (c) again, but this time adjust Chi instead of Phi

4. Adjusting centre of rotation

Moving the region of interest into the centre of rotation in confocal microscope in X and Y direction. The sample height, which is Z direction, is also adjusted in confocal microscope.

5. Setting up UB matrix (optional)

For going to multiple diffraction peaks of a single crystal, it's useful to set up the UB matrix before the measurement. This includes:

(a) Setting incident angle by "freeze" (may need "sigtau" to free the fixed flat angle).

(b) Setting up lattice constant and wavelength.

(c) Setting up or0 and or1.

6. Moving to designed Bragg angle and hunting for peaks.
7. Picking up Bragg peaks and doing rocking curve scan measurement.

C. Some useful spec commands are:

Command	Example / Explanation
wh	where motor position / angle is
wa	where all
lm	Limit
pa	display ub matrix
set_lm	*i.e. set_lm motor low high*
br / ubr	*i.e. br H K L*
ca	*i.e. ca H K L*
mv / umv	move motor directly
tw / umvr	move motor relatively *i.e. tw motor delta*
ct	Count
ascan / dscan (lup)	position scan. *i.e. ascan motor start finish intervals time*
hscan / kscan /lscan	scan in reciprocal space
do	do is to run a mac in command line. *i.e. do macroname.mac*
setmode	set fixing mode
setlat	set lattice constant
freeze	set freezing angle
setor0 / setor1	to set primary / secondary reflection of the UB matrix
or0 / or1	take current value in UB matrix

or_swap	swap values for primary and secondary vectors
savepos / save	save current position

APS 34-ID-C Special Command

ad_save_on / off	turn on / off saving data
cct 1	move diffraction pattern to the centre of ROI
align.mac	macro file to realign the position (usually labx, laby, labz and th)

NSLS2 4ID ISR Special Command

te	read or set the temperature
tscan / dtscan	temperature scan. *i.e. tscan start finish intervals time [sleep]; dtscan start finish intervals time [sleep]*

D. Algorithms available for phase retrieval

Algorithm	Description
ER	pn=pnm.*support #Using direct support
ERs	pn=amp_sqrt(pnm.*support,0.5) #Using half sqrt of support
ER-hist	#Lack histogram to run (histogram_constraint_v3)
ER-AMP	pn=amplitude_constraint(pnm,abs(pn));
SF	pn=(2*support-1).*pnm
SFa	amp=(sqrt(abs(2*support.*pnm))-sqrt(abs(pnm))).^2; pn=(2*support-1).*pnm ; pn=amp.*atan2(imag(pn),real(pn));
SF-h-ER	Make shift of SF/ER based on param.itno
ER-h-SF	
ER-SF-ER	
ERSF	
GPHIO	#Lack phase model to run(params.model_phase)
GHIO	pn=(pnm.*support)+(1-support).*(pn-beta*pnm)+.3*support.*(pn-pnm)
HIO	pn=(pnm.*support)+(1-support).*(pn-beta*pnm) #Explore area out of support
HIO-OR	pn=(1+beta*(lama-1))*pn+(beta-lama-beta*lama)*support.*pn-beta*lama*pnm+(1+beta)*lama*pnm.*support
HIO-ROR	lama=random('uniform',-.5,.5); pn=(1+beta*(lama-1))*pn+(beta-lama-beta*lama)*support.*pn-beta*lama*pnm+(1+beta)*lama*pnm.*support;

pcj-HIO	pnmpc=support.*phase_projector(pnm,params);
	pnpc=support.*phase_projector(pn,params);
	pn=pnmpc+pn-beta*pnm-pnpc+beta.*pnmpc;

HIO-hist	#Lack histogram to run (histogram_constraint_v3)
HIO-hist-sq	pnmpc=hist_squared(pnm,support); pnpc=hist_squared(pn,support); pn=pnmpc+pn-beta*pnm-pnpc+beta.*pnmpc;

HIO-AMP	pnmpc=amplitude_constraint(pnm,abs(pn));
	pnpc=amplitude_constraint(pn,abs(pn));
	pn=pnmpc+pn-beta*pnm-pnpc+beta.*pnmpc;

HIOb	pnmpc=amp_boost(pnm.*support); pnpc=amp_boost(pn.*support); pn=pnmpc+pn-beta*pnm-pnpc+beta.*pnmpc;
HIOs	pnmpc=amp_sqrt(pnm.*support,0.5); pnpc=amp_sqrt(pn.*support,0.5); pn=pnmpc+pn-beta*pnm-pnpc+beta.*pnmpc;

HIO-phgrd	pnmpc=phase_gradient_constraint(pnm.*support);
	pnpc=phase_gradient_constraint(pn.*support);
	pn=pnmpc+pn-beta*pnm-pnpc+beta.*pnmpc;

HIOp	pnmpc=amp_sqrt_perc(pnm.*support,0.5,.02); pnpc=amp_sqrt_perc(pn.*support,0.5,.02); pn=pnmpc+pn-beta*pnm-pnpc+beta.*pnmpc;
HIOv	pnmpc=amp_sqrt_val(pnm.*support,0.5,.75); pnpc=amp_sqrt_val(pn.*support,0.5,.75); pn=pnmpc+pn-beta*pnm-pnpc+beta.*pnmpc;
HIOso	if mod(params.itno,5) == 1 pnmpc=amp_sqrt(pnm.*support,0.5); pnpc=amp_sqrt(pn.*support,0.5); else pnmpc=pnm.*support; pnpc=pn.*support; end pn=pnmpc+pn-beta*pnm-pnpc+beta.*pnmpc; #Do HIOs or HIO
HIOsr	pnmpc=amp_sqrt(pnm.*support,0.75); pnpc=amp_sqrt(pn.*support,0.75); pn=pn+1*(pnmpc-beta*pnm-pnpc+beta.*pnmpc);
HIOd	pnmpc=amp_sqrt_th(pnm.*support,0.5); pnpc=amp_sqrt_th(pn.*support,0.5); pn=pnmpc+pn-beta*pnm-pnpc+beta.*pnmpc;

HIOsi	width=0.5; fact=params.itno/(width*params.iterations);
	if fact > 1,fact = 1;end if fact < 1,fact=0;end
	disp(num2str(fact));
	pnmpc=fact*pnm.*support+(1-fact)*amp_sqrt(pnm.*support,0.5);
	pnpc=fact*pn.*support+(1-fact)*amp_sqrt(pn.*support,0.5);
	pn=pn+.5*(pnmpc-beta*pnm-pnpc+beta.*pnmpc);

DM	pn=pn+pnm-pn.*support
DMr	pn=pn+.5*(pnm-pn.*support)
RAAR	pn=0.5*beta*((2*support-1).*(2*pnm-pn)+pn)+(1-beta)*pnm

RAARv	pnsm=grey_level_my_image(pnm.*support,6);
	pns=grey_level_my_image(pn.*support,6);
	pn=0.5*beta*(4*pnsm-2*pns-2*pnm+2*pn)+(1-beta)*pnm;

GRAAR	pn=0.5*beta*((2*support-1).*(2*pnm-pn+(pn-pnm))+pn)+(1-beta)*pnm
ASR	pn=0.5*((2*support-1).*(2*pnm-pn)+pn)
HPR	pn=0.5*((2*support-1).*(2*pnm-pn+(beta-1)*pnm)+pn+(1-beta)*pnm)

MEM	if params.itno ~= 1,
	dpn=abs((pnm-pn)).*support; epsilon=1/max(abs(dpn(:)));
	pn=pnm.*exp(-dpn*epsilon).*support;
	else pn=pnm.*support;

Chapter 2. Barium titanate oxide as a ferroelectric material

2.1 Polarization and ferroelectricity

2.1.1 A brief history

The understanding or even the discovery of the polarization related properties in materials takes a long time in history [1]. The pyroelectric phenomenon has been known for at least two thousand years, where it was first documented by the Greek philosopher Theophrastus [2-3]. The reason for this early discovery is that many natural materials show considerable pyroelectricity, such as tourmaline mineral [3]. The attempts to quantitatively study the pyroelectricity properties led to the discovery of piezoelectricity in 1880, when the Curie brothers realized the different pyroelectricity from uniform and non-uniform heating is caused by thermal stress [1,4]. The first ferroelectric material was reported in 1920, in which the polarization of Rochelle salt ($NaKC_4H_4O_6 \cdot 4H_2O$) was found to be reversible by external electric field [5]. But Rochelle salt has a complex structure containing four formula unit cells with 112 atoms, and it remained to be the only ferroelectric until the discovery of KH_2PO_4 (KDP) and its isomorphous crystals called KDP-ferroelectrics [6,7]. KDP series have a simpler crystal structure but involves hydrogen bond in the structure. Different possible arrangements of hydrogen lead to different orientation of (H_2PO_4) dipole units, so that the properties of KDP depends on the H-dynamic.

Theories were proposed to explain the origin of their ferroelectricity and many considered the hydrogen bond to be the essential condition for polar instability to give ferroelectricity [8-10]. However, this assumption was displaced with the discovery barium titanate ($BaTiO_3$, BTO) in the 1940s where no hydrogen bond exists in the crystal structure [11]. Due to the simplicity of its perovskite structure and its stability, BTO became one of the most studied ferroelectrics for decades. The big family of perovskite ferroelectrics also grew quickly, with $PbTiO_3$ (PTO) reported in 1950 and $Pb(Zr_xTi_{1-x})O_3$ (PZT) discovered in 1952 [12,13]. These materials remain to be the base materials for studying ferroelectricity until now. With the growth of the ferroelectric family, so followed the application of ferroelectric materials. BTO, for example, is widely used for its superior dielectric constant in the electronics industry. Recently, the ferroelectric random-access memory (FeRAM) has been developed for the low power usage and fast write performance. BTO is a suitable material for such kinds of application because it is both cheap and lead-free [14,15].

2.1.2 Structure origin of ferroelectricity

Before entering into a specific structure, it's interesting to revisit the definition of some crystallographic terms. These terms are well documented in textbooks of different fields, but sometimes used in a confused manner.

Table 2.1 Crystallographic terms and their definitions.

Terms	Definitions [16-18]
Crystal structure	Often shorten to be "structure". It's the atomic distribution within a crystal. Only when neglecting all possible defects in the structure, should we consider the periodicity defines the lattice of the structure.
Lattices	An infinite set of geometric points (known as lattice nodes) that represent the translational symmetry of an ideal crystal. The number of possible lattices is infinite.

Bravais lattices	Description of geometric arrangement of lattice points, and therefore the translational symmetry of the crystal. There are 14 Bravais lattices in three dimensions: simple cubic, body-centred cubic, face-centred cubic, etc…
Lattice systems (Lattice types)	A grouping of lattices according to the axial system. There are 7 lattice systems in three dimensions: triclinic, monoclinic, orthorhombic, tetragonal, rhombohedral, hexagonal, cubic.
Crystal systems	A classification of lattice according to the point group. There are 230 unique 3-D space groups. These crystallographic space groups can be sorted into 7 crystal systems: triclinic, monoclinic, orthorhombic, tetragonal, trigonal, hexagonal, cubic.
Crystal families	A combination of crystal systems. There are 6 crystal families in three dimensions: triclinic, monoclinic, orthorhombic, tetragonal, hexagonal, cubic.
Geometric crystal class	A classification of the symmetry groups of the external shape of macroscopic crystals. There are 32 geometric crystal classes in three dimensions.
Arithmetic crystal class	A combination of geometric crystal classes (32) and corresponding Bravais lattice types (14). There are 73 arithmetic crystal classes in three dimensions. For example, the tetragonal structure has 7 geometric crystal classes: 4, $\bar{4}$, $4/m$, 422, $4mm$, $\bar{4}m2$, $4/mmm$; It has two Bravais lattice types: Primitive (P) and Body centred (I); This combines to 16 arithmetic crystal classes: 4P, 4I, $\bar{4}P$, $\bar{4}I$, $4/mP$, $4/mI$, $422P$, $422I$, $4mmP$, $4mmI$, $\bar{4}2mP$, $\bar{4}m2P$, $\bar{4}m2I$, $\bar{4}2mI$, $4/mmmP$, $4/mmmI$.

Ferroelectricity is a characteristic of the crystal with two or more identical and spontaneous orientation states in the absence of electrical field. These orientation states, namely the electric polarization, can be reversed or change from one to another by an external electrical field. This reversibility of polarization is a unique feature of ferroelectricity, as all substances have electrostriction and could react to the field in a non-reversible manner. Of the 32 geometric crystal classes, 11 classes are centrosymmetric with no polar properties, therefore appear neither ferroelectric nor piezoelectric. In the remaining 21 non-centrosymmetric geometric crystal classes, 20 of them exhibit the piezoelectric effect, that is the charge-stress coupling phenomenon. In these 20 piezoelectric crystal classes, 10 of them have a unique polar axis with spontaneous polarization. Because these spontaneous polarizations are temperature dependent, the 10 crystal classes are termed as pyroelectric crystal classes. Ferroelectric crystal classes can be considered to be the subgroup of pyroelectric classes, as all ferroelectrics show pyroelectricity. However, it is suggested not to solely define ferroelectricity using a purely crystallographic definition because of the experimental limitations in two ways: 1) Polarization reversibility may not be seen even when a material is ferroelectric. For example, the crystal imperfections, the electric conductivities, the temperature and pressure all affect the reversibility of polarization. 2) Polarization reversal does not necessarily mean a material is a ferroelectric. For example, the polarization can arise from a metastable phase due to the temporary application of a switching field [1].

Perovskite ferroelectrics have a chemical formula of ABO_3, where A and B are cations. In perovskite structure, there is a semi-empirical relationship known as Goldsmith factor or tolerance factor[19]. It calculates the geometry of atoms in cubic phase as:

$$t = \frac{R_A + R_O}{\sqrt{2}(R_B + R_O)} \tag{2.1}$$

R_A and R_B are the radius of A-site, B-site and oxygen ionic radii, respectively. If the tolerance factor is bigger than 1, it means the B-site cation is relatively smaller than A-site, so that it has more free space to move around in its oxygen octahedral cage. This smaller B-site is usually related to high dielectric or ferroelectric properties [20]. If tolerance factor is equal to 1, it means the A-site and B-site match in size perfectly. If tolerance factor is smaller than 1, it represents a smaller A-site relative to B-site and the A cation can move around its cage of oxygen neighbours.

2.1.3 Phase transitions

From low temperature to high temperature, most ferroelectrics would go from low symmetry to high symmetry lattices, although in some cases the highest symmetry phase is not achieved before the melting point. BTO has a perovskite structure, where the titanium cation sits at B site in the oxygen octahedral shell. The phase transition is presented in Figure 2.1a, where it has a rhombohedral lattice (trigonal crystal system, R3m) at lower temperature, going into orthorhombic lattice (B2mm) at 203K, and then to tetragonal lattice (P4mm) at 278K, and finally goes into cubic lattice (Pm3m) at 393K [21]. The lattice constant changes over temperature are shown in Figure 2.1b [22]. Interestingly, there is a gap in transition temperature between heating and cooling down. Such a transition delay is usually seen in glasses, where the disorder system needs time and activation energy to cooperate with the transition. While in BTO, the disorder is believed to come from the different alignments of spontaneous polarization.

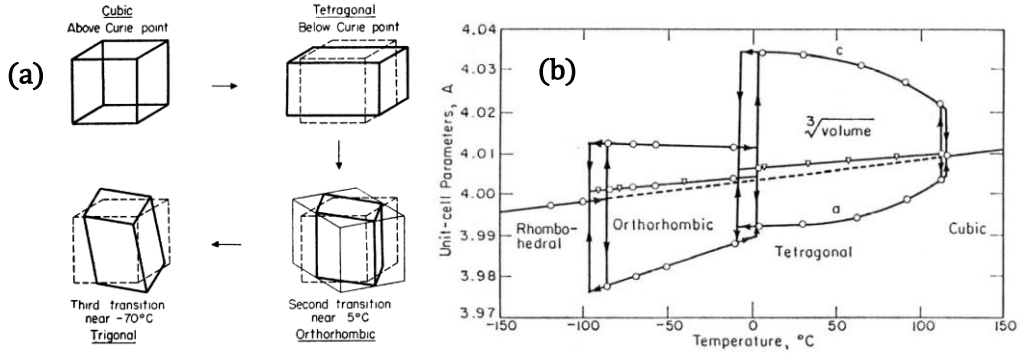

Figure 2.1 (a) Phase transitions of BTO. Image from [21]. (b) The changes of lattice constant with temperature. Image from [22].

The ample phase transitions with different crystal systems lead to various properties. BTO shows ferroelectricity in rhombohedral, orthorhombic and tetragonal lattice systems, which are all termed as ferroelectric phases. The polar axes for the three ferroelectric phases are crystallographic 111, 110 and 100, respectively. BTO has no ferroelectricity in its cubic phase, at least globally, which is termed a paraelectric phase because its polarization responds linearly to the applied field.

Different phase diagrams could be generated when varying one factor and controlling the others. Two examples are given in Figure 2.2. The first graph shows the phase transition temperature is decreased with the increase of pressure [23]. The second

graph shows the changes of Curie temperature with in-plane strain when the BTO thin film has the c-axis pointing out-of-plane [2]. The solid line is the result from thermodynamic calculations, while the points inside the graph are experimental result. This tetragonal-cubic phase transition could increase to more than 800K with a -1.7% in-plane strain. This substantial strain is acquired by carefully choosing the substrate lattice constant supporting a thin film and is hard to acquire in single crystal, where numerous mechanisms would happen to relax the large strain. There are also phase diagrams for domains, where different configurations of domain structures are of interest and mapped out [15].

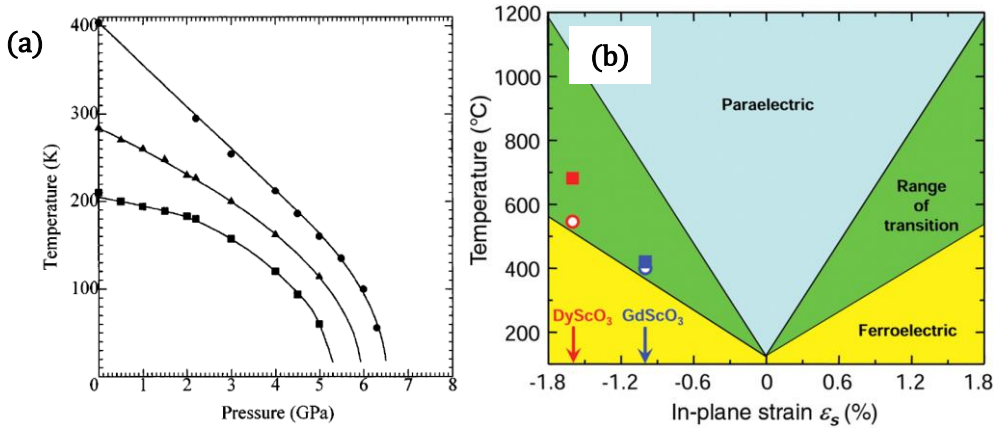

Figure 2.2 General phase diagrams of BTO. (a) Experimental phase transition temperature as a function of pressure. The solid lines are guide for eyes. Image from [23] (b) Thermodynamic calculated and experimental cubic-tetragonal phase transition temperature (Tc) of (001) BTO thin film under biaxial in-plane strain. Image from [24]. The circles represent the results from reactive molecular beam epitaxy (MBE), while the cube represent the results from pulse-laser decomposition (PLD). The red colour denotes the BTO thin film grown on $DyScO_3$ substrate, while the blue colour denotes the $GdScO_3$ substrate. Images from [24].

2.1.4 Soft mode

Microscopic models and lattice dynamics have helped to understand the nature of ferroelectric phase transitions. The structural phase transition is usually defined as being either "displacive" type and "order-disorder" type. There is a longstanding discussion in the scientific literature about the relative merits of both models.

(a) Displacive model

The displacive model is straightforward, given the simplicity of perovskite ABO_3 structure. In the displacive model, the Ti^{4+} cation is displaced off-centre within the O^{2-} anion octahedron. The phase transition occurs when this average position changes its symmetry. Figure 2.3 shows a typical image of how the Ti^{4+} displacement happens in BTO unit cells.

The basis of displacive model could track back to 1950, when Slater proposed there is a long-range dipole force tending to destabilize the local high-symmetric configuration [25]. Now the model is built on the lattice dynamics, where one lattice mode is considered to describe the displacive lattice instability [26]. Generally, there are three deformations to consider: long wavelength homogeneous deformations (zone centre acoustic modes); long wavelength inhomogeneous deformations (zone centre transverse optical modes); short wavelength deformations (zone boundary optical

modes). The long wavelength inhomogeneous mode involves the ionic motions of all constituent atoms, which is designated as the basic variable and is the so-called "soft mode" in a displacive phase transition.

When getting close to the phase transition temperature T_c, the frequency of this soft mode substantially decreases. This is why it is called soft mode or freezing mode. Microscopically, the restoring force of vibrating positive and negative ions are lost or weakened when approaching the T_c. Therefore, the ions are displaced to new off-centre positions. The reducing soft mode frequency is described by Cochran's law:

$$\omega_{TO}^2 = C(T - T_c) \tag{2.2}$$

C is a constant and is T_c is Curie temperature. In displacive model, the driving force of phase transition is the softening of the zone centre transverse optical mode.

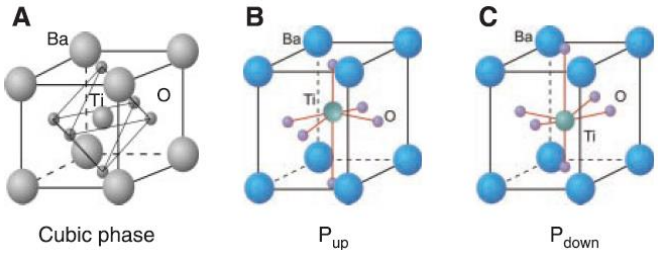

Figure 2.3 Typical crystal structure of BTO. (a) Cubic phase unit cell. (b) Tetragonal phase unit cell with Ti^{4+} displaced upward. (c) Tetragonal phase unit cell with Ti^{4+} displaced downward. Image from [27].

(b) Order disorder model

The order disorder model involves partially occupied sites and the symmetry of this occupancy. Figure 2.4 shows a typical eight-site order disorder model for BTO, which is proposed in 1968 by Comes [28,29]. In this model, the Ba^{2+} (A-site) and oxygen can be treated as static, while the Ti^{4+} (B-site) has eight crystallographic 111 positions to occupy. The phase transition occurs when the breaking of occupational symmetry starts to happen. In an order-disorder phase transition, the soft mode as described in displacive model (zone centre transverse optical mode) does not change with temperature. However, another central mode describing the relaxation type excitation becomes strongly temperature dependent and showing damping, which can be used as a signature of order disorder type in spectroscopy [30]. This central mode frequency is linked with dielectric constant via the Debye relaxation relation.

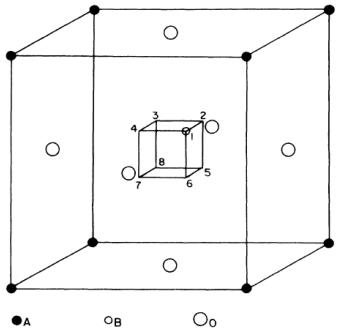

Figure 2.4 Eight site model in a BTO unit cell. Image from [29]

The phase transition in a specific ferroelectric can be one or a mixture of both types. For example, the ferroelectric transition in PTO is reported to be the pure displacive type [149]. Historically, BTO was thought to be a textbook displacive type ferroelectric. Now it is well accepted as a combination of displacive and order-disorder type material [31-33]. This is quite relevant to the local structure, which is discussed in details in Chapter 2.5.

2.1.5 Phenomenological theories

Phenomenological calculations based on Landau-Ginzburg-Devonshire has proven to be useful in studying ferroelectrics, such as predicting the phase transitions and describing temperature dependent properties. Most of the phase field simulations are also implicitly based on the continuum theory underlying the LGD theory. It is a purely macroscopic theory equivalent to mean field theory, where it averages out the long-range interactions and fluctuations to reduce a many-body problem to a one-body problem.

(a) Landau theory

Landau theory is a general theory for describing second-order phase transitions in 1937, but can also be extended to first-order phase transitions under external field as shown in later studies [34]. In Landau theory, the thermodynamic potential (or free energy, such as Gibbs free energy) of the system can be depicted as an analytic function of its order parameters, suitably defined. This function is then Taylor expanded in the form of different powers of order parameters near the phase transition temperature. This Taylor expansion only includes the even powers, as all the odd powers are omitted due to certain symmetries:

$$F(T,\eta) - F_0 = \frac{1}{2}a(T)\eta^2 + \frac{1}{4}b(T)\eta^4 + \frac{1}{6}c(T)\eta^6 + \cdots \qquad (2.3)$$

T is the temperature and η is the order parameter, which depicts the strength of perturbation linked to the structural change. This order parameter is constructed in such away the it is non-zero in the low symmetry phase and zero in the high symmetry phase.

The physical reason for this expansion is related to the soft mode described above. Because restoring force of a certain lattice mode becomes frozen or soft when approaching the phase transition, the amplitude of this mode becomes large enough to supress all other modes. The total energy is the sum of all lattice modes, as in the Debye theory. This total energy can be approximated as the expansion of the amplitude of just this soft mode when it becomes dominant [35].

(b) Landau-Ginzburg-Devonshire theory

Many extensions and applications of Landau theory have been proposed with regard to different systems. One of the famous extensions is Landau-Ginzburg theory, which serves as a mathematical description of superconductivity. The Landau theory was applied to describe ferroelectricity by Ginzburg in 1945 and Devonshire in 1949 independently [36]. Therefore, the developed phenomenological theory for ferroelectricity is called Landau-Ginzburg-Devonshire (LGD) theory. The crucial assumption for ferroelectrics, is to identify the order parameter as the polarization, thus the free energy can be written as:

$$F(T,P) - F_0(T) = \alpha_1 P^2(T) + \alpha_{11} P^4(T) + \alpha_{111} P^6(T) + \cdots - EP(T) \tag{2.4}$$

α_1 is temperature dependent, crossing zero at the phase transition, and usually takes the form of:

$$\alpha_1 = \frac{T - T_c}{2\varepsilon_0 C_0} \tag{2.5}$$

α_{11} and α_{111} are higher-order dielectric stiffness coefficients at constant stress.

When the electric field E=0, the polarization for the minimization of free energy can be calculated as

$$P^2(T) = \frac{-\alpha_{11} + \sqrt{\alpha_{11}^2 - 3\alpha_1 \alpha_{111}}}{3\alpha_{111}} \tag{2.6}$$

Notably, this is a simple form in one dimension and considering only the polarization to be the order parameter. To depict a real ferroelectric system, more quantities need to be added [37-39]. For example, the elastic strain accounts for a zone-centre acoustic mode which causes the phase transition. However, it is not associated with the softening of polarization related zone centre optical mode. These factors can be added directly to the free energy expression and treated as secondary order parameters, because they are independent of the primary order parameter. If the polarization in three dimensions, the lattice systems with specific atoms and grain shape are treated in details, then even more terms need to be considered [40,41]. In real case, certain modification of free energy expression is needed based on the question of interest.

2.1.6 Physical Properties

Both the soft mode theory and phenomenological LGD theory help to understand the properties of ferroelectric. Although the starting point is different, they do come to the same conclusion and show a inter connection.

(a) Dielectric property

The dielectric permitivity can be directly calculated from LGD theory. If only the second power of polarization is considered, then the expression for free energy can be written as:

$$F(T,P) - F_0(T) = \alpha_1 P^2(T) - EP(T) \tag{2.7}$$

The minimum free energy takes place at:

$$P(T) = \frac{1}{2\alpha_1} = \frac{\varepsilon_0 C_0}{T - T_c} E \tag{2.8}$$

The dielectric permittivity can be calculated as:

$$\varepsilon = \varepsilon_r \varepsilon_0 = (1 + \chi)\varepsilon_0 = \varepsilon_0 \left(1 + \frac{C_0}{T - T_c}\right) \tag{2.9}$$

The electric susceptibility in this equation is the famous Curie-Weiss law:

$$\chi = \frac{C_0}{T - T_c} \tag{2.10}$$

Figure 2.5a shows an example of the dielectric constant over temperature for BTO, where dielectric constant reaches 4500 at room temperature and reaches the maximum value at the Curie point [21]. However, this value is strongly dependent on the grain size and other factors, as illustrated later in this Chapter.

If the electric field is a harmonic alternating field, it can be expressed as:

$$E = E_0 e^{i\omega t} \tag{2.11}$$

Then the polarization is expressed as:

$$P = \varepsilon_0 \chi E_0 e^{i\omega t} = P_0 e^{i\omega t - \theta} \tag{2.12}$$

The ω means angular frequency and theta is the phase shift. The electric susceptibility in this case is also frequency dependent and complex. The real part and imaginary parts are called dielectric dispersion and dielectric loss, respectively.

The Curie-Weiss law can also be derived from the lattice dynamics point of view by either the displacive model or order-disorder model. Taking the displacive model as an example, according to Lyddane-Sachs-Teller relation [ref], the dielectric constants are connected to the optical phonon frequency:

$$\frac{\varepsilon_s(T)}{\varepsilon_\infty} = \frac{\omega_{LO}^2}{\omega_{TO}^2(T)} \tag{2.13}$$

The $\varepsilon_s(T)$ is static frequency of dielectric constant and ω_{TO} is transverse optical mode frequency, both of which will change with temperature. The ε_s is the high frequency dielectric constant and ω_{LO} is the longitudinal optical mode frequency, both of which can be viewed as constant over temperature. By substituting the equation 2.2, the Curie-Weiss law is obtained.

Ferroelectric materials behave similarly to ferromagnets in the sense of hysteretic behaviour. Figure 2.5b shows the hysteresis loop of BTO at room temperature [42,43]. When the external electrical field is applied to the sample, the inner spontaneous polarization will align accordingly and become parallel to the field when saturated. When this external field is removed, the polarization of a paraelectric material would decrease to zero. However, for ferroelectric material, the polarization would decrease to a nonzero value. Additional negative field is needed in order to switch the polarization direction. This hysteresis loop is also time-dependent. Figure 2.5c presents the hysteresis loops at different temperatures [42,44].

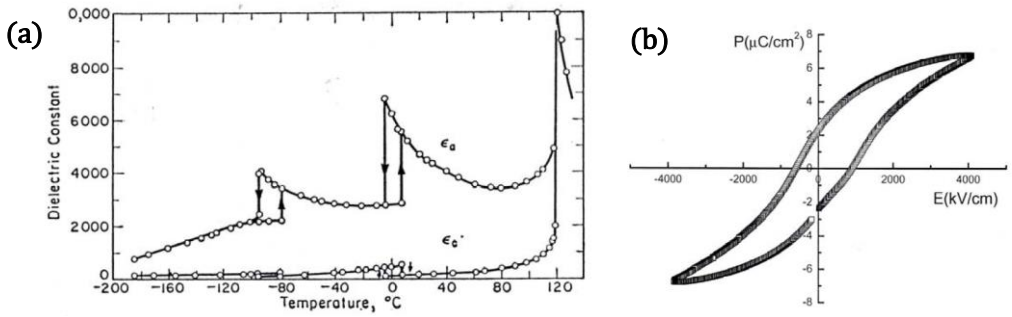

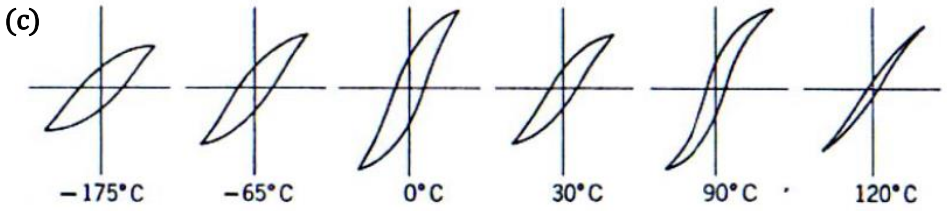

Figure 2.5 (a) The dielectric constant of BTO along a and c axes. Image from [21]. (b) BTO hysteresis loops at room temperature with high resolution. Image from [43]. (c) The change in BTO hysteresis loops with temperature. Image from [44].

(b) Piezoelectricity

Piezoelectricity quantifies the interaction between stress and electric field, measured as the derivative of polarization with respect to stress, of which the d_{33}component is the most important [27]. Some good piezoelectric performance materials are $Pb(Zr_xTi_{1-x})O_3$ (PZT, d_{33}=374pC/N) and relaxor type single crystal such as $(PbMg_{1/3}Nb_{2/3})_{1-x}$-$(PbTiO_3)_x$ (PMN-PT, d_{33}=1500pC/N) and $(PbZn_{1/3}Nb_{2/3})_{1-x}$-$(PbTiO_3)_x$ (PZN-PT, d_{33}=2200pC/N) [45-48]. Single crystal BTO, however, has modest piezoelectricity at room temperature with d_{33}=90pC/N along 001 crystal orientation, which is the polar axis in the tetragonal phase. A higher piezoelectricity with d_{33}=190pC/N can be achieved by applying a sufficiently large electric field along the 111 crystal orientation [49-51]. By heating the BTO crystal from room temperature to the tetragonal-cubic phase transition temperature, the d_{33} value rises from 90pC/N to nearly 350pC/N for 001 oriented BTO single crystals. While for 111 oriented BTO single crystals in the same temperature range, the d_{33} value decreases as temperature increases [50,52].

Recently, exceptional high piezoelectric BTO ceramics are prepared by different sintering techniques or hydrothermal synthesis. The d_{33} value can now reach 788pC/N, making it a promising candidate for lead-free piezoelectric applications [53,54]. It's generally believed that the grain size and the domains are responsible for these high piezoelectric responses, though there are controversial views of whether it is the domain wall or domain width that matters [55-58].

Stress and strain are second rank tensors with 9 coefficients. Due to symmetry, only 6 of 9 coefficients are independent. The strain, for example, is expressed as below:

$$\varepsilon = \begin{bmatrix} \varepsilon_{xx} & \varepsilon_{xy} & \varepsilon_{xz} \\ \varepsilon_{yx} & \varepsilon_{yy} & \varepsilon_{yz} \\ \varepsilon_{zx} & \varepsilon_{zy} & \varepsilon_{zz} \end{bmatrix} = \begin{bmatrix} \varepsilon_{xx} & \varepsilon_{xy} & \varepsilon_{xz} \\ 0 & \varepsilon_{yy} & \varepsilon_{yz} \\ 0 & 0 & \varepsilon_{zz} \end{bmatrix} = \begin{bmatrix} \frac{\partial u_x}{\partial x} & \frac{1}{2}\left(\frac{\partial u_x}{\partial y} + \frac{\partial u_y}{\partial x}\right) & \frac{1}{2}\left(\frac{\partial u_x}{\partial z} + \frac{\partial u_z}{\partial x}\right) \\ 0 & \frac{\partial u_y}{\partial y} & \frac{1}{2}\left(\frac{\partial u_y}{\partial z} + \frac{\partial u_z}{\partial y}\right) \\ 0 & 0 & \frac{\partial u_z}{\partial z} \end{bmatrix} \quad (2.14)$$

Such expression can also be written using number annotation:

$$\begin{bmatrix} \varepsilon_{xx} & \varepsilon_{xy} & \varepsilon_{xz} \\ 0 & \varepsilon_{yy} & \varepsilon_{yz} \\ 0 & 0 & \varepsilon_{zz} \end{bmatrix} \Rightarrow \begin{bmatrix} \varepsilon_1 \\ \varepsilon_2 \\ \varepsilon_3 \\ \varepsilon_4 \\ \varepsilon_5 \\ \varepsilon_6 \end{bmatrix} \quad (2.15)$$

Stress and strain are quantitatively connected as:

$$\begin{bmatrix}\sigma_1\\ \sigma_2\\ \sigma_3\\ \sigma_4\\ \sigma_5\\ \sigma_6\end{bmatrix}=\begin{bmatrix}Q_{11} & Q_{12} & Q_{13} & Q_{14} & Q_{15} & Q_{16}\\ Q_{21} & Q_{22} & Q_{23} & Q_{24} & Q_{25} & Q_{26}\\ Q_{31} & Q_{31} & Q_{33} & Q_{34} & Q_{35} & Q_{36}\\ Q_{41} & Q_{42} & Q_{43} & Q_{44} & Q_{45} & Q_{46}\\ Q_{51} & Q_{52} & Q_{53} & Q_{54} & Q_{55} & Q_{56}\\ Q_{61} & Q_{62} & Q_{63} & Q_{64} & Q_{65} & Q_{66}\end{bmatrix}\begin{bmatrix}\varepsilon_1\\ \varepsilon_2\\ \varepsilon_3\\ \varepsilon_4\\ \varepsilon_5\\ \varepsilon_6\end{bmatrix} \tag{2.16}$$

where the Q matrix is the stiffness matrix. A similar reversed expression would link the strain with stress by compliance matrix S. The relationship is $S = Q^{-1}$.

Piezoelectricity is a third rank tensor with 27 coefficients, but could only have 18 distinct coefficients because of the symmetry of strain. Without electrical field, the polarization can be expressed as applied stress:

$$\begin{bmatrix}P_1\\ P_2\\ P_3\end{bmatrix}=\begin{bmatrix}d_{11} & d_{12} & d_{13} & d_{14} & d_{15} & d_{16}\\ d_{21} & d_{22} & d_{23} & d_{24} & d_{25} & d_{26}\\ d_{31} & d_{32} & d_{33} & d_{34} & d_{35} & d_{36}\end{bmatrix}\begin{bmatrix}\sigma_1\\ \sigma_2\\ \sigma_3\\ \sigma_4\\ \sigma_5\\ \sigma_6\end{bmatrix} \tag{2.17}$$

P_1, P_2 and P_3 are polarization along crystallographic x, y and z direction. Such abbreviation writing of stress tensor also simplified the piezoelectric coefficients, like d_{31} connects polarization P_3 with stress tensor σ_1. This is the case where force is along x direction and the polarization is along c axis.

Similarly, without stress, the spontaneous strain can be express as applied electric field:

$$\begin{bmatrix}\sigma_1\\ \sigma_2\\ \sigma_3\\ \sigma_4\\ \sigma_5\\ \sigma_6\end{bmatrix}=\begin{bmatrix}d_{11} & d_{21} & d_{31}\\ d_{12} & d_{22} & d_{32}\\ d_{13} & d_{23} & d_{33}\\ d_{14} & d_{24} & d_{34}\\ d_{15} & d_{25} & d_{35}\\ d_{16} & d_{26} & d_{36}\end{bmatrix}\begin{bmatrix}E_1\\ E_2\\ E_3\end{bmatrix} \tag{2.18}$$

If further crystal symmetries are applied, then the independent piezoelectric coefficient would keep decreasing. For example, in cubic crystal lattice, all piezoelectric coefficients are zero. Considering the tetragonal BTO and picking up c-axis as the only polar axis, then the tensor matrix is simplified as:

$$\begin{bmatrix}P_1\\ P_2\\ P_3\end{bmatrix}=\begin{bmatrix}0 & 0 & 0 & 0 & d_{15} & 0\\ 0 & 0 & 0 & d_{24} & 0 & 0\\ d_{31} & d_{32} & d_{33} & 0 & 0 & 0\end{bmatrix}\begin{bmatrix}\sigma_1\\ \sigma_2\\ \sigma_3\\ \sigma_4\\ \sigma_5\\ \sigma_6\end{bmatrix} \tag{2.19}$$

Where d_{31}=d_{32} and d_{15}=d_{24}.

The physical meaning of these coefficients can be seen in Figure 2.6 [59].

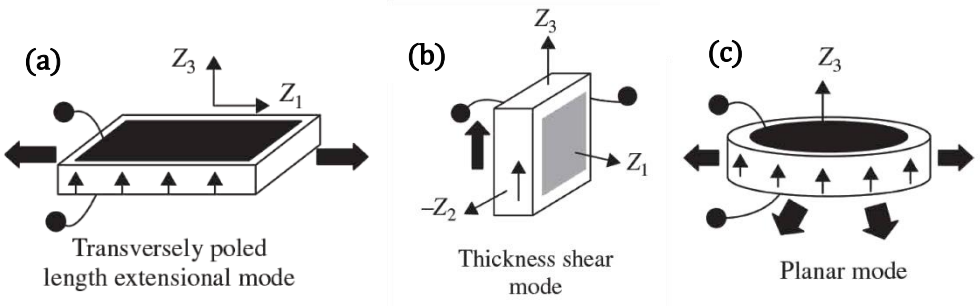

Figure 2.6 Measurements of different piezoelectric coefficient of a ceramic. (a) A measurement of coefficient d_{33}. Both applied stress and polarization measurement are taking along Z_3 axis. (b) A measurement of coefficient d_{31}. Stress is applied along Z_1 axis and the polarization is measured along Z_3 axis. (c) A measurement of coefficient d_{15}. Force direction is along Z_3 axis but force normal is Z_1 axis. The polarization is measured along Z_1 axis. Image from [59].

2.1.7 Influencing factors

As discussed above, the phase transition temperatures of BTO could vary a lot in literature, where various factors are reported to be influential. For example, the strain, pressure, the crystal size, and/or the perfection of the crystal could substantially change the transition temperature. This may take the form of different synthesis routes and processing techniques, which then involves defect chemistry, incorporation of foreign atoms, aggregation, porosity, residual stress and so on. It is possible that the influence is coming through the domain structure of the crystal, which is affected by all these factors, and so we are interested to discover the cause-effect relationships. Due to this complexity, it is not surprising that there are masses of scientific literature focused on this topic and sometimes it's hard to compare the exact value, given that different papers are using different samples. However, it's still useful to track the trend within each experiment, which would coincide with each other. Also, the dependent variables are intertwined themselves.

Taking the tetragonal-cubic phase transition as an example, the Gibbs energy of a ferroelectric system is written as a series power expansion of polarization, as stated in LGD theory:

$$G = G_0 + \frac{1}{2}\beta(T-\theta)P^2 + \frac{1}{4}\Upsilon P^4 + \frac{1}{6}\delta P^6 \tag{2.20}$$

G is Gibbs energy; P is polarization; β, Υ and δ are phenomenological coefficients; θ is Curie-Weiss temperature. The tetragonal distortion can be quantified as tetragonality, which can be described as the square of polarization:

$$\eta = \frac{c}{a} - 1 = kP_s^2 \tag{2.21}$$

$\frac{c}{a}$ is tetragonality, k is the difference of the electrostrictive coefficients $Q_{11} - Q_{12}$.

The Curie transition temperature is also related to polarization, therefore can be described by tetragonality:

$$\frac{Q}{T_c} = \frac{\beta}{2}P_s^2 + \frac{1}{4}\left(\frac{\partial \Upsilon}{\partial T}\right)P_s^4 = \frac{\beta}{2k}\eta + \frac{1}{4k^2}\left(\frac{\partial \Upsilon}{\partial T}\right)\eta^2 \tag{2.22}$$

Q is the heat of transition and T_c is the Curie temperature.

Through these equations, it can be seen that the tetragonality (or tetragonal related strain), the spontaneous polarization and Curie temperature are directly connected for a given system.

The most studied factor in BTO is the size effect. The grain-size effect has been reported for more than 60 years, when Kniepkamp and Heywang talking about the dielectric properties of polycrystalline BTO [60]. This size effect has been under intensive studied especially after 1990, when both the preparation and characterization methods were well developed for studying miniaturization of BTO grains. From equations above, the tetragonality, the Curie temperature and spontaneous polarization are coupled together, therefore they will change in a similar manner as the size decreases.

Tetragonality tends to show little change when the grain size is in or above micrometer size. When the grain size goes down to hundreds or tens of nanometer, the tetragonality would show a decreasing trend. Again, this decreasing curves with grain size varies from one study to another. Figure 2.7 shows the tetragonality of different BTO samples. The first graph shows the tetragonality for BTO single crystal remains the same from 1μm down to 0.3um, when it starts to decrease [61]. The lattice system goes into cubic when the size is 0.12um. The second graph shows another study of BTO fine crystal [62]. This time the crystal still shows tetragonality over 1.004 when size is about 40nm. The crystal goes into cubic phase suddenly when the size is 30nm or less. What temperature?

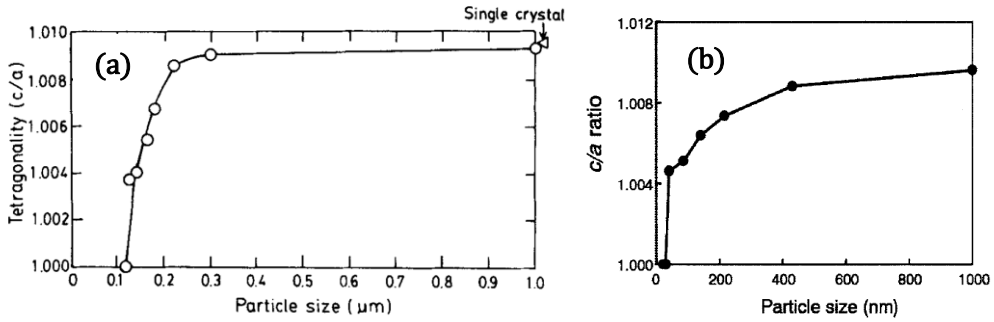

Figure 2.7 The tetragonality changes with particle size. Image from [61,62].

Curie temperature is expected to be connected to tetragonality, as explained above. As the particle size decreases at a given temperature, the tetragonality is seen to decrease as well, so it is expected that the Curie temperature will be lower for smaller particles too. Figure 2.8a shows the Curie temperature changes over tetragonality in BTO single crystal. When single crystal sizes go down to 0.12um, the Curie temperature decreases to about 70° [62].

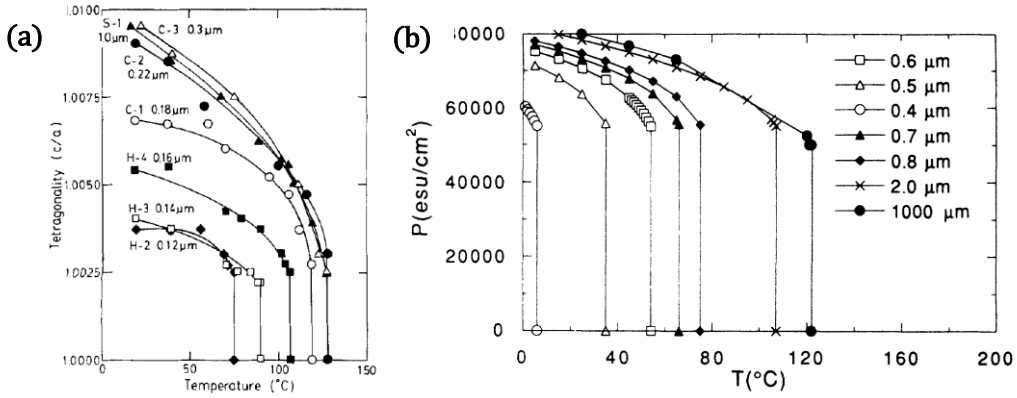

Figure 2.8 (a) Curie temperature differences and tetragonality difference as a function of grain size. Image from [61] (b) Polarization differences and Curie temperature difference as a function of different grain size. Image from [62].

Polarization also shows a decreasing tendency when the size goes down to sub micrometer range. Figure 2.8b shows the polarization as a function of crystal size and temperature. For this specific series of samples, the crystal with size of 0.4μm has no polarization at room temperature. When the size geos from 0.5μm to 2.0μm, the polarization increases from 66000esu/cm^2 to more than 80000esu/cm^2 [63].

The dielectric constant of BTO is found to increase when the size goes from bulk down to micrometers and reaches a maximum at about 1μm [64,65]. Temperature data of dielectric constant are shown in Figure 2.9 for particles of different sizes, decreasing from 1200nm to 50nm. Smaller grain BTO particles have smaller dielectric constant. There are different reasons to explain the appearance of an optimum size, all related to the nanoscale structure. A first view is that there is a bigger mobility of domain walls at this particular size that leads to a maximum dielectric constant [65,66]. A second view is that it's the twinning behaviour that determine the favourable size. When the crystal size decreases to micrometer, the minimization of residual strain results in a twinning structure becoming favorable. However, for the finest BTO crystals, with sizes down to hundreds of nanometer, the formation of domain wall becomes too costly compared to the volume transformation changes for transformation [67-69].

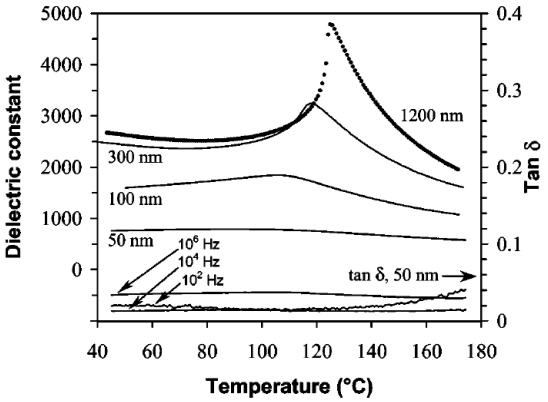

Figure 2.9 The changes of dielectric constant of BTO crystals of different grain size with temperature. Image from [67].

The optimum "critical" size is thought to be the smallest size when the BTO particle could still preserve ferroelectricity [148]. Though the idea itself is controversial, there

are supporting experimental results. As can be seen in the two examples in Figure 2.7, the critical sizes are 0.12μm and 30nm, respectively. The theoretical predicted critical length (thickness) for BTO thin film is 2.4nm [70]. There are several phenomenological reasons to explain the appearance of critical size:

1) Depolarization field could play a key role in this size dependent behaviour [71,72], unlike in the bulk crystal material, where numerous mechanisms exist to compensate the charge generated by polarization. When the crystal size keeps decreasing, it reaches a point where there is no way to compensate this charge. Then the depolarization field could be sufficiently strong for the crystal phase to become unstable. The depolarization field can be described as:
$$E = -\frac{L}{\varepsilon_0}P \tag{2.23}$$
The energy of depolarization field can be denoted as:
$$W = \frac{1}{2}\int \frac{\varepsilon}{\varepsilon_0}L^2P^2dV \tag{2.24}$$
2) Charged defects are inevitable for chemically prepared BTO samples, where the hydroxyl ion could reside as defects on oxygen sites and result in cation vacancies for charge compensation [73,74]. This can be confirmed by spectroscopy, in which the narrowly spaced infrared absorption bands are interpreted as the stretching mode for hydroxyl ions in the unit cell of tetragonal BTO [75,76]. Apparently, these charged defects could serve to stabilize the local polar ordering, and might be expected to disturb the phase transition.
3) The effect of elastic constraint could also make a play in this critical size effect. As described above, when the grain size decreases to sub-micron size, the crystals are substantially untwinned due to the increasing domain wall energy cost. From our BCDI experiments in Chapter 3 for the nominal 200nm BTO particles, the twin structure happens in less than one-seventh of the crystals. When the size goes to the limit, the transformation strain could be prevented even if there is a transformation driving force.

Anyway, the reasons behind the critical size haven't come to a consensus, which is one of our pursuits in the current and future studies.

2.2 Ferroelectric domain structure

"Domain" is a term to describe a region of crystal having the same order parameter. In ferroelectrics, this order parameter is spontaneous polarization. Before stepping into the specific domain structures, the techniques to visualize the domains are described first. The two most widely used techniques are scanning electron transmission microscopy (STEM) and piezoresponse force microscopy (PFM), both of which are good at dealing with thin film samples.

2.2.1 Characterization techniques

To map out the atomic polarization for thin film sample, high-angle annular dark-field (HAADF)-STEM is often performed, where an annular dark-field detector is put at high angle to measure the incoherently scattered electrons. Such intensity is proportional to the square of the atomic number (Z^2) with good accuracy [77], which is why HAADF is often called "Z-contrast" TEM. Two-dimensional (2D) gauss fitting is usually applied to determine the atom central position, by which the relative displacement between different types of atoms can be extracted.

HAADF-STEM images of typical perovskite $SrTiO_3$ (STO), $BaTiO_3$ (BTO) and $PbTiO_3$ (PTO) are shown in Figure 2.10. The atomic numbers for strontium, barium, lead and titanium are 38, 56, 82, 22, respectively. The strontium and titanium atomic number are closer, so that the contrast is less obvious. Both atoms, as ions, show bright spots in the STEM image and the oxygen ions can also be visible as dark points in Figure 2.10a [78]. The polarization direction can be described as the titanium atom displacement relative to oxygen.

Figure 2.10b presents the STEM image of BTO. The barium atomic number is twice larger than the titanium, thus barium atom appears to be much brighter than titanium in STEM image [79]. Although in some cases, the Ti-O columns can be clearly seen, but for the other conditions only barium and titanium ions can be identified with confidence. Therefore, it's more natural to compare the displacement between barium and titanium ions. The polarization is interpreted as being along the direction where the titanium ion is displaced relative to barium ion.

As for PTO shown in Figure 2.10c, lead atom number is nearly four times bigger than titanium, which make the contrast even larger [80]. In PTO, the valence s electrons of lead tend to form some directional bonding with oxygen p-orbital. As a result, the PbO_{12} cage has Pb-O bonding distances of 2.54Å, 2.80Å and 3.2Å. Titanium is also displaced within the TiO_6 octahedral cage with bonding distances of 1.78Å, 1.97Å, and 2.37Å [81]. The polarization direction is the lead ion displacement direction relative to titanium.

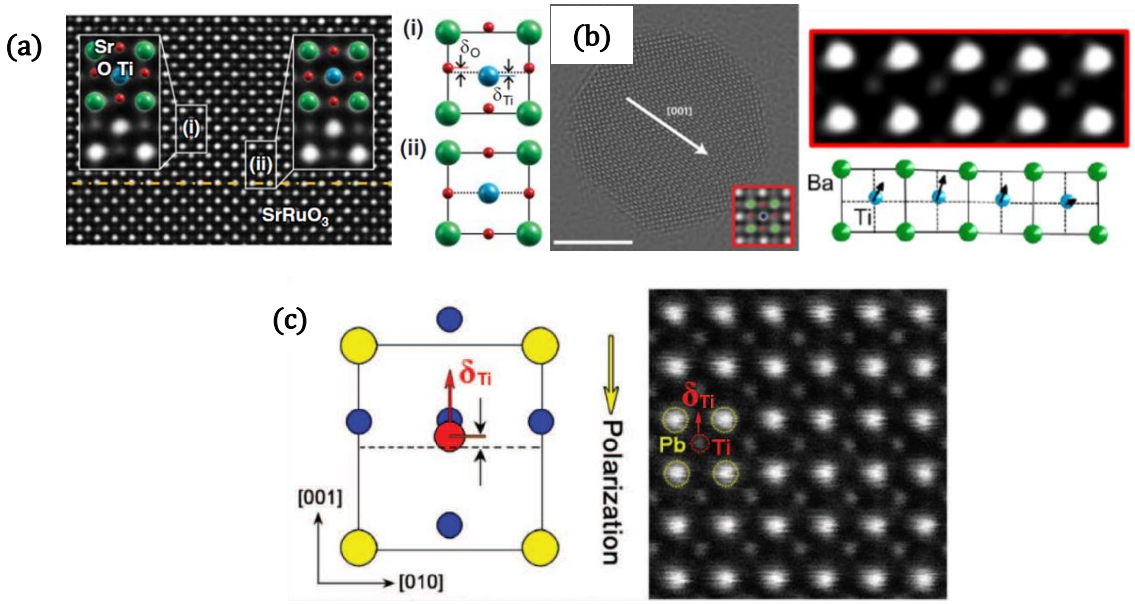

Figure 2.10 HAADF-STEM images of classical ferroelectrics. (a) STEM image of STO where the polarization can be identified as parallel to titanium displacement to oxygen. Image from [78]. (b) STEM image of BTO, where the polarization can be seen as parallel to the titanium displacement with respect to barium. Image from [79]. (c) STEM image of PTO, where the polarization is viewed as anti-parallel to the titanium displacement with respect to lead. Image from [80].

Gradient phase analysis (GPA) is a quantitative method to map out the displacement and strain field of crystal lattice based on high resolution STEM image. As illustrated in [82-84], GPA takes the advantages of both real-space and reciprocal-space information. The intensity distribution in a STEM image can be described as a Fourier series:

$$I(r) = \sum_{g} \left| H_g(r) e^{2\pi i \boldsymbol{g}*\boldsymbol{r}} \right| \tag{2.25}$$

$I(r)$ is the intensity of the STEM image at position r. g is the undistorted lattice reciprocal lattice vector, or the periodicity corresponding to the Bragg reflection. Practically, the operation is Fourier transform the STEM intensity image back to reciprocal space to get diffraction pattern. The Fourier coefficient $H_g(r)$ is a complex value where the phase is preserved in GPA. It can be viewed as the local Fourier component, can be obtained by Fourier filtering by:

$$H_g(r) = A_g(r) e^{iP_g(r)} \tag{2.26}$$

Amplitude $A_g(r)$ is associated with the local contrast of lattice fringe; Phase $P_g(r)$ is the lateral position of the lattice fringes. The phase $P_g(r)$ can be further deduced to describe the displacement field $u(r)$ by:

$$P_g(r) = 2\pi g \cdot u(r) \tag{2.27}$$

By measuring two phase images $P_{g1}(r)$ and $P_{g2}(r)$ from two non-colinear reciprocal space vectors g_1 and g_2, the two-dimensional displacement field $u_{2D}(r)$ can be fully determined as:

$$\boldsymbol{u}_{2D}(\boldsymbol{r}) = -\frac{1}{2\pi}\left(P_{g1}(\boldsymbol{r})a_1 + P_{g2}(\boldsymbol{r})a_2\right) \tag{2.28}$$

a_1 and a_2 are the real space lattice vector, as corresponding to the reciprocal space vector g_1 and g_2. If we project displacement field onto x direction ($\boldsymbol{u}_{2Dx}(\boldsymbol{r})$) and y direction ($\boldsymbol{u}_{2Dy}(\boldsymbol{r})$), then the 2D strain tensor can be further deduced as:

$$\varepsilon = \begin{bmatrix} \varepsilon_{xx} & \varepsilon_{xy} \\ \varepsilon_{yx} & \varepsilon_{yy} \end{bmatrix} = \begin{bmatrix} \dfrac{\partial \boldsymbol{u}_{2Dx}(\boldsymbol{r})}{\partial x} & \dfrac{\partial \boldsymbol{u}_{2Dx}(\boldsymbol{r})}{\partial y} \\ \dfrac{\partial \boldsymbol{u}_{2Dy}(\boldsymbol{r})}{\partial x} & \dfrac{\partial \boldsymbol{u}_{2Dy}(\boldsymbol{r})}{\partial y} \end{bmatrix} \tag{2.29}$$

Thus, the intensity distribution in a STEM image can be linked quantitatively to the displacement and strain field. Nowadays the GPA is a common plug-in in commercial TEM. Figure 2.11 shows the GPA study of an edge dislocation in silicon [83].

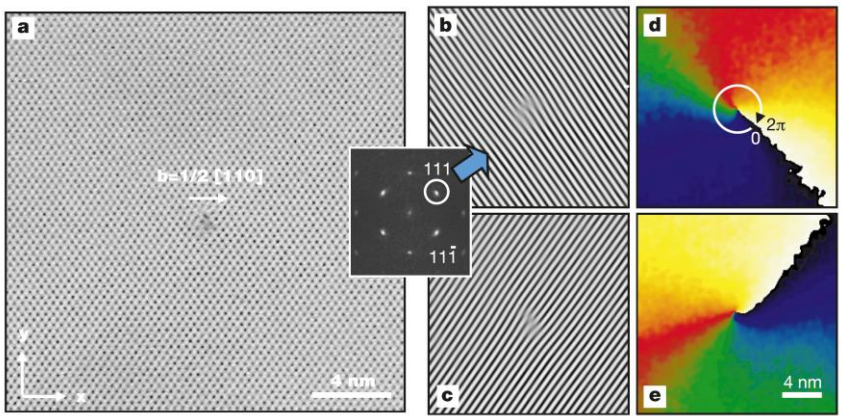

Figure 2.11 Geometric phase analysis of an edge dislocation. (a) High resolution electron microscope image in $1\bar{1}0$ *orientation. (b)* 110 *lattice fringes by Fourier filtering. (c)* $11\bar{1}$

lattice fringes by Fourier filtering. (d) Phase image of 110 lattice fringes. (e) Phase image of $11\bar{1}$ *lattice fringes. Image from [83].*

Another widely used method for looking at perovskite thin films is the Piezoresponse force microscope (PFM). It is one of the variants of the big Scanning Probe Microscopy (SPM) family including Atomic Force Microscopy (AFM) and Scanning Tunnelling Microscopy (STM). There are clear differences among those techniques: AFM is a mechanical detection method, where the tip-surface force is measured through the mechanical motion of cantilever [85,86]. There are many works presenting nice surface roughness images mapped out by AFM; STM is a current detection method, which is sensitive to tip-bias voltage; PFM is an electromechanical detection method, where an electric bias is generated by applying a current to the tip, and surface deformation is then captured.

PFM is first proposed by Gruverman in 1996, before which there are already some works proposing the principle of PFM in AFM and STM systems [87]. The most basic mode of PFM is the static mode, where a direct current is applied to the sample surface. The field induced strain along the field direction can be expressed as:

$$Z = \pm d_{33} V \tag{2.30}$$

where the domain will expand if the polar axis is along the field direction and contract if opposite.

Due to poor sensitivity to the static piezoresponse, the static mode has limited used in real cases. Instead, a dynamic mode is preferred, which uses an alternating current to increase the sensitivity by three orders of magnitude. This is now the 'basic' setup in commercial PFM. In such case, if the electric field is $V\cos(\omega t)$, then the first harmonic component of surface vibration (or surface piezoresponse) is measured in the form of amplitude $A\cos(\omega t+\phi)$. Figure 2.12 schematically shows the working modes of PFM including the vertical PFM (VPFM) and the lateral PFM (LPFM) [88].

For the VPFM, only the cantilever deflections are measured, which corresponds to the vertical (out-of-plane) force. Thus, the VPFM is sensitive to the polarization component that pointing out-of-plane. The amplitude of VPFM image can be expressed as $d_{33}V$, which is proportional to piezoelectric coefficient d_{33}. While the sign of phase in VPFM denotes the polarization direction of domains. The plus means the polarization is in the same direction with electric field, while the minus means opposite.

For the LPFM, only the torsion of the cantilever is measured, which relates to the in-plane polarization. The amplitude of VPFM image is linearly related to the shearing piezoelectric coefficient in the form of $d_{15}V$. The phase also means the direction. To map out the whole 3D polarization distribution, two perpendicular LPFM measurements are required, together with one VPFM measurement.

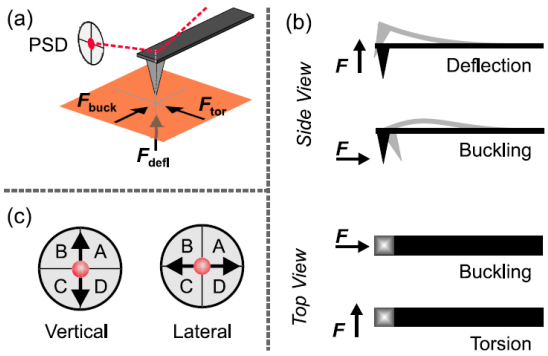

Figure 2.12 Possible movements of the cantilever due to forces acting on the tip. Image from [88].

However, in most real cases, the ferroelectric thin films are polycrystalline, containing domains that have different orientations. Under such condition, the amplitude map is coupled to all the piezoelectric coefficients that are relevant. To solve for the polarization in such conditions, it's useful to set up two sets of coordinates: tensor in laboratory coordinates d_{ij} and crystallographic coordinates d'_{ij}. They are connected with a general Euler rotation matrix (θ, ϕ, φ). For example, in tetragonal structure where the piezoelectric tensor is simplified in equation X.X, the response coefficient can be expressed as follows:

$$d_{33} = [(d'_{31} + d'_{15})sin^2\theta cos\theta + d'_{33}cos^3\theta]V \tag{2.31}$$

Again, PFM is only a qualitative method to image the domain configuration in thin film samples. Over decades, many advanced methods have been developed for better accuracy and signal-to-noise ratio (SNR). For example, in resonant mode, the cantilever working at a frequency close to its natural resonance can acquire a larger amplitude at a higher efficiency [89]. This resonance can be either predefined, or experimentally determined at every position before measurement using a feedback loop. This is the so-called Dual Amplitude Resonance Tracking method (DART) [88,90].

2.2.2 Classical domain structure in ferroelectric

The driving force of the domain formation is a pair of competing energies: the energy cost of the domain wall formation and the energy gain from domain formation [91]. The energy from domain formation E_1 can be expressed as:

$$E_1 = Uw \tag{2.32}$$

DEFINE SYMBOLS. If thin film is considered, where there is a one-dimensional size limitation, the wall energy density of unit area E_2 can be expressed as:

$$E_2 = \frac{\sigma d}{w} \tag{2.33}$$

The total energy is the sum of two terms, which is given by:

$$E = E_1 + E_2 = Uw + \frac{\sigma d}{w} \tag{2.34}$$

This total energy reaches the equilibrium at

$$\frac{dE}{dw} = 0 \tag{2.35}$$

This gives the relation:

$$w^2 = \frac{\sigma d}{U} \tag{2.36}$$

Here, the w means the domain width or domain size; the d means the sample thickness in thin film sample; U is energy volume density (constant); σ is the energy density of domain wall (constant). Kittel first proposed this square-root relation of domain size to thin film thickness in magnetic system, where the U stands for magnetostatic energy volume density [92,93]. Mitsui and Furuichi applied this equation in ferroelectrics, in which the U stands for electric energy density per unit volume [94]. Now this square-root relation is widely termed as Kittel's law. Notably, the above equation is a simplified version of the derivation of Kittel's law. If a specific system is treated, more accurate expression of U can be formed. For example, Kittel's law for 180° domain stripes can be expressed as [95]:

$$w^2 = \frac{\pi^3 \varepsilon_0 \left(1 + \sqrt{\varepsilon_x \varepsilon_z}\right)}{8.42 P^2} \sigma d \tag{2.37}$$

ε_0 is the dielectric constant of vacuum, ε_x and ε_z are the dielectric constants along a and c axes, respectively.

The Kittel's law is derived for thin films where two dimensions are infinite, but found to be universal in other geometries. An extension of Kittel's law to single crystal can be made with the assumption that the crystal is a cube with six parallel facets. This is shown as follow:

$$w^2 = \frac{\sqrt{2}\sigma}{2\left(\frac{U_x}{d_x} + \frac{U_y}{d_y} + \frac{U_z}{d_z}\right)} \tag{2.38}$$

Here, the $U_i (i = x, y, z)$ means the contributions of volume energy density from the domain facets along i direction. The size of a domain along the i'th direction is denoted as $d_i (i = x, y, z)$. This square-root relation could work as a guideline for the domain size, but does not mean to be quantitative or accurate. In a real sample, a deviation from this square-root relation is commonly seen, where the sample size and shape are reported to make a big difference [96,97].

Generally, the domain walls that are formed in ferroelectrics can be divided into two types: pure ferroelectric domain walls and ferroelastic domain walls. The pure ferroelectric domain walls separate 180° domains, where the polarizations between adjacent domains are anti-parallel to each other, as shown in Figure 2.13a. The ferroleastic domain walls are also ferroelectric, but involve changes of elastic strain upon formation. The ferroelastic domain walls are structurally the same as twin boundaries, where the two adjacent domains have mirror symmetry near the domain wall. The types of ferroelastic domain walls are determined by lattice system, not the specific atoms. For the Perovskite tetragonal phase, only 90° ferroelastic domain is allowed; for the orthorhombic phase, 60°, 90° and 120° ferroelastic domains are allowed. As for rhombohedral phase, 71° and 109° domains can be formed. These angles are commonly used for naming the ferroelastic domain walls, however, the angle is approximate with an accuracy of ~1° because it is based on the exact lattice parameters of the material. In BTO for example, if the lattice constants are set to be a=3.99Å and c=4.03Å, then the exact ferroelastic angles are [98]

$$\alpha = arctran\left(\frac{c}{a}\right) = 90.57° \text{ or } \beta = 180° - \alpha = 89.43° \quad (2.39)$$

Figure 2.13b shows a sketch of 90° ferroelastic domains in tetragonal lattice.

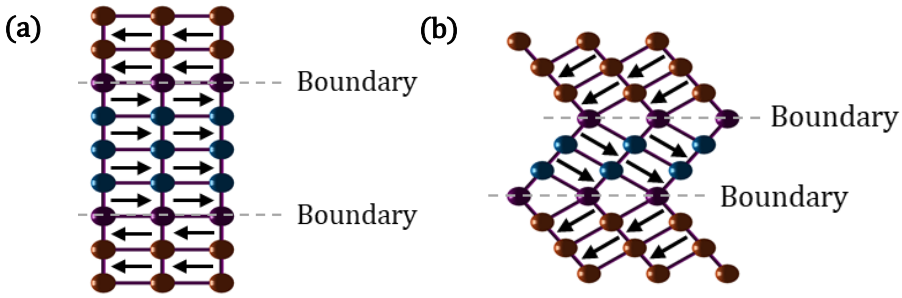

Figure 2.13 Sketches of domain wall. (a) 180° domain walls (b) 90° domain walls.

In thin film samples, where the boundary conditions can be carefully tuned, the domain configuration in-plane and out-of-plane is of great interest and leads to the so-called domain engineering. This interesting topic will be discussed further below in our future plans section.

2.2.3 Flux-closure domains and vortices

Recently, there has been a trend to locate and quantify new topological structures in ferroelectrics, which are the equivalent of important magnetic analogue configurations, because these may have great potential for functional electronic devices [73]. Topological structures are caused by manipulation of local degrees of freedom (DOFs) such as lattice, charge, spin and orbit. In ferroelectrics, however, the spin and orbit DOFs do not make any noticeable contributions, so the DOFs of these systems are dominated by lattice and charge DOFs. These freedoms are linked with energy, where the lattice DOF is the competition of elastic energy, while the charge DOF consists of electrostatic energy and polarization gradient energy [100,101]. To form a flux-closure domain, theoretical works suggest the depolarization field plays a key role. Under large residual depolarization fields, which is equivalent to poorly screened charge conditions, classical polydomains are favoured, such as 90° and 180° domains in tetragonal BTO. If the depolarization field is too small, the material is effectively screened and the monodomain is favoured. Therefore, to form a rotational polarization domain, a proper depolarization field is required [102,103].

Although vortices have been well studied in magnetic materials, their equivalent polar vortices in ferroelectrics are poorly understood. Even the existence of polar vortices or it's prerequisite flux-closure domain were debatable and used to be a big unknown question. The initial theoretical study that supported the existence of flux-closure domains was published only in 2004 [102]. This used first-principles Monte Carlo simulation to study the polarization field in PZT films under a residual depolarization field and a pretty large compressive strain (-2.65%), as shown in Figure 2.14. Under such strict conditions, the authors managed to see polar vortices in the side view. In 3D, these vortices build up uniform lateral vortex tubes. Ivan et al. also uses *ab initio* simulations to study PZT nanodisk and nanorod confined structures, in which they found vortices at 64K [104].

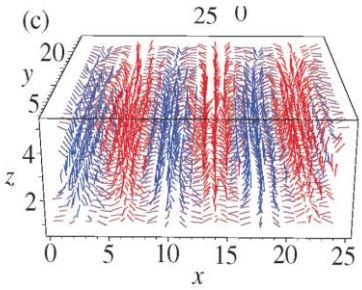

Figure 2.14 Simulated polarization in PZT thin film under -2.65% compressive strain. Image from [102].

After these theoretical predictions, some indirect experimental results followed. For example, in 2009, BTO nanodots with self-defined stripes were reported using TEM, as shown in Figure 2.15 [105]. These BTO nanodots are created by focused ion beam (FIB) milling of a bulk single BTO crystal. The author tried to explain these stripe features as some hierarchical twin boundaries that oriented in a self-confined way.

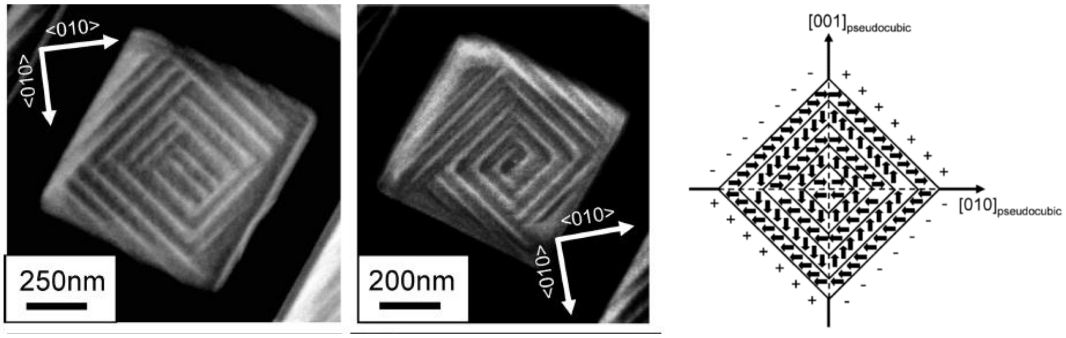

Figure 2.15 HAADF-STEM image of BTO nanodots and a sketch for possible domain configuration. Image from [105]

Rodriguez *et al* reported characteristic features of PZT nanodots via PFM also in 2009, as shown in Figure 2.16 [106]. They also build a nanodot of 7.6nm × 2.4nm in size with -0.9% compressive strain and simulated their VPFM and LPFM image. Such resemblance between experimental results and simulation suggests a possibility of vortices.

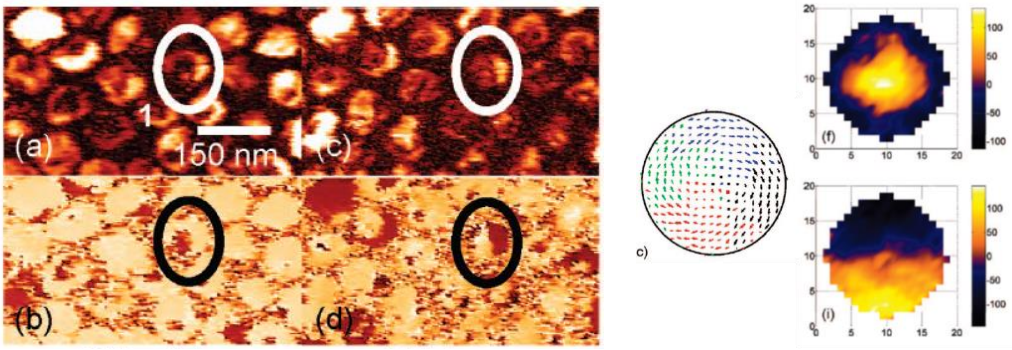

Figure 2.16 The left graph is the PFM results of BTO nanodots. (a) VPFM amplitude image; (b) VPFM phase image; (c) LPFM amplitude image; (d) LPFM phase image. The right graph is the simulation results, including the polarization order, the VPFM amplitude and LPFM phase. Image from [106]

In 2010, McGilly *et al* reported possible vortices in BTO lamellae, where two arrays of twin domains form a zigzag structure at interface [107]. Such a zigzag structure is

obvious in STEM image in Figure 2.17, but it failed to show up in the corresponding PFM image.

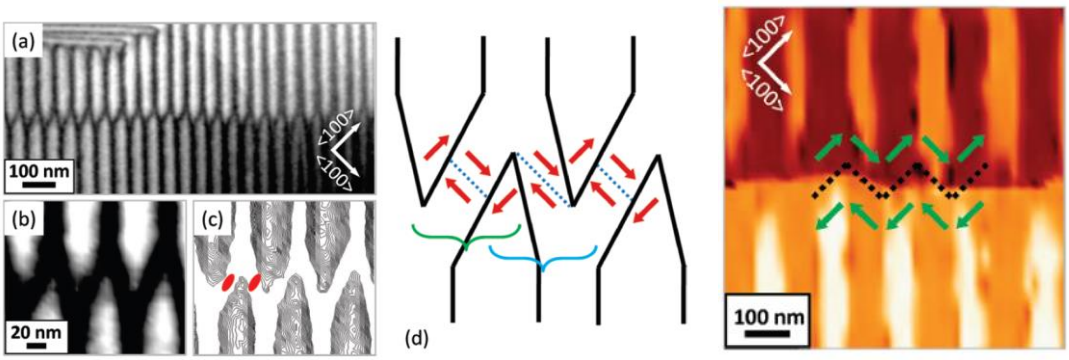

Figure 2.17 The left graph shows the STEM image of the zigzag structure. The middle graph shows a sketch of the polarization order at interface. The right graph shows the PFM image. Image from [107]

Later in 2010, the same group reported seeing flux closure domain with sizes up to micrometers [108]. Figure 2.18a shows the LPFM result on BTO lamella. This single crystal had been fully switched to a-c domains by application of sufficient electrical field. After the electric field was removed, they found the domain structures in BTO relaxed gradually. Figure 2.18b shows LPFM of a partially relaxed structure, where 180° in-plane domains are forming. After relaxing the sample for a few hours, the structure gradually evolved into that shown in Figure 2.18c. In two orthogonal LPFM images, four-fold flux closure domains can be seen.

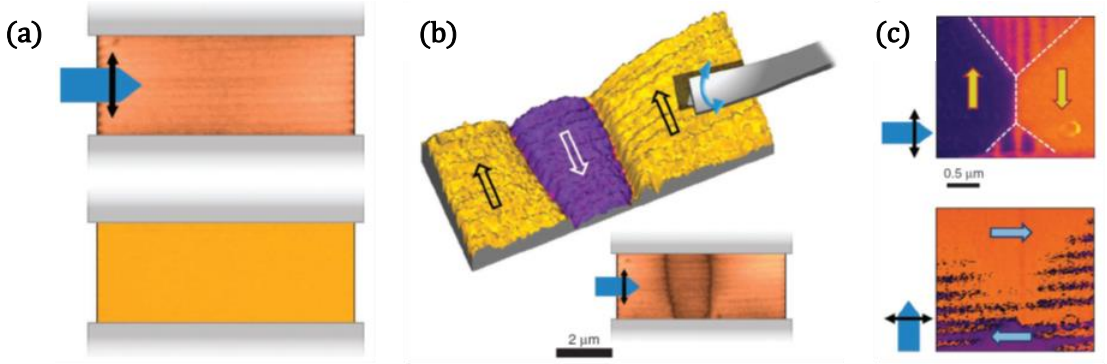

Figure 2.18 (a) LPFM result of BTO lamella. (b) LPFM of a partially relaxed BTO lamella. (c) LPFM image of BTO lamella after several hours of relaxation. Image from [108]

A further breakthrough came in 2011. Taking advantage of HAADF-STEM, directional views of flux-closure domains were obtained with sub-angstrom resolution. Figure 2.19 shows the TEM image of a typical flux closure domain in a $BiFeO_3$ (BFO) thin film grown on $TbSsO_3$ (TSO) substrate. BFO has an orthorhombic structure at room temperature, so the elastic domains are 109° relative to each other. Figure 2.19a shows one 109° domain. Figure 2.19b show a complete flux-closure domain, consisting of two 109° elastic domain walls and two 180° electrical domain walls [109]. Although such structures show little curvature of polarization except at the boundary, which is still far different from vortices, it is still a breakthrough to see that a flux closure domain can be formed by carefully selecting the materials and construction them into complex multidomain arrangements. A similar work is also published that year, shown in Figure

2.19c [110], is a three-fold vortex measured in a PZT thin film. Although in the title the authors called it a continuous electric dipole rotation, actually the only place seen to be rotating is the small block on the bottom.

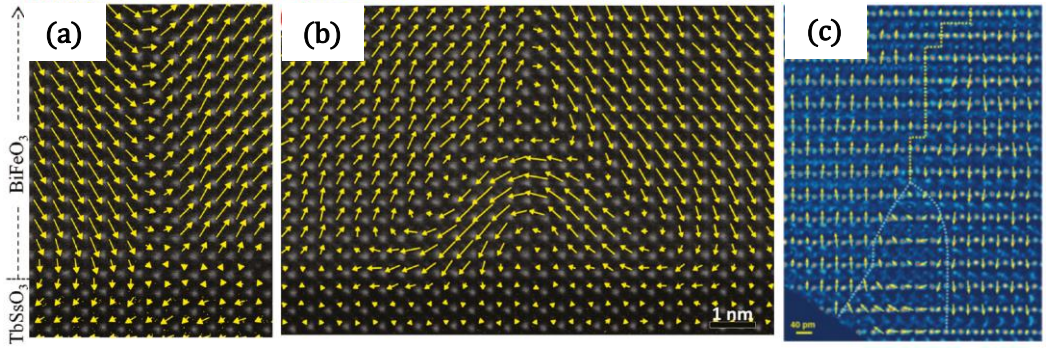

Figure 2.19 HAADF-STEM image showing flux-closure domains. Images from [109,110]

In 2015, flux-closure domains in PTO were discovered in a complex STO(10nm)/PTO(36nm)/STO(3nm)/PTO(28nm)/GSO system [111]. The GPA of the thin film shows a regular distribution of out-of-plane strain tensor. Selected areas were chosen for mapping the atomic arrangements, shown in Figure 2.20. Although the authors call these "flux closure quadrants", the flux is not closed in the sense that they only rotate 270° in the images. But again, finding these rotational domains in the PTO/STO system is already a breakthrough, which serves like a platform or playground in ferroelectric study. By learning the possible local topological structures, it can be envisaged that general design rules could be elaborated to create larger configurations for specific purposes in the future.

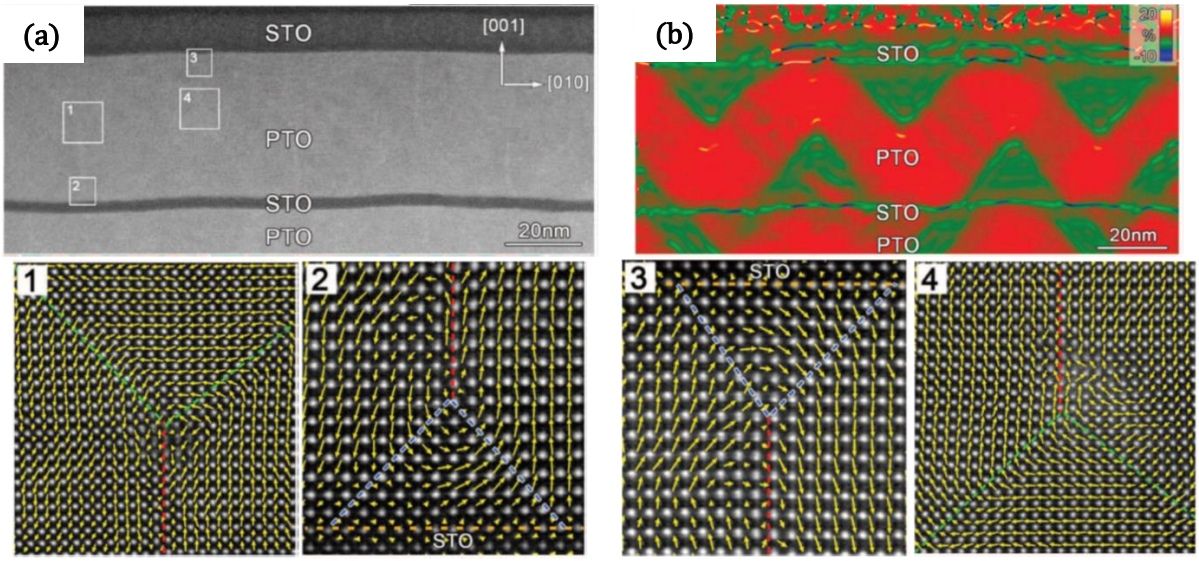

Figure 2.20 Flux closure domains in PTO/STO thin film. (a) HAADF-STEM image. Zoom-in micrographs of box area with number 1-4 are showing at the bottom. (b) GPA analysis. Image from [111].

In 2016, a full vortex array was found in a PTO/STO superlattice, as shown in Figure 2.21 [112]. The two adjacent vortices are clockwise and anti-clockwise, so that they can share the boundary with each other. These vortex arrays appear to be elongated in the third dimension, suggesting the 3D structure to be vortex tubes. A Phase field simulation was also presented to support the experimental result.

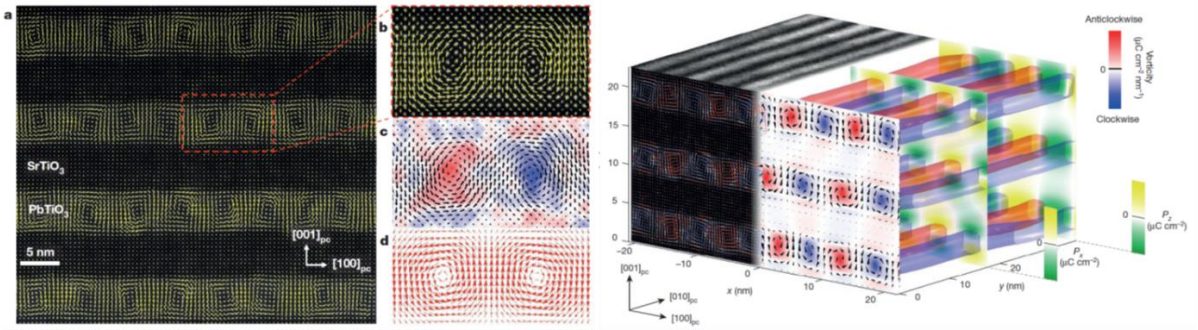

Figure 2.21 HAADF-STEM image on the top and side of PTO/STO superlattice film. Phase field simulation is also presented. Image from [112].

2.2.4 Skyrmion and meron bubble

A magnetic skyrmion describes a magnetic configuration of a chiral-lattice magnet with its spin directions forming a vortex-like topology. This has drawn interest for potential applications such as racetrack memory. The corresponding structure in ferroelectrics is, however, less obvious and hard to characterize. Recently, polar skymion-like bubbles were experimentally confirmed in a PTO/STO thin film system, utilizing the lattice mismatch strain in the heterostructure [113-114]. Figure 2.22 shows the main result. By some pre-knowledges from dark-field TEM, the polar skyrmion bubbles were first simulated in a thin film in Figure 2.22a (black box). At the centre, the polar direction is upward. There are two clear boundaries on two sides, where the vortices are formed. The polar direction rotates a total circle of 360° when going through this skyrmion bubble. Such a structure agrees with the experimental observation shown in Figure 2.22c (blue box), which is the polar order derived from the atomic positions in HAADF-STEM image. The three section views of the simulated skymions show that at the top and bottom position of such skyrmion, the polarization is hedgehog-like with a Neel type domain wall. In the middle position, the polarization is vortex-like with a Bloch type domain wall. The calculated ADF image and polar order match the TEM image as well. This class of topological structure is usually quantified by a "skyrmion number", N. Different definitions have been put forward based on situations, for example:

$$N = \frac{1}{4\pi}\iint u \cdot \left(\frac{\partial u}{\partial x} \times \frac{\partial u}{\partial y}\right) dxdy \tag{2.40}$$

u is normalized local dipole moment. For the model building in this paper, the skymion number N is $+1$ for all slices.

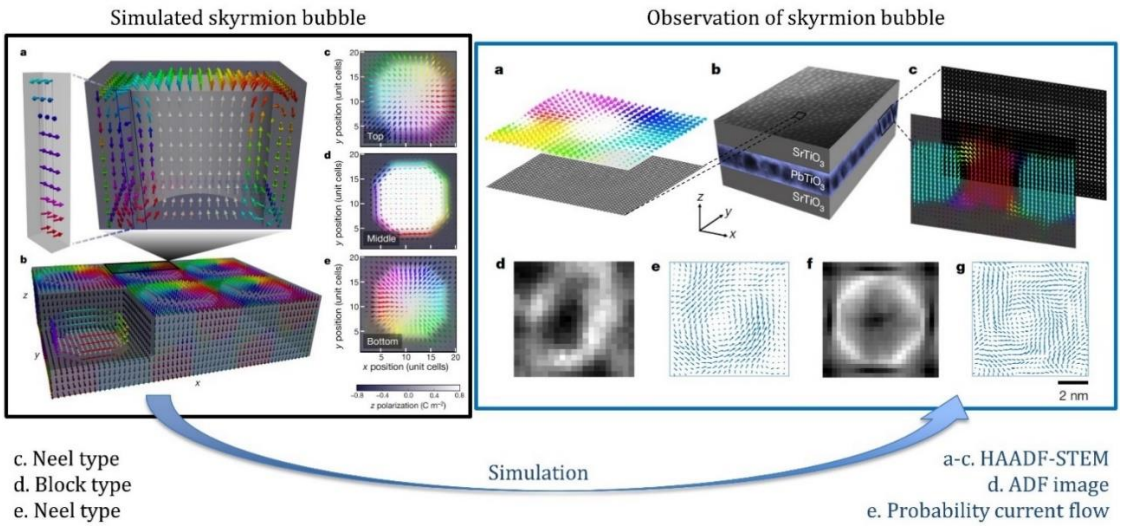

Figure 2.22 Simulated skyrmion bubbles and the experimental proof of possible skyrmion bubbles in PTO/STO system. Image revised from [113].

Notably, because STEM only measures the projection of atomic position, it doesn't visualize the polar skyrmions directly. Instead, by combination of TEM image and simulation model, it infers a polar skyrmion bubble structure.

A "Meron" is considered to be half a skyrmion. The polar direction rotates 180° when crossing a meron bubble, which is half the magnitude of skyrmion. Wang et al reported the first observation of regularly distributed merons in 5nm thick PTO/STO thin film [115]. Figure 2.23 shows two meron bubbles with both phase field simulations and HAADF-STEM images. The sizes of merons are roughly 5nm, and they appear only at the stripe walls. These merons are regularly distributed and the spacing between two domains along a stripe line is 8nm on average. Such meron arrays have also been found in other system including PTO/GSO and PTO/SSO. The density of merons is dependent on in-plane strain: the meron and anti-meron density first increases with strain and decreases after reaching the peak value at about 2.25%.

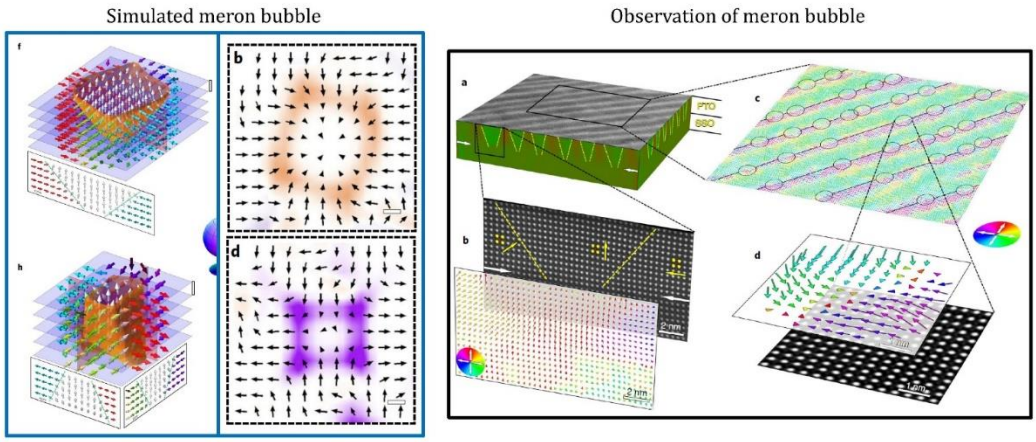

Figure 2.23 Simulated meron structures and experimental observation by HAADF-STEM. Image from [115].

In this section, different works are listed to show the development and understanding of vortices step by step. Despite the observation of these hierarchical structures, the easily

overlooking point is whether the structure inferred from the image is correct or not. Most of these results are based on HAADF-STEM, which only shows the projection views that is both 2D-projected and averaged out. All the usual caveats about TEM sample preparation and use of very thin specimens apply to the results. The PFM result has a significant resolution limit and is only a rather qualitative method. Therefore, it's better to view the above results as a taste of possibilities instead of the finished textbook.

2.3 Core-shell model

Core-shell models are widely used in nanoparticle research. Often composed of inner and outer shells of two different materials, the most general model is when the central core and outer shell differs in some order parameters. In BTO, there are at least two kinds of core-shell models that attract scientific interest. The first and the most studied core-shell includes a pure tetragonal BTO core and a chemically doped BTO shell. This is commonly used as a multilayer ceramic capacitor in industry [116,117]. The growing industrial interest for miniaturization of electronic devices has accelerated the study in this particular direction.

The second core-shell structure was proposed by Wada and Hoshino [118-120]. This core-shell model does not contain any dopant but pure BTO crystal. It consists of an inner tetragonal core, some band of transition material and an outer cubic shell, as shown in Figure 2.24a. For a typical 200nm diameter BTO crystal, the inner tetragonal core would span more than 50nm in radius and the outer cubic shell occupies the last 10nm in radius, according to the model. The experimental proof of this model comes from X-ray powder diffraction, shown in Figure 2.24b. For their fine crystal sample, specially synthesized, the adjacent 200 and 002 peaks are not sharp. There is a large amount of intensity between the two peaks that cannot be fitted by pure tetragonal structure using Rietveld refinement. These scattering data, however, agree well with the core-shell model proposed. We are particularly interested in this core-shell model and have performed a series of BCDI study on the commercial BTO nanocrystals. However, the XRD profile of our samples only shows two sharp peaks with a width corresponding to the particle size, which does not favour a core-shell model. We attribute this difference to the sample, where the samples from Wada's group are claimed to be fine crystal with almost no defect [120]. We are tackling this problem on two fronts: while we are making experimental advances by learning how to synthesize BTO nanoparticles, we did simulations to predict the characteristics of core-shell model in a BCDI experiment. Figure 2.24c shows the simulated BTO crystal and the corresponding Bragg diffraction pattern. The simulated crystal has displacement field accumulated on two sides, because the Q-vector is set to be 110. The coherent Bragg diffraction pattern shows three peaks in the vicinity of each other. These outer two peaks represent the inner core and the outer shell, while the middle peak comes from the assumed transition region.

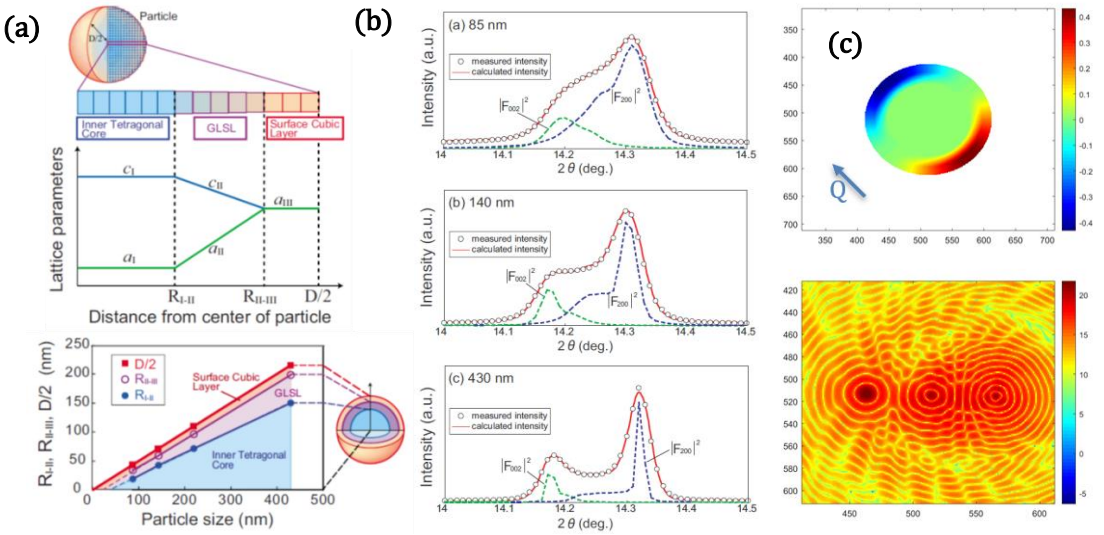

Figure 2.24 (a) The sketches of core-shell model. Image from [119]. (b) XRD profile of BTO fine crystal from Wada's group. Image from [120]. (c) Simulated image from a core-shell model and its diffraction pattern.

2.4 Polar nanoregions

2.4.1 Relaxor ferroelectrics

The relaxor ferroelectrics, simply called relaxors, are ferroelectric materials that show dielectric relaxation in the time domain. They show several distinct differences from normal ferroelectrics [121]:

(a) No well-defined Curie temperature
(b) Strong frequency dispersion of dielectric permittivity
(c) Frequency dependent temperature of maximum dielectric loss and dielectric permittivity

For (a), the specific phase transition temperature is one of the defining characteristics in comparing crystals and glasses. In one interpretation for relaxors, the poorly defined Curie temperature means that different regions would transform from paraelectric phase to ferroelectric at different temperatures, rather than developing full long-range order. (b) and (c) describes the same frequency dependence, but from different points of view. Figure 2.25 shows a typical dielectric permittivity curve of ferroelectrics and relaxors [122]. Ferroelectrics show a distinct anomaly as shown in Figure 2.25a. The relaxors can be divided into two categories according to their response to temperature, as shown in Figure 2.25b and c. This will be discussed in the next section. In both types, with the increasing frequency of applied field, the maximum dielectric permittivity decreases, while the temperature for the maximum dielectric permittivity increases.

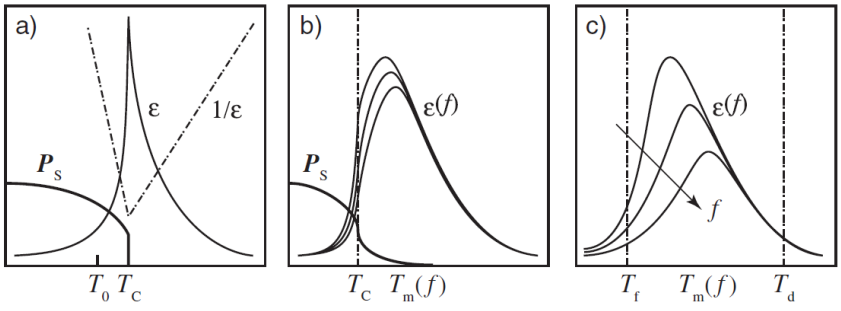

Figure 2.25 Dielectric permittivity as a function of temperature. (a) First order ferroelectric (b) Ferroelectric with a diffuse transition. (c) Canonical relaxor. Image from [122].

The compositional disorder and the resulting charge and strain inhomogeneities are usually considered as essential but not sufficient to induce relaxor behaviour [ref?]. All the known relaxor materials include some kind of composition disorder. The most studied PMN and PMN-PT relaxors involve chemically disordered B-site cations [123,124]. The solid solution type BSTO, for example, has a ferroelectric BTO phase and paraelectric STO phase. The proper mixing of BTO and STO would lead to inhomogeneous ferroelectric regions embedded in paraelectric regions [125]. Aliovalent cation doping in both ferroelectrics and paraelectrics could lead to relaxors, like the La-doped PTO and Bi-doped STO [126,127].

However, some disordered systems like PZT show no dielectric relaxation. BTO also shows disorder local structure and polar nanoregions or precursors in cubic phase, but it also has no dielectric relaxation. This is covered in Chapter 2.5.

2.4.2 Polar nanoregions in relaxors

Polar nanoregions (PNRs) are defined as finite-sized regions, either dynamic or static, with a nonzero spontaneous electrical polarization [128]. While the definition of PNRs is straightforward, the details depend on specific systems. It's better to understand the development of polar nanoregions through the transitions of relaxors.

The relaxors experience a series of transformation upon cooling:

(a) Paraelectric state ($T > T_B$)

When above the Burns temperature, T_B, relaxor materials are paraelectric. There is no evidence of any noticable static polar nanoregions in this state.

(b) Type-I relaxor state ($T_B > T > T^*$)

Somewhere between the Burns temperature T_B and an intermediate temperature T^*, the polar nanoregions start to nucleate. These polar nanoregions are both dynamic and have random polarized direction. This dynamic means the polar nanoregions could flip their direction due to thermal excitation.

The Burns temperature is first seen as the deviation from a linear relation between optical refractive index and temperature and can be measured by Raman spectroscopy [129,130].

(c) Type-II relaxor state ($T^* > T > T_f$)

Between the intermediate temperature T^* and the freezing temperature T_f, the PNRs start to form larger clusters. The flipping dynamic of PNRs becomes slowed down, so that the static component of polarization starts to appear. The PNRs are considered both partially dynamic and static in this state.

The combination of Type-I and Type-II relaxor state is called ergodic state, because they share some similar characteristics. The most important feature is that the PNRs have random distributions of polarization direction, so there is no preferred polarization macroscopically.

(d) Type-III relaxor state ($T_f > T$)

When the temperature decreases below the freezing temperature T_f, the relaxor goes into non-ergodic state. In this state, the local polarization becomes frozen. The local symmetry deviates from high symmetry phase, while macroscopically the crystal still has high symmetry. PNRs are considered to be fully static in this state.

(e) Ferroelectric state ($T_c > T$)

It should be noted that not all relaxors have this ferroelectric phase transition, in which case there is no T_c at all. Canonical relaxors have this phase transition. One important example is the well-studied $PbMg_{1/3}Nb_{2/3}O_3$ (PMN). But there do exist some relaxors which could transform to have long range ferroelectric ordering at the transition temperature T_c. For example, the PMN-xPT (0.05<x<0.35) would have such a ferroelectric phase transition [131]. However, the PNRs are still detectable in this ferroelectric state, therefore their coexistence with polar order is favoured. These two kinds of polar ordering, namely the PNRs and ferroelectric domains, exist at different length scale and contribute to the same long-range ferroelectric order [132].

The PNRs are probed and studied by a number of spectroscopic techniques such as diffuse X-ray and neutron scattering, EXAFS, acoustic emission and dielectric spectroscopy [133-137].

The direct observations are given by TEM and PFM. Figure 2.26a shows some dark field TEM results of PMN [138]. The image of PNRs and chemical ordering regions (CORs) are obtained by inverse Fourier transform of the TEM images. The size of PNRs is 15nm~25nm, and the size of CORs is 5nm. Figure 2.26b shows another example of PMN seen by high resolution TEM at the top-left panel [139]. The top-right panel presents the FFT of the TEM image, and the bottom-left panel shows the schematically the distribution of PNRs.

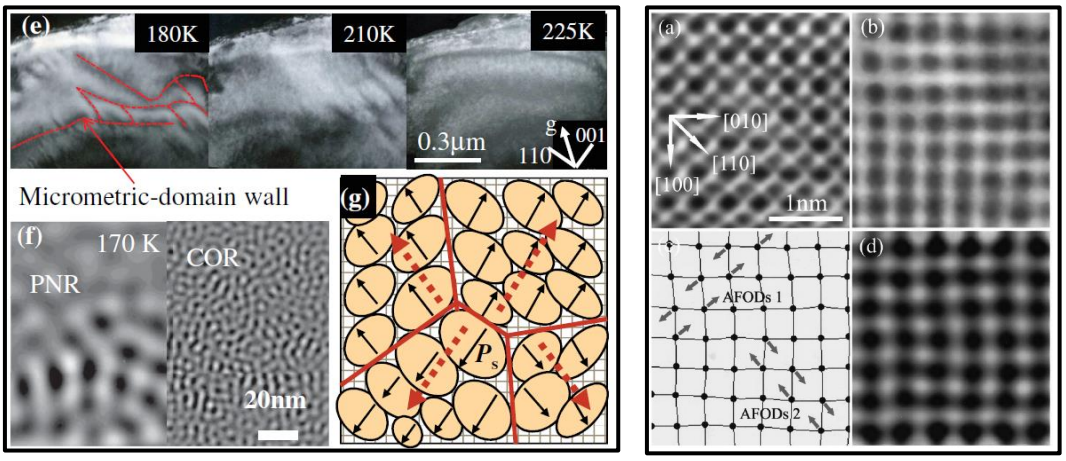

Figure 2.26 Left panel are the 111 reflection dark field TEM image of PMN and related PNR image and COR image. A sketch of the PNRs is also plotted. Image from [138]. Right panel shows the 001 reflection TEM image of PMN, it's FFT image, a schematic diagram of Pb displacement and computer simulated image from FFT image. Image from [139].

PFM, as illustrated in Chapter 2.21, is effective in measuring the static or dynamic polarization via local piezo response. An autocorrelation image could be further generated from the autocorrelation of PFM image:

$$C(r_1, r_2) = \sum_{x,y} D(x, y)D(x + r_1, y + r_2) \tag{2.41}$$

D(x,y) is the piezo response value at position (x,y). The shape of autocorrelation function provides the symmetry and regularity of the polarization [140].

To measure the short-range order, one way is to average over the autocorrelation functions in all in-plane directions should be taken and expressed as [141]:

$$\langle C(r)\rangle_{short} = \sigma^2 e^{-(\frac{r}{\langle\xi\rangle})^{2h}} \tag{2.42}$$

r is the distance from central peak. $\langle\xi\rangle$ is the average correlation radius. The exponent h is a measure of the roughness of the polarization surface.

If the long-range order is considered, its contribution can be expressed as:

$$\langle C(r)\rangle_{long} = (1-\sigma^2)e^{\left(-\frac{r}{r_c}\right)\cos\left(\frac{\pi r}{a}\right)} \tag{2.43}$$

a is the period of structure and r_c is the long-range correlation length.

Then the full autocorrelation function considering both short-range and long-range order can be summed up:

$$\langle C(r)\rangle = \langle C(r)\rangle_{short} + \langle C(r)\rangle_{long} = \sigma^2 e^{-(\frac{r}{\langle\xi\rangle})^{2h}} + (1-\sigma^2)e^{\left(-\frac{r}{r_c}\right)\cos(\frac{\pi r}{a})} \tag{2.44}$$

Figure 2.27 shows the PFM results and corresponding autocorrelation images of PMN, PMN-PT10 and PMN-PT20 [140,142]. PMN has small regions in the PFM image and they are static for 5-20min. Using the short-range autocorrelation function $\langle C(r)\rangle_{short}$, the average correlation length is estimated to be around 46nm. PMN-PT10 shows nanoregions in size of tens of nanometers in PFM image, which is larger than pure PMN. The full autocorrelation function is mapped out in Figure 2.27d, which shows oscillation along crystallographic 110 direction. This indicates the short-range order is along the 110 direction. The short-range correlation length is fitted to be 70nm and the long-range correlation length is 800nm in PMN-PT10. PMN-PT20 shows strong ferroelectric ordering in PFM image, while the long-range correlation length is about 2~2.5um.

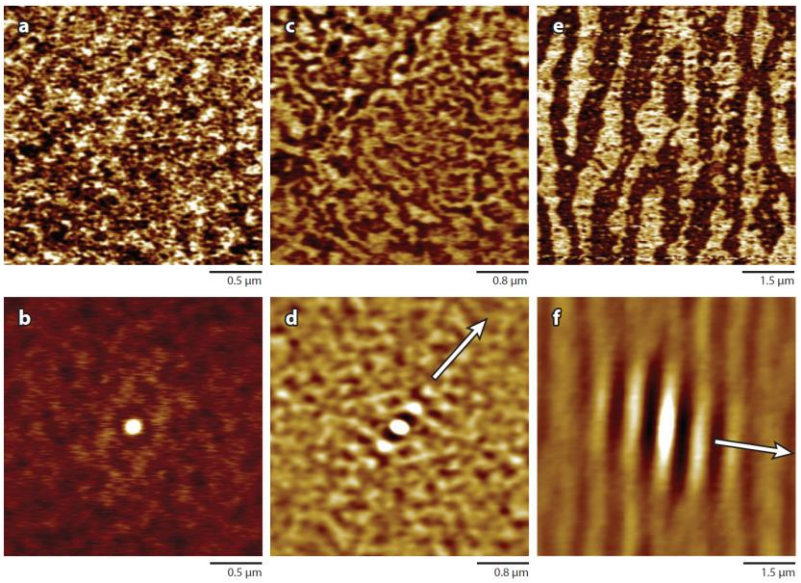

Figure 2.27 (a), (c) and (e) are PFM images of PMN, PMN-PT10, PMN-PT20. (b), (d) and (f) are corresponding autocorrelation images. Image from [140].

However, it should be noted that even in the same system, the size of PNRs could be quite distinct from different measuring techniques. Even the validity of the methods is not solid and raises concerns in their own fields. For example, it's strange to get both PNRs and CORs from purely a dark field TEM image. As the TEM expert Yimei Zhu once put it, many TEM based works could published in good journals like Nature or Science, but they cannot publish in electron microscopic journals for technical reasons. Therefore, the over interpretation of data might also appear in this Chapter, and it is fully based on the readers to judge whether this is true or only a possibility.

PNRs work well in describing the relaxor properties. For example, the dielectric relaxation can be explained by PNRs via the Vogel-Fulcher law:

$$f = f_0 e^{\frac{E_a}{k(T_m - T_f)}} \tag{2.45}$$

T_m is maximum dielectric permittivity temperature. E_a is an activation energy. f_0 is saturation frequency.

To understand the formation and mechanism of PNRs in relaxors, different models have been proposed. Some widely used models include a compositional fluctuation model, a superparaelectric model and a dipole glass model.

The compositional fluctuation model proposes the disordered hetero-valent cation at equivalent crystallographic position to be the compositionally disordered. The local compositional disorder would lead to regions with distinct local Curie temperature and different transition temperature. Such regions are called the polar nanoregions in this model.

The superparaelectric model is an extension of the compositional model and resembles its magnetic counterpart super-paramagnetism. The polar regions are thought be embedded in a paraelectric matrix and not interacting with each other. These polar nanoregions are dynamic and can flip due to thermal excitation, which resembles a spin glass.

2.5 Local structure

From low temperature to high temperature, BTO goes from low symmetry to high symmetry, following rhombohedral, orthorhombic, tetragonal and cubic lattice structures, in sequence. As described in Chapter 2.4, the soft mode theory supports a displacive type model. However, various local structure studies have revealed the existence of rhombohedral local distortions in all crystal phases of BTO, which indicates the order-disorder component.

Figure 2.28 shows the Pair Distribution Function (PDF) results for BTO while crossing the rhombohedral to orthorhombic and orthorhombic to tetragonal phase transitions [143]. The atomic displacement shows no noticeable difference in all these crystal phases. Because the PDF is only sensitive to local structure, different global structures could be formed by selectively choosing some of the eight site rhombohedral distortion directions. For example, the tetragonal could be formed by choosing four of the eight site directions, and the cubic phase is averaged out by all eight site directions.

PDF based refinement using reverse Monte Carlo (RMC) also supports the Ti displacement to be zone-centred rhombohedral like. Figure 2.28c shows the atomic structure after refinement and their calculated diffuse scattering in the planes [144]. The RMC calculation uses large supercells instead of the small boxes used in Rietveld

refinement [145]. It refines the atomic displacement to fit both G(r) and S(r). However, the work has been criticised because too many degrees of freedoms exist in the RMC method, so it gives an impression of the structure, rather than a unique answer. Bias are often introduced in the selection of RMC model parameters and this could lead to different detailed results from the random numbers used to perform RMC.

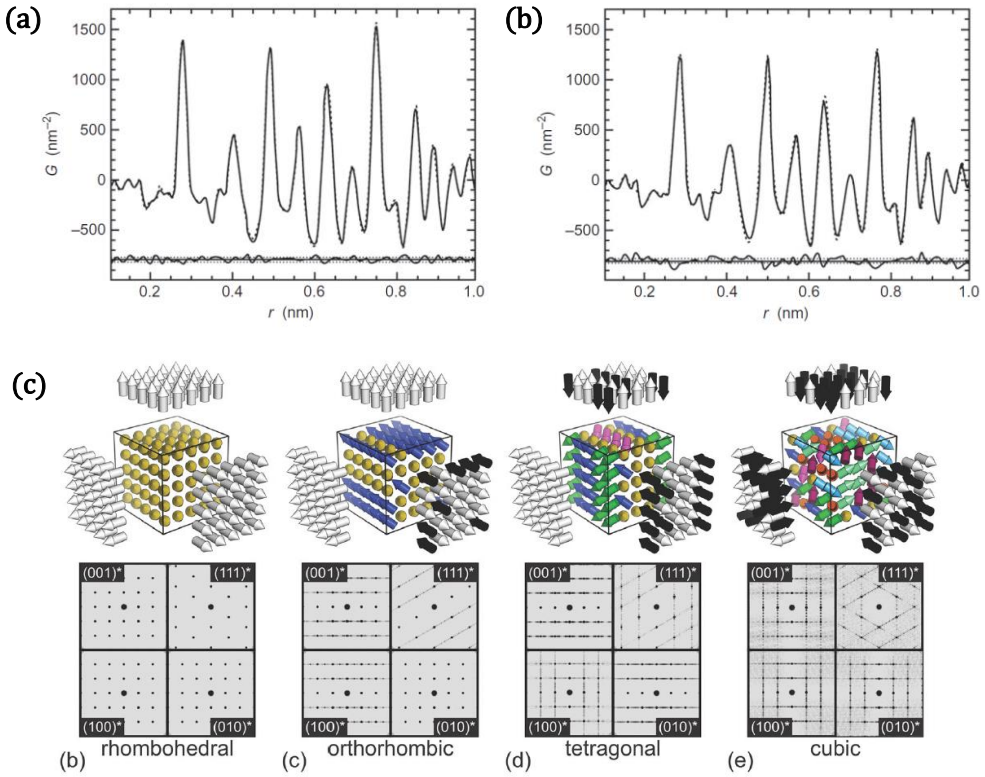

Figure 2.28 (a) PDF result of BTO passing through rhombohedral to orthorhombic phase transition. (b) PDF result of BTO going through orthorhombic to tetragonal phase transition. In both cases two PDF profiles are superimposed and their difference is shown below. The solid line is above phase transition, and the dash line is below. Image from [143]. (c) A portion of simulation results of each phase are shown, with corresponding calculated diffuse scattering in the planes indicated. Image from [144].

X-ray absorption fine structure (XAFS) also confirms a different local structure relative to the global structure. The combination the K-edge Extended XAFS (EXAFS) of Ba K-edge and X-ray absorption near edge structure (XANES) of Ti K-edge quantitatively support the eight-sight model. The local Ti displacement direction is calculated to be 11.7° away from the 111 direction towards the c axis in tetragonal phase. Such displacement of Ti from oxygen octahedral centre is 0.19Å at 35K and 0.16 Å at 750K [146].

Figure 2.29 shows first-principles calculated energy as a function of Ti distortion relative to Ba [147]. When the soft mode distortion is small ($\pm$0.1 in image), the rhombohedral phase has the lowest energy of all phases and the tetragonal phase is unstable.

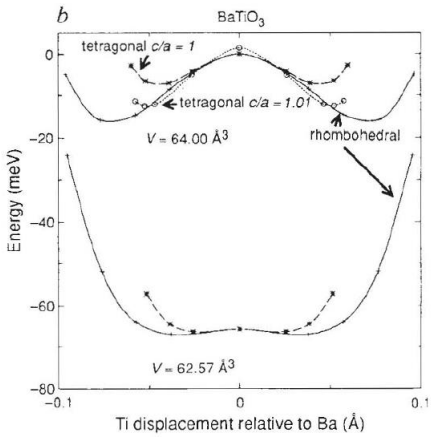

Figure 2.29 Calculated energy as a function of soft-mode distortion in BTO. Image from [147].

Reference

[1] M. E. Lines and A. M. Glass, Principles and Applications of Ferroelectrics and Related Materials (2010). https://doi.org/10.1093/acprof:oso/9780198507789.001.0001

[2] E. R. Caley, J. F. C. Richards, Theophrastus On Stones, The Ohio State U., Columbus (1956). http://hdl.handle.net/1811/32541

[3] Lang, S. B. (2005). Pyroelectricity: From ancient curiosity to modern imaging tool. Physics Today, 58(8), 31–36. https://doi.org/10.1063/1.2062916

[4] Curie, J. and Curie, P. (1881). "Contractions and expansions produced by voltages in hemihedral crystals with inclined faces," Comptes Rendus 93: 1137-1140.

[5] Valasek, J. (1921). Piezo-electric and allied phenomena in Rochelle salt. Physical Review, 17(4), 475–481. https://doi.org/10.1103/PhysRev.17.475

[6] G. Busch and P. Scherrer, Naturwissenschaften, 1935, 23, 737. https://doi.org/10.1080/00150198708224825

[7] Cai, W., & Katrusiak, A. (2013). Structure of the high-pressure phase IV of KH2PO4 (KDP). Dalton Transactions, 42(4), 863–866. https://doi.org/10.1039/c2dt32131a

[8] Horiuchi, S., Tokunaga, Y., Giovannetti, G., Picozzi, S., Itoh, H., Shimano, R., Kumai, R., & Tokura, Y. (2010). Above-room-temperature ferroelectricity in a single-component molecular crystal. Nature, 463(7282), 789–792. https://doi.org/10.1038/nature08731

[9] Katrusiak, A., & Szafranski, M. (1999). Ferroelectricity in NH···N hydrogen bonded crystals. Physical Review Letters, 82(3), 576–579. https://doi.org/10.1103/PhysRevLett.82.576

[10] Szafrański, M., Katrusiak, A., & McIntyre, G. J. (2010). Proton disorder in NH···N bonded [dabcoH]+I- relaxor: New insights into H-disordering in a one-dimensional H2O ice analogue. Crystal Growth and Design, 10(10), 4334–4338. https://doi.org/10.1021/cg100247g

[11] von Hippel, A., Breckenridge, R. G., Chesley, F. G., & Tisza, L. (1946). High dielectric constant ceramics. Industrial & Engineering Chemistry, 38(11), 1097–1109. https://doi.org/10.1021/ie50443a009

[12] Roberts, S. (1950). Dielectric Properties of Lead Zirconate and Barium-Lead Zirconate. Journal of the American Ceramic Society, 33(2), 63–66. https://doi.org/10.1111/j.1151-2916.1950.tb14168.x

[13] Shirane, G., & Suzuki. K., (1952), J. Phys. Soc. Jpn. 7, 333. https://doi.org/10.1143/JPSJ.7.333

[14] Garcia, V., Fusil, S., Bouzehouane, K., Enouz-Vedrenne, S., Mathur, N. D., Barthélémy, A., & Bibes, M. (2009). Giant tunnel electroresistance for non-destructive readout of ferroelectric states. Nature, 460(7251), 81–84. https://doi.org/10.1038/nature08128

[15] Noh, K. H., Yang, B., Lee, S. W., Lee, S. S., Kang, H. B., & Park, Y. J. (2003). Issues and reliability of high-density FeRAMs. Japanese Journal of Applied Physics, 42, 2096–2099. https://doi.org/10.1143/jjap.42.2096

[16] M. Nespolo, J. Appl. Crystallogr. 52, 451 (2019) https://doi.org/10.1107/S1600576719000463

[17] M. Nespolo, IUCr Newsletter 27, 2 (2019) https://www.iucr.org/news/newsletter/volume-27/number-2/the-lattice-sickness-pandemic

[18] IUCr Online Dictionary of Crystallography https://dictionary.iucr.org/Lattice_system

https://dictionary.iucr.org/Crystal_system

https://dictionary.iucr.org/Crystal_family

[19] IUCr Online Dictionary of Crystallography

https://dictionary.iucr.org/Goldschmidt_tolerance_factor

[20] F. S. Galasso, Structure, properties, and preparation of perovskite-type compounds, London, Pergamon Press; 1969. https://doi.org/10.1016/c2013-0-02117-2

[21] A. von Hippel, Rev. Mod. Phys. 22, 221 (1950) https://doi.org/10.1103/RevModPhys.22.221

[22] F. Jona, G. Shirane, Ferroelectric crystals, London, Pergamon Press; 1962.

https://doi.org/10.1002/zamm.19630431016

[23] Ishidate, T., & Abe, S. (1997). Phase Diagram of $BaTiO_3$, 78(2), 2397–2400. https://doi.org/10.1103/PhysRevLett.78.2397

[24] Enhancement of ferroelectricity in strained $BaTiO_3$ thin films. (2004). Science, 306(5698), 1005–1009. https://doi.org/10.1126/science.1103218

[25] Slater, J. C. (1950). The lorentz correction in barium titanate. Physical Review, 78(6), 748–761. https://doi.org/10.1103/PhysRev.78.748

[26] Cochran, W. (1960). Crystal stability and the theory of ferroelectricity. Advances in Physics, 9(36), 387–423. https://doi.org/10.1080/00018736000101229

[27] Ahn, C. H., Rabe, K. M., & Triscone, J. (2004). Ferroelectricity at the Nanoscale: Local Polarization in Oxide Thin Films and Heterostructures, Science, 303, 488–492. http://doi.org/10.1126/science.1092508

[28] Comes, R., Lambert, M., & Guinier, A. (1968). Solid State Communications, 6(010), 715–719. https://doi.org/10.1016/0038-1098(68)90571-1

[29] Chaves, A. S., Barreto, F. C. S., & Noqueira, R. A. (1976). Physical Review B, 13(1), 207–212. https://doi.org/10.1103/PhysRevB.13.207

[30] Hlinka, J., Ostapchuk, T., Nuzhnyy, D., Petzelt, J., Kuzel, P., Kadlec, C., Vanek, P., Ponomareva, I., & Bellaiche, L. (2008). Coexistence of the phonon and relaxation soft modes in the terahertz dielectric response of tetragonal $BaTiO_3$. Physical Review Letters, 101(16), 1–4. https://doi.org/10.1103/PhysRevLett.101.167402

[31] Tai, R. Z., Namikawa, K., Sawada, A., Kishimoto, M., Tanaka, M., Lu, P., Nagashima, K., Maruyama, H., Ando, M. (2004). Picosecond view of microscopic-scale polarization clusters in paraelectric $BaTiO_3$. Physical Review Letters, 93(8), 087601. https://doi.org/10.1103/PhysRevLett.93.087601

[32] Stern, E. A. (2004). Character of Order-Disorder and Displacive Components in Barium Titanate, Physical Review Letters, 93(3), 037601. https://doi.org/10.1103/PhysRevLett.93.037601

[33] Isohama, Y., Nakajima, N., Maruyama, H., Tezuka, Y., & Iwazumi, T. (2011). Tetragonal-cubic phase transition in $BaTiO_3$ probed by resonant X-ray emission spectroscopy. Journal of Electron Spectroscopy and Related Phenomena, 184(3–6), 207–209. https://doi.org/10.1016/j.elspec.2010.12.023

[34] Translated and reprinted from Landau L.D. “Collected Papers” (Nauka, Moscow, 1969), Vol. 1, pp. 234–252. Originally published in Zh. Eksp. Teor. Fiz. 7, pp. 19–32 (1937) https://pdfs.semanticscholar.org/60d6/3a992ed0944d72a0b54c8eb182cbed14d1fa.pdf

[35] Cao, W. (2008). Constructing Landau-Ginzburg-Devonshire type models for ferroelectric systems based on symmetry. Ferroelectrics, 375, 28–39. https://doi.org/10.1080/00150190802437845

[36] Devonshire, A. (1949). Theory of barium titanate. Philosophical Magazine, 40(309), 1040-1063. https://doi.org/10.1080/14786444908561372

[37] Glinchuk, M. D., Zaulychny, B. Y., & Stephanovich, V. A. (2005). Depolarization field in thin ferroelectric films with account of semiconductor electrodes. Ferroelectrics, 316, 1–6. https://doi.org/10.1080/00150190590963057

[38] Levanyuk, A. P., Strukov, B. A., & Cano, A. (2016). Background dielectric permittivity: Material constant or fitting parameter? Ferroelectrics, 503(1), 94–103. https://doi.org/10.1080/00150193.2016.1218245

[39] Glinchuk, M. D., Eliseev, E. A., & Morozovska, A. N. (2007). Influence of built-in internal electric field on ferroelectric film properties and phase diagram. Ferroelectrics, 354(1), 86–98. https://doi.org/10.1080/00150190701454628

[40] Kim, I. H., Kim, I. H., Jang, K. O., Sin, K. R., & Kim, C. J. (2018). A new higher-order Landau–Ginzburg–Devonshire theory for $KNbO_3$ crystal. Phase Transitions, 91(12), 1189–1205. https://doi.org/10.1080/01411594.2018.1536269

[41] Yamamoto, T. (1998). Crystallographic, Dielectric and Piezoelectric Properties of $PbZrO_3$-$PbTiO_3$ System by Phenomenological Thermodynamics. Jpn. J. Appl. Phys., 37, 6041-6047. https://iopscience.iop.org/article/10.1143/JJAP.37.6041/meta

[42] Vijatović, M. M., Bobić, J. D., & Stojanović, B. D. (2008). History and challenges of barium titanate: Part II. Science of Sintering, 40(3), 235–244. https://doi.org/10.2298/SOS0803235V

[43] Stojanovic, B. D., Jovalekic, C., Vukotic, V., Simoes, A. Z., & Varela, J. A. (2005). Ferroelectric properties of mechanically synthesized nanosized barium titanate. Ferroelectrics, 319, 65–73. https://doi.org/10.1080/00150190590965424

[44] W. David Kingery, H. K. Bowen, Donald R. Uhlmann (1976). Introduction to Ceramics. John Wiley & Sons, Inc. https://doi.org/10.1149/1.2133296

[45] Gao, J., Xue, D., Liu, W., Zhou, C., & Ren, X. (2017). Recent progress on $BaTiO_3$-based piezoelectric ceramics for actuator applications. Actuators, 6(3). https://doi.org/10.3390/act6030024

[46] Haertling, G. H. (2007). Ferroelectric Ceramics: History and Technology. Ferroelectricity: The Fundamentals Collection, 818, 157–178. https://doi.org/10.1002/9783527618002.ch6

[47] Park, S. E., & Shrout, T. R. (1997). Ultrahigh strain and piezoelectric behavior in relaxor based ferroelectric single crystals. Journal of Applied Physics, 82(4), 1804–1811. https://doi.org/10.1063/1.365983

[48] Zhang, Q. M., & Zhao, J. (1999). Electromechanical properties of lead zirconate titanate piezoceramics under the influence of mechanical stresses. IEEE Transactions on Ultrasonics, Ferroelectrics, and Frequency Control, 46(6), 1518–1526. https://doi.org/10.1109/58.808876

[49] You, Y. M., Liao, W. Q., Zhao, D., Ye, H. Y., Zhang, Y., Zhou, Q., Niu, X., Wang, J., Li, P., Fu, D., Wang, Z., Gao, S., Yang, K., Liu, J., Li, J., Yan, Y., & Xiong, R. G. (2017). An organic-inorganic perovskite ferroelectric with large piezoelectric response. Science, 357(6348), 306–309. https://doi.org/10.1126/science.aai8535

[50] Wada, S., Kakemoto, H., & Tsurumi, T. (2004). Enhanced Piezoelectric Properties of Piezoelectric Single Crystals by Domain Engineering. Materials Transactions, 45(2), 178–187. https://doi.org/10.2320/matertrans.45.178

[51] Bell, A. J. (2001). Phenomenologically derived electric field-temperature phase diagrams and piezoelectric coefficients for single crystal barium titanate under fields along different axes. Journal of Applied Physics, 89(7), 3907–3914. https://doi.org/10.1063/1.1352682

[52] Wada, S., Yako, K., Kakemoto, H., Tsurumi, T., & Kiguchi, T. (2005). Enhanced piezoelectric properties of barium titanate single crystals with different engineered-domain sizes. Journal of Applied Physics, 98, 014109. https://doi.org/10.1063/1.1957130

[53] Wada, S., Takeda, K., Muraishi, T., Kakemoto, H., Tsurumi, T., & Kimura, T. (2007). Preparation of [110] grain oriented barium titanate ceramics by templated grain growth method and their piezoelectric properties. Japanese Journal of Applied Physics, 46(10), 7039–7043. https://doi.org/10.1143/JJAP.46.7039

[54] Ma, N., Zhang, B. P., Yang, W. G., & Guo, D. (2012). Phase structure and nano-domain in high performance of $BaTiO_3$ piezoelectric ceramics. Journal of the European Ceramic Society, 32(5), 1059–1066. https://doi.org/10.1016/j.jeurceramsoc.2011.11.014

[55] Shao, S., Zhang, J., Zhang, Z., Zheng, P., Zhao, M., Li, J., & Wang, C. (2009). Erratum: High piezoelectric properties and domain configuration in $BaTiO_3$ ceramics obtained through solid-state reaction route. Journal of Physics D: Applied Physics, 42(18), 189801. https://doi.org/10.1088/0022-3727/42/18/189801

[56] Karaki, T., Yan, K., & Adachi, M. (2008). Subgrain microstructure in high-performance $BaTiO_3$ piezoelectric ceramics. Applied Physics Express, 1(11), 111402. https://doi.org/10.1143/APEX.1.111402

[57] Huan, Y., Wang, X., Fang, J., & Li, L. (2014). Grain size effect on piezoelectric and ferroelectric properties of $BaTiO_3$ ceramics. Journal of the European Ceramic Society, 34(5), 1445–1448. https://doi.org/10.1016/j.jeurceramsoc.2013.11.030

[58] Zheng, P., Zhang, J. L., Tan, Y. Q., & Wang, C. L. (2012). Grain-size effects on dielectric and piezoelectric properties of poled $BaTiO_3$ ceramics. Acta Materialia, 60(13–14), 5022–5030. https://doi.org/10.1016/j.actamat.2012.06.015

[59] R. E. Newnham. “Properties of materials.” Oxford University Press Inc. (2005)

[60] H. Kniepkamp and W. Heywang, Z. Angew. Phys., 6, 385 (1954).

[61] Uchino, K., Sadanaga, E., & Hirose, T. (1989). Dependence of the Crystal Structure on Particle Size in Barium Titanate. Journal of the American Ceramic Society, 72(8), 1555–1558. https://doi.org/10.1111/j.1151-2916.1989.tb07706.x

[62] Hoshina, T., Kakemoto, H., Tsurumi, T., Wada, S., & Yashima, M. (2006). Size and temperature induced phase transition behaviors of barium titanate nanoparticles. Journal of Applied Physics, 99(5), 1–9. https://doi.org/10.1063/1.2179971

[63] Shih, W. Y., Shih, W. H., & Aksay, I. A. (1994). Size dependence of the ferroelectric transition of small BaTiO3 particles: Effect of depolarization. Physical Review B, 50(21), 15575. https://doi.org/10.1103/PhysRevB.50.15575

[64] Buessem, W. R., Cross, L. E., & Goswami, A. K. (1966). Effect of Two-Dimensional Pressure on the Permittivity of Fine- and Coarse-Grained Barium Titanate. Journal of the American Ceramic Society, 49(1), 36–39. https://doi.org/10.1111/j.1151-2916.1966.tb13145.x

[65] Arlt, G., Hennings, D., & De With, G. (1985). Dielectric properties of fine-grained barium titanate ceramics. Journal of Applied Physics, 58(4), 1619–1625. https://doi.org/10.1063/1.336051

[66] Zhao, Z., Buscaglia, V., Viviani, M., Buscaglia, M. T., Mitoseriu, L., Testino, A., Nygren, M., Johnsson, M., Nanni, P. (2004). Grain-size effects on the ferroelectric behavior of dense nanocrystalline $BaTiO_3$ ceramics. Physical Review B, 70(2), 024107. https://doi.org/10.1103/PhysRevB.70.024107

[67] Frey, M., & Payne, D. (1996). Grain-size effect on structure and phase transformations for barium titanate. Physical Review B, 54(5), 3158. https://doi.org/10.1103/PhysRevB.54.3158

[68] Arlt, G., (1990). The influence of microstructure on the properties of ferroelectric ceramics. Ferroelectrics 104, 217. https://doi.org/10.1080/00150199008223825

[69] Reis, M. (2013). Landau Theory. Fundamentals of Magnetism, 52(9), 177–191. https://doi.org/10.1016/b978-0-12-405545-2.00011-4

[70] Junquera, J., & Ghosez, P. (2003). Critical thickness for ferroelectricity in perovskite ultrathin films. Nature, 422(6931), 506–509. https://doi.org/10.1038/nature01501

[71] Batra, I. P., Wurfel, P., & Silverman, B. D. (1973). New type of first-order phase transition in ferroelectric thin films. Physical Review Letters, 30(9), 384. https://doi.org/10.1103/PhysRevLett.30.384

[72] Batra, I. P., Wurfel, P., & Silverman, B. D. (1973). Phase transition, stability, and depolarization field in ferroelectric thin films. Physical Review B, 8(7), 3257. https://doi.org/10.1103/PhysRevB.8.3257

[73] WASER, R. (1988). Solubility of Hydrogen Defects in Doped and Undoped $BaTiO_3$. Journal of the American Ceramic Society, 71(1), 58–63. https://doi.org/10.1111/j.1151-2916.1988.tb05760.x

[74] Baikov, Y. M., & Shalkova, E. K. (1992). Hydrogen in perovskites. Journal of Solid State Chemistry, 97(1), 224–227. https://doi.org/10.1016/0022-4596(92)90027-S

[75] Kapphan, S. and Weber, G. (1981). IR-absorption study of H and D-impurities in $BaTiO_3$ crystals. Ferroelectrics 37, 673. https://doi.org/10.1080/00150198108223518

[76] Jovanović, A., Wöhlecke, M., Kapphan, S., Maillard, A., & Godefroy, G. (1989). Infrared spectroscopy of hydrogen centers in undoped and iron-doped $BaTiO_3$ crystals. Journal of Physics and Chemistry of Solids, 50(6), 623–627. https://doi.org/10.1016/0022-3697(89)90457-5

[77] Pennycook, S. J., & Jesson, D. E. (1990). High-resolution incoherent imaging of crystals. Physical Review Letters, 64(8), 938–941. https://doi.org/10.1103/PhysRevLett.64.938

[78] Lee, D., Lu, H., Gu, Y., Choi, S. Y., Li, S. D., Ryu, S., Paudel, T. R., Song, K., Mikheev, E., Lee, S., Stemmer, S., Tenne, D. A., Oh, S. H., Tsymbal, E. Y., Wu, X., Chen, L. Q., Gruverman A., & Eom, C. B. (2015). Emergence of room-temperature ferroelectricity at reduced dimensions. Science, 349(6254), 1314–1317. https://doi.org/10.1126/science.aaa6442

[79] Kim, S. D., Hwang, G. T., Song, K., Jeong, C. K., Park, K. Il, Jang, J., Kim, K. -H., Ryu, J., & Choi, S. Y. (2018). Inverse size-dependence of piezoelectricity in single $BaTiO_3$ nanoparticles. Nano Energy, 58, 78–84. https://doi.org/10.1016/j.nanoen.2018.12.096

[80] Tang, Y. L., Zhu, Y. L., Ma, X. L., Borisevich, A. Y., Morozovska, A. N., Eliseev, E. A., Wang, Y. J., Xu, Y. B., Zhang, Z. D., & Pennycook, S. J. (2015). Observation of a periodic

array of flux-closure quadrants in strained ferroelectric $PbTiO_3$ films. Science, 348(6234), 547–551. https://doi.org/10.1126/science.1259869

[81] Egami, T., & Billinge S. J. L. (2003). Underneath the Bragg peaks: structural analysis of complex materials. Elsevier ltd.

[82] Johnson, C. L., Hÿtch, M. J., & Buseck, P. R. (2004). Nanoscale waviness of low -angle grain boundaries. Proceedings National Academy of Sciences, 101(52), 17936–17939. https://doi.org/10.1073/pnas.0408348102

[83] Hÿtch, M. J., Putaux, J. L., & Pénisson, J. M. (2003). Measurement of the displacement field of dislocations to 0.03Å by electron microscopy. Nature, 423(6937), 270–273. https://doi.org/10.1038/nature01638

[84] Hÿtch, M. J., Snoeck, E., & Kilaas, R. (1998). Quantitative measurement of displacement and strain fields from HREM micrographs. Ultramicroscopy, 74(3), 131–146. https://doi.org/10.1016/S0304-3991(98)00035-7

[85] Gruverman, A., & Kalinin, S. V. (2006). Piezoresponse force microscopy and recent advances in nanoscale studies of ferroelectrics. Journal of Materials Science, 41(1), 107–116. https://doi.org/10.1007/s10853-005-5946-0

[86] Kalinin, S. V., Rar, A., & Jesse, S. (2006). A decade of piezoresponse force microscopy: Progress, challenges, and opportunities. IEEE Transactions on Ultrasonics, Ferroelectrics, and Frequency Control, 53(12), 2226–2251. https://doi.org/10.1109/TUFFC.2006.169

[87] Gruverman, A., Auciello, O., Hatano, J., & Kalinin, S. V. (1996). Scanning force microscopy as a tool for nanoscale study of ferroelectric domains. Ferroelectrics, 184, 11-20. https://doi.org/10.1080/00150199608230240

[88] Soergel, E. (2011). Piezoresponse force microscopy (PFM). Journal of Physics D: Applied Physics, 44(46). https://doi.org/10.1088/0022-3727/44/46/464003

[89] Somnath, S., Belianinov, A., Kalinin, S. V., & Jesse, S. (2015). Full information acquisition in piezoresponse force microscopy. Applied Physics Letters, 107(26). https://doi.org/10.1063/1.4938482

[90] Rodriguez, B. J., Callahan, C., Kalinin, S. V., & Proksch, R. (2007). Dual-frequency resonance-tracking atomic force microscopy. Nanotechnology, 18(47). https://doi.org/10.1088/0957-4484/18/47/475504

[91] Catalan, G., Seidel, J., Ramesh, R., & Scott, J. F. (2012). Domain wall nanoelectronics. Reviews of Modern Physics, 84(1), 119–156. https://doi.org/10.1103/RevModPhys.84.119

[92] Kittel, C. (1946). Theory of the structure of ferromagnetic domains in films and small particles. Physical Review, 70(11–12), 965–971. https://doi.org/10.1103/PhysRev.70.965

[93] Kittel, C. (1949). Physical Theory of Ferromagnetic Domains. Reviews of Modern Physics, 21, 541. https://doi.org/10.1103/RevModPhys.21.541

[94] Mitsui, T., & Furuichi, J. (1953). Domain structure of rochelle salt and KH2PO4. Physical Review, 90(2), 193–202. https://doi.org/10.1103/PhysRev.90.193

[95] Schilling, A., Adams, T. B., Bowman, R. M., Gregg, J. M., Catalan, G., & Scott, J. F. (2006). Scaling of domain periodicity with thickness measured in $BaTiO_3$ single crystal lamellae and comparison with other ferroics. Physical Review B, 74(2), 024115. https://doi.org/10.1103/PhysRevB.74.024115

[96] Randall, C. A., Kim, N., Kucera, J.-P., Cao, W., & Shrout, T. R. (2005). Intrinsic and Extrinsic Size Effects in Fine-Grained Morphotropic-Phase-Boundary Lead Zirconate Titanate Ceramics. Journal of the American Ceramic Society, 81(3), 677–688. https://doi.org/10.1111/j.1151-2916.1998.tb02389.x

[97] Schilling, A., Bowman, R. M., Gregg, J. M., Catalan, G., & Scott, J. F. (2006). Ferroelectric domain periodicities in nanocolumns of single crystal barium titanate. Applied Physics Letters, 89(21), 1–4. https://doi.org/10.1063/1.2393145

[98] Catalan, G., Lubk, A., Vlooswijk, A. H. G., Snoeck, E., Magen, C., Janssens, A., Rispens, G., Rijnders, G., Blank, D. H. A., & Noheda, B. (2011). Flexoelectric rotation of polarization in ferroelectric thin films. Nature Materials, 10(12), 963–967. https://doi.org/10.1038/nmat3141

[99] Seidel, J., Vasudevan, R. K., & Valanoor, N. (2016). Topological Structures in Multiferroics – Domain Walls, Skyrmions and Vortices. Advanced Electronic Materials, 2(1), 1–14. https://doi.org/10.1002/aelm.201500292

[100] Zubko, P., Gariglio, S., Gabay, M., Ghosez, P., & Triscone, J. M. (2011). Interface physics in complex oxide heterostructures. Annual Review of Condensed Matter Physics, 2(1), 141–165. https://doi.org/10.1146/annurev-conmatphys-062910-140445

[101] Hwang, H. Y., Iwasa, Y., Kawasaki, M., Keimer, B., Nagaosa, N., & Tokura, Y. (2012). Emergent phenomena at oxide interfaces. Nature Materials, 11(2), 103–113. https://doi.org/10.1038/nmat3223

[102] Kornev, I., Fu, H., & Bellaiche, L. (2004). Ultrathin Films of Ferroelectric Solid Solutions under a Residual Depolarizing Field, Physical Review Letter, 93, 196104. https://doi.org/10.1103/PhysRevLett.93.196104

[103] Ponomareva, I., Naumov, I. I., Kornev, I., Fu, H., & Bellaiche, L. (2005). Atomistic treatment of depolarizing energy and field in ferroelectric nanostructures. Physical Review B, 72(14), 1–4. https://doi.org/10.1103/PhysRevB.72.140102

[104] Naumov, I. I., Bellaiche, L., & Fu, H. (n.d.). Unusual phase transitions in ferroelectric nanodisks and nanorods, Nature, 432, 737–740. https://doi.org/10.1038/nature03107

[105] Schilling, A., Byrne, D., Catalan, G., Webber, K. G., Genenko, Y. A., Wu, G. S., Scott, J. F., & Gregg, J. M. (2009). Domains in Ferroelectric Nanodots, Nano Lett., 9, 3359-3364. https://doi.org/10.1021/nl901661a

[106] Rodriguez, B. J., Gao, X. S., Liu, L. F., Lee, W., Naumov, I. I., Bratkovsky, A. M., Hesse, D., & Alexe, M. (2009). Vortex Polarization States in Nanoscale Ferroelectric Arrays, Nano Lett., 9, 1127-1131. https://doi.org/10.1021/nl8036646

[107] Mcgilly, L. J., Schilling, A., & Gregg, J. M. (2010). Domain bundle boundaries in single crystal $BaTiO_3$ lamellae: searching for naturally forming dipole flux-closure/quadrupole chains, Nano Lett., 10, 4200–4205. https://doi.org/10.1021/nl102566y

[108] Mcquaid, R. G. P., Mcgilly, L. J., Sharma, P., Gruverman, A., & Gregg, J. M. (2011). Mesoscale flux-closure domain formation in single-crystal $BaTiO_3$. Nature Communications, 2, 404. https://doi.org/10.1038/ncomms1413

[109] Nelson, C. T., Winchester, B., Zhang, Y., Kim, S., Melville, A., Adamo, C., … Pan, X. (2011). Spontaneous Vortex Nanodomain Arrays at Ferroelectric, Nano Lett., 11, 828–834. https://doi.org/10.1021/nl1041808

[110] Jia, C., Urban, K. W., Alexe, M., Hesse, D., & Vrejoiu, I. (2011). Direct Observation of Continuous Electric Dipole Rotation in Flux-Closure Domains in Ferroelectric $Pb(Zr,Ti)O_3$, 311, 1420–1424. http://doi.org/10.1126/science.1200605

[111] Tang, Y. L., Zhu, Y. L., Ma, X. L., Borisevich, A. Y., Morozovska, A. N., Eliseev, E. A., Wang, W. Y., Xu, Y. B., Zhang, Z. D., & Pennycook, S. J. (2015). Observation of a periodic array of flux-closure quadrants in strained ferroelectric $PbTiO_3$ films. Science, 348(6234), 547–551. https://doi.org/10.1126/science.1259869

[112] Yadav, A. K., Nelson, C. T., Hsu, S. L., Hong, Z., Clarkson, J. D., Schleputz, C. M., Damodaran, A. R., Shafer, P., Arenholz, E., Dedon, L. R., Chen, D., Vishwanath, A., Minor, A. M., Chen, L. Q., Scott, J. F., Martin, L. W., & Ramesh, R. (2016). Observation of polar vortices in oxide superlattices. https://doi.org/10.1038/nature16463

[113] Das, S., Tang, Y. L., Hong, Z., Gonçalves, M. A. P., McCarter, M. R., Klewe, C., Nguyen, K. X., Gomez-Ortiz, F., Shafer, P., Arenholz, E., Stoica, V. A., Hsu, S. -L., Wang, B., Ophus, C., Liu, J. F., Nelson, C. T., Saremi, S., Prasad, B., Mei, A. B., Schlom, D. G., Iniguez, J., Garcia-Fernandez, P., Muller, D. A., Chen, L. Q., Junquera, J., Martin, L. W., & Ramesh, R. (2019). Observation of room-temperature polar skyrmions. Nature, 568(7752), 368–372. https://doi.org/10.1038/s41586-019-1092-8

[114] Seki, S., Yu, X. Z., Ishiwata, S., & Tokura, Y. (2012). Observation of skyrmions in a multiferroic material. Science, 336, 198-201. https://doi.org/10.1126/science.1214143

[115] Wang, Y. J., Feng, Y. P., Zhu, Y. L., Tang, Y. L., Yang, L. X., Zou, M. J., Geng, W. R., Han, M. J., Guo, X. W., Wu. B., & Ma, X. L. (2020). Polar meron lattice in strained oxide ferroelectrics. Nature Materials, 19, 881-886. https://doi.org/10.1038/s41563-020-0694-8

[116] Kishi, H., Okino, Y., Honda, M., Iguchi, Y., Imaeda, M., Takahashi, Y., Ohsato, H., & Okuda, T. (1997). The effect of MgO and rare-earth oxide on formation behavior of core-shell structure in $BaTiO_3$. Japanese Journal of Applied Physics, 36, 5954–5957. https://doi.org/10.1143/jjap.36.5954

[117] Bi, K., Bi, M., Hao, Y., Luo, W., Cai, Z., Wang, X., & Huang, Y. (2018). Ultrafine core-shell $BaTiO_3$@SiO_2 structures for nanocomposite capacitors with high energy density. Nano Energy, 51, 513–523. https://doi.org/10.1016/j.nanoen.2018.07.006

[118] Wada, S., Yasuno, H., Hoshina, T., Nam, S. M., Kakemoto, H., & Tsurumi, T. (2003). Preparation of nm-sized barium titanate fine particles and their powder dielectric properties. Japanese Journal of Applied Physics, 42, 6188–6195. https://doi.org/10.1143/jjap.42.6188

[119] Hoshina, T., Wada, S., Kuroiwa, Y., & Tsurumi, T. (2008). Composite structure and size effect of barium titanate nanoparticles. Applied Physics Letters, 93(19), 2006–2009. https://doi.org/10.1063/1.3027067

[120] Hoshina, T. (2013). Size effect of barium titanate: Fine particles and ceramics. Journal of the Ceramic Society of Japan, 121(1410), 156–161. https://doi.org/10.2109/jcersj2.121.156

[121] Li, F., Zhang, S., Damjanovic, D., Chen, L. Q., & Shrout, T. R. (2018). Local Structural Heterogeneity and Electromechanical Responses of Ferroelectrics: Learning from Relaxor Ferroelectrics. Advanced Functional Materials, 28(37), 1–21. https://doi.org/10.1002/adfm.201801504

[122] Hirota, K., Wakimoto, S., & Cox, D. E. (2006). Neutron and X-ray scattering studies of relaxors. Journal of the Physical Society of Japan, 75(11), 1–13. https://doi.org/10.1143/JPSJ.75.111006

[123] Takenaka, H., Grinberg, I., & Rappe, A. M. (2013). Anisotropic local correlations and dynamics in a relaxor ferroelectric. Physical Review Letters, 110(14), 147602. https://doi.org/10.1103/PhysRevLett.110.147602

[124] Jeong, I. K., Darling, T. W., Lee, J. K., Proffen, T., Heffner, R. H., Park, J. S., Hong, K. S., Dmowski, W., & Egami, T. (2005). Direct observation of the formation of polar nanoregions in $Pb(Mg_{1/3}Nb_{2/3})O_3$ using neutron pair distribution function analysis. Physical Review Letters, 94(14), 147602. https://doi.org/10.1103/PhysRevLett.94.147602

[125] Tyunina, M., & Levoska, J. (2004). Coexistence of ferroelectric and relaxor properties in epitaxial films of $Ba_{1-x}Sr_xTiO_3$. Physical Review B, 70(13), 132105. https://doi.org/10.1103/PhysRevB.70.132105

[126] Haertling, G. H. (2007). Ferroelectric Ceramics: History and Technology. Ferroelectricity: The Fundamentals Collection, 818, 157–178. https://doi.org/10.1002/9783527618002.ch6

[127] Levin, I., Keeble, D. S., Cibin, G., Playford, H. Y., Eremenko, M., Krayzman, V., Laws, W. J., & Reaney, I. M. (2019). Nanoscale Polar Heterogeneities and Branching Bi-Displacement Directions in $K_{0.5}Bi_{0.5}TiO_3$. Chemistry of Materials, 31(7), 2450–2458. https://doi.org/10.1021/acs.chemmater.8b05187

[128] Eremenko, M., Krayzman, V., Bosak, A., Playford, H. Y., Chapman, K. W., Woicik, J. C., Ravel, B., & Levin, I. (2019). Local atomic order and hierarchical polar nanoregions in a classical relaxor ferroelectric. Nature Communications, 10(1), 2728. https://doi.org/10.1038/s41467-019-10665-4

[129] Burns, G., & Dacol, F. H. (1983). Crystalline ferroelectrics with glassy polarization behavior. Physical Review B, 28(5), 2527–2530. https://doi.org/10.1103/PhysRevB.28.2527

[130] Mihailova, B., Bismayer, U., Güttler, B., Gospodinov, M., Boris, A., Berndhard, C., & Aroyo, M. (2005). Nanoscale phase transformations in relaxor-ferroelectric lead scandium tantalate and lead scandium niobate. Zeitschrift Fur Kristallographie, 220(8), 740–747. https://doi.org/10.1524/zkri.220.8.740.67075

[131] Noblanc, O., Gaucher, P., & Calvarin, G. (1996). Structural and dielectric studies of $Pb(Mg_{1/3}Nb_{2/3})O_3$-$PbTiO_3$ ferroelectric solid solutions around the morphotropic boundary. Journal of Applied Physics, 79(8), 4291–4297. https://doi.org/10.1063/1.361865

[132] Xu, G. (2010). Competing orders in PZN-xPT and PMN-xPT relaxor ferroelectrics. Journal of the Physical Society of Japan, 79(1), 33–36. https://doi.org/10.1143/JPSJ.79.011011

[133] Xu, G., Zhong, Z., Bing, Y., Ye, Z. G., & Shirane, G. (2006). Electric-field-induced redistribution of polar nano-regions in a relaxor ferroelectric. Nature Materials, 5(2), 134–140. https://doi.org/10.1038/nmat1560

[134] La-Orauttapong, D., Toulouse, J., Robertson, J. L., & Ye, Z. G. (2001). Diffuse neutron scattering study of a disordered complex perovskite crystal. Physical Review B, 64, 212101. https://doi.org/10.1103/PhysRevB.64.212101

[135] Xu, G., Shirane, G., Copley, J. R. D., & Gehring, P. M. (2004). Neutron elastic diffuse scattering study of $Pb(Mg_{1/3}Nb_{2/3})O_3$. Physical Review B, 69, 064112. https://doi.org/10.1103/PhysRevB.69.064112

[136] Dul'kin, E., Roth, M., Janolin, P. E., & Dkhil, B. (2006). Acoustic emission study of phase transitions and polar nanoregions in relaxor-based systems: Application to the $Pb(Zn_{1/3}Nb_{2/3})O_3$ family of single crystals. Physical Review B, 73, 012102. https://doi.org/10.1103/PhysRevB.73.012102

[137] Laulhé, C., Hippert, F., Kreisel, J., Maglione, M., Simon, A., Hazemann, J. L., & Nassif, V. (2006). EXAFS study of lead-free relaxor ferroelectric $Ba(Ti_{1-x}Zr_x)O_3$ at the Zr K edge. Physical Review B, 74, 014106. https://doi.org/10.1103/PhysRevB.74.014106

[138] Fu, D., Taniguchi, H., Itoh, M., Koshihara, S., Yamamoto, N., & Mori, S. (2009). Relaxor $Pb(Mg_{1/3}Nb_{2/3})O_3$: A Ferroelectric with Multiple Inhomogeneities, Physical Review Letter, 103, 207601. https://doi.org/10.1103/PhysRevLett.103.207601

[139] Miao, S., Zhu, J., Zhang, X., & Cheng, Z. Y. (2002). Electron diffraction and HREM study of a short-range ordered structure in the relaxor ferroelectric. Physical Review B, 65, 052101. https://doi.org/10.1103/PhysRevB.65.052101

[140] Shvartsman, V. V., Dkhil, B., & Kholkin, A. L. (2013). Mesoscale domains and nature of the relaxor state by piezoresponse force microscopy. Annual Review of Materials Research, 43, 423–449. https://doi.org/10.1146/annurev-matsci-071312-121632

[141] Shvartsman, V. V., & Kholkin, A. L. (2007). Evolution of nanodomains in $0.9Pb(Mg_{1/3}Nb_{2/3})O_3$-$0.1PbTiO_3$ single crystals. Journal of Applied Physics, 101(6). https://doi.org/10.1063/1.2713084

[142] Shvartsman, V. V., & Kholkin, A. L. (2012). Polar structure of $Pb(Mg_{1/3}Nb_{2/3})O_3$-$PbTiO_3$ relaxors: piezoresponse force microscopy approach. Journal of Advanced Dielectrics, 02, 1241003. https://doi.org/10.1142/s2010135x12410032

[143] Kwei, G. H., Bilinge, S. J. L., Cheong, S. -W., & Saxton, J. G. (1995). Pair-distribution functions of ferroelectric perovskites: Direct observation of structural ground states. Ferroelectrics, 164, 57-73. https://doi.org/10.1080/00150199508221830

[144] Senn, M. S., Keen, D. A., Lucas, T. C. A., Hriljac, J. A., & Goodwin, A. L. (2016). Emergence of Long-Range Order in $BaTiO_3$ from Local Symmetry-Breaking Distortions. Physical Review Letters, 116, 207602. https://doi.org/10.1103/PhysRevLett.116.207602

[145] Neilson, J. R., & McQueen, T. M. (2015). Representational analysis of extended disorder in atomistic ensembles derived from total scattering data. Journal of Applied Crystallography, 48, 1560–1572. https://doi.org/10.1107/S1600576715016404

[146] Ravel, B., Stern, E. A., Vedrinskii, R. I., & Kraizman, V. (1998). Local structure and the phase transitions of BaTiO3. Ferroelectrics, 206, 407–430. https://doi.org/10.1080/00150199808009173

[147] Cohen, R. E. (1992) Origin of ferroelectricity in perovskite oxides. Nature, 358, 136-138. https://doi.org/10.1038/358136a0

[148] Junquera, J. & Ghosez, P. (2003) Critical thickness for ferroelectricity in perovskite ultrathin films. Nature, 422, 506. https://doi.org/10.1038/nature01501

[149] Zhou, W. X. & Ariando, A. (2020) Review on ferroelectric/polar metal. JJAP, 59, SI0802. https://doi.org/10.35848/1347-4065/ab8bbf

Chapter 3. Evolution of Grain Boundaries during Phase Transitions in Barium Titanate Nanoparticles

Chapter published on Physical Review Materials, 4, 106001 (2020).

Jiecheng Diao[1,*], Xiaowen Shi[31], Tadesse A. Assefa[2], Longlong Wu[2], Ana F. Suzana[2], Daniel S. Nunes[1], Darren Batey[3], Silvia Cipiccia[3], Christoph Rau[3], Ross J. Harder[4], Wonsuk Cha[4] and Ian K. Robinson[1,2,*]

[1]*London Centre for Nanotechnology, University College London, London WC1E 6BT, UK*
[2]*Condensed Matter Physics and Materials Science Department, Brookhaven National Lab, Upton, NY 11793, USA*
[3]*Diamond Light Source, Oxfordshire, OX11 0QX, UK;*
[4]*Advanced Photon Source, Argonne National Lab, Lemont, IL 60439, USA*
Corresponding author: ucapiao@ucl.ac.uk; i.robinson@ucl.ac.uk

Abstract

In this work, ferroelastic domain walls inside $BaTiO_3$ (BTO) tetragonal nanocrystals are distinguished by Bragg peak position and studied with Bragg coherent X-ray diffraction imaging (BCDI). Convergence-related features of the BCDI method for strongly phased objects are reported. A ferroelastic domain wall inside a BTO crystal has been tracked and imaged across the tetragonal-cubic phase transition and proves to be reversible. The linear relationship of relative displacement between two twin domains with temperature is measured and shows a different slope for heating and cooling, while the tetragonality reproduces well over temperature changes in both directions. An edge dislocation is also observed and found to annihilate when heating the crystal close to the phase transition temperature.

I. Introduction

Perovskite transition-metal oxides have been studied for decades because of both their broad applications and fundamental scientific questions. The displacement of Ti and Ba ions relative to the oxygen in unit cell leads to local polarization, which gives rise to exotic electrical properties such as elevated dielectric susceptibility, ferroelectricity and piezoelectricity [1-4]. By analogy with well-studied magnetic systems, it is believed that it is not the local polarization in unit cell level that directly links with these macroscopic electrical properties, but rather via the formation and rearrangement of polarized nanodomains. Therefore, the study of domain structures, preferably in three dimensions (3D), is important for understanding and improving these properties. $BaTiO_3$ (BTO), for example, is frequently chosen as a lead-free functional material for both actuator and sensor applications [5-6]. It goes through a series of crystal lattice systems: cubic, tetragonal, orthorhombic and rhombohedral upon cooling [7]. The corresponding transitions are first-order with critical temperatures of 393K, 278K and 183K, respectively, which can be adjusted by varying strain and sample size. The cubic-tetragonal phase transition temperature, for example, can be increased from 393K to 813K with 1.7% compressive strain [8] and can decrease to room temperature when the

---

- [1] Current affiliation: Department of Physics, New Mexico State University, Las Cruces, New Mexico 88003, USA
- & Department of Materials Science and Engineering, Rensselaer Polytechnic Institute, 110 8th Street, Troy, NY, 12180, USA

particle size is reduced to 3nm [9]. Recently, it was reported that the local structure remains locally rhombohedral throughout all phases [10,11].

The phase transition is also complex, demonstrating both order-disorder and displacive character [12,13]. From the high symmetry cubic phase to the lower symmetry tetragonal phase, the paraelectric ensemble breaks into ferroelectric domains of uniform electric polarization, driven by the minimization of the sum of electrostatic and elastic energy [1-4]. To accommodate local energy landscape and strain, different types of domains could be formed by rotation or translation of crystal regions or domains into different locations with well-defined domain-wall interfaces. For example, there are 71°, 109° and 180° domain walls in rhombohedral BTO [14]. In tetragonal BTO, the flipping of one region of a crystal along a face-diagonal leads to a ferroelectric and ferroelastic 90° domain wall (twin boundary). While flipping along the long side of the tetragonal unit cell creates a ferroelectric-only 180° domain wall instead, in which the a-domain and c-domain are formed head-to-tail with each other [15-17]. The domain wall is said to be continuous which means it can only end in other domain walls or grain boundaries [18]. There are discontinuities of polarization in the perpendicular direction of domain walls, where the local displacements would be expected to accumulate. The formation of these domains depends strongly on boundary conditions, such as sample shape, while the size of domains in thin films has a square-root dependence on thickness, known as the Kittel scaling law [19].

Bragg coherent X-ray diffraction imaging (BCDI) is a synchrotron-based lens-less imaging method, which is well adapted to studying nanocrystals in three dimensions (3D). It is capable of imaging the shape and mapping out inner strain without damaging the nanocrystal [20-22]. In the BCDI experiment, the 3D diffraction pattern is collected in reciprocal space and inverted to real space with advanced phase retrieval algorithms [20]. Usually, a single hkl Bragg peak is selected in the reciprocal lattice with a total momentum transfer vector $\mathbf{Q} = h\mathbf{a}^* + k\mathbf{b}^* + l\mathbf{c}^*$. In a completely general way, this gives a 3D complex image of the crystal, capturing both its electron density function as the complex amplitude signal and a projection of the distortions as the corresponding phase signal. A simple linear relationship exists between the crystal displacement field $\mathbf{u}(\mathbf{r})$ and the observed image phase, $\phi(\mathbf{r}) = \mathbf{Q}\bullet\mathbf{u}(\mathbf{r})$ [20]. The amplitude, representing the average electron density, contains information about crystallinity and its isosurface can be used to visualize the shape of crystal. Any local displacement of the unit cells of the crystal parallel to $\mathbf{Q}$ will change the relative phase of the scattering from those unit cells relative to the rest of the crystal; when this occurs in regions large enough to be resolved the distortion can be visualized as a region or domain with a measurable phase appearing in the image. When the phase shift exceeds 2π, a proper phase unwrapping operation is needed to preserve the continuity of the displacement field.

The BCDI technique is sensitive to defects and has the unique ability to identify the dislocations and grain boundaries inside crystals by their characteristic strain (displacement) patterns [23-26]. The interpretation of the phase as a projection of the displacement field is analogous to the Generalized Phase Approximation (GPA) used to interpret Transmission Electron Microscopy (TEM) images [27]. There have already been several studies of BTO by BCDI motivated by the ability to see its important domain structures. An important example is the discovery of an interesting electric-field driven vortex structure [28-30]. Here we take advantage of the unique properties of BCDI to investigate the domain structure and dislocations inside BTO nanocrystals upon crossing the cubic-tetragonal phase transition. In this work, we extend the BCDI method

by considering the case of two nearby overlapping Bragg peaks, originating from different regions or domains of the same nanocrystal, to explore the structure and properties of the domain walls formed between them.

II. Experimental Methods

Commercial BTO powders with a nominal size of 200nm were diluted in a solution of Tetraethyl Orthosilicate (TEOS) and ethanol at a ratio of 1:75 in volume. This solution was then drop casted onto the silicon wafer and annealed in the furnace at around 700°C for 1h. This forms an amorphous SiO_2 bonding matrix, which is a common procedure for fixing nanoparticles on to a substrate in BCDI experiments, in order to avoid its movement due to beam pressure [31].

Ex-situ and In-situ experiments reported in this work were performed at two beamlines specialized in BCDI. At Advanced Photon Source (APS), beamline 34-ID-C uses a Kirkpatrick-Baez (KB) mirror focusing system to match a 70×30 um^2 spatially coherent beam at 55m from the source to the size of the sample. This gives a good signal level from 200nm BTO nanocrystals. At Diamond Light Source (DLS) beamline I-13-1, we used a 400um aperture 220m from the source to cut out a spatially coherent beam, which was focussed by a Fresnel Zone Plate (FZP) to the size of the sample. The signal level from this latter system was found to be at least ten times weaker. In both cases the sample was rotated in the coherent, monochromatic, focussed beam and the diffraction pattern was collected on a Medipix-technology area detector. At APS, the detector distance was variable and for the measurement reported in this manuscript, we keep the detector at D=0.45m. While at DLS, the detector was fixed at D=2.8m.

When the beam is coherent over the dimensions of the sample, its diffraction pattern acquires interference fringes surrounding each Bragg peak. This diffraction pattern from the nanocrystal was measured in three dimensions at the 101 or 110 Bragg peaks by rotating the sample stage over a short range, typically $\pm0.1°$ to $\pm0.5°$. This rocking curve scan is equivalent to the 2D detector plane sweeping across the Ewald sphere and capturing the 3D volume of reciprocal space around the Bragg peak [20]. The amplitude of the diffracted X-ray is the square root of intensity, while the phase information is lost. This famous phase problem is solved by iterative algorithms, using the additional information obtained by oversampling the intensity distribution in the fringes of the coherent diffraction pattern surrounding the Bragg peak. In this work, a combination of Error-Reduction (ER) and Hybrid Input-output (HIO) algorithms are used to iteratively retrieve the phase until the error between the amplitude of the reconstruction and measured diffraction patterns decreased close to 0.1% [32].

III. Domain walls in tetragonal BTO nanocrystals

At room temperature, the 200nm BTO nanocrystals have tetragonal structure, in which case the 90° and 180° type domain walls (DWs) are favourable because they are mechanically compatible with each other without crystal misfit and are electrically neutral. 90° type DWs separate ferroelastic and ferrolelectric domains, while 180° type DWs separate pure polarization domains. Figure 1 shows an example of a crystal twin structure captured inside a single tetragonal BTO nanocrystal. Figure 1a and 1c show the diffraction patterns of the 101 peak and the 110 peak from differently oriented tetragonal regions of the same crystal. The omega angle difference between the centers of mass (COM) of these two diffraction patterns is 0.6°. There are interference fringes crossing the entire reciprocal space region spanning between the two diffraction

patterns centers seen on the area detector. Figure 1b shows the fringes on the detector frame at the angle in the middle of the two COMs. The observation of continuous fringes is a clear indication that the 110 and the 101 peaks come from the same coherence volume in real space, so that their diffraction patterns can interfere coherently. This identifies them as coming from substructures of the same nanoparticle. This is confirmed by gradually moving the sample piezo stages transverse to the beam direction, and seeing that the intensities of the two peaks increase and decrease simultaneously in a 100nm size X-ray beam. This confirms the Bragg intensities are coming from the same nanoparticle, for which the intensity variation is attributed to crystal moving in and out of the X-ray beam.

The diffraction patterns of the two peaks were reconstructed separately. Figure 1(d) is the reconstructed image from the 101 diffraction pattern in Figure 1(a), where the shape is plotted as an isosurface (single 3D contour level) of the amplitude and the surface is color-cued with the local value of the phase. There are two separate domains with a 50nm wide gap in between. The two domains both have the same crystal orientation because they both contribute to the same 101 Bragg peak, but they have different phases (displacements, denoted by color in Figure 1(d)). This shows that the origins of their unit cells are shifted relative to each other. The average phases for the two 101 domains are -1.259 ± 0.004 and 0.546 ± 0.003 rad, respectively. Because the phase can only be determined modulo 2π, this phase difference corresponds to a displacement of $2.835*n+0.813$Å between the two pieces along the Q-direction, where the n is an integer. 2.835Å is the {101} d-spacing of BTO. The missing volume in between the two pieces implies there must be a third object, presumably an inserted piece of crystal with a different orientation, filling the gap. Figure 1(f), the reconstructed 3D image of the 110 pattern of figure 1(c), reveals a 50nm plate-shaped crystal, which is the missing part. The two reconstructed images in Figure 1(d) and 1(f) fit together well with each other, as shown in Figure 1e. We conclude that two 90° domain walls exist in the same nanoparticle, which are parallel in this case. The polarization direction would change across a ferroelastic domain wall, in the way that is illustrated in figure 1(g).

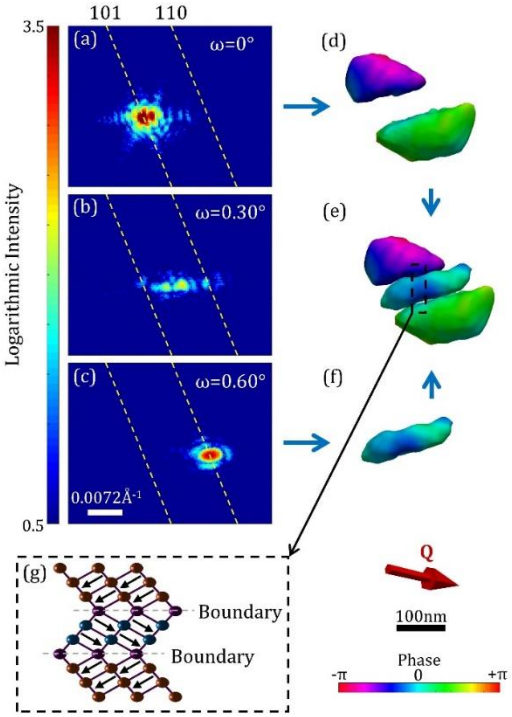

Figure 1. Ferroelastic domain walls in $BaTiO_3$ nanocrystal at room temperature. (a)-(c) Diffraction patterns of a $BaTiO_3$ nanocrystal at the angles indicated. The location of the 101 and 110 powder rings on the area detector is plotted with yellow dash lines as guides to the eye. Omega is the self-rotation angle of the sample stage. (d) & (f) Reconstructed images of 101 and 110 diffraction patterns in (a) and (c), respectively, shown as isosurfaces of amplitude to give the shape of crystal. The colour on the shape of nanocrystal represents the complex phase, which can be reverted to displacement of crystal unit-cell origins. (e) A joint view of (d) and (f), which gives a good match in shape. (g) A sketch of the two parallel ferroelastic domain walls inferred from these data at the position indicated by a black box in (e), which shows changes in the polarization direction upon crossing domain wall. The Q direction is denoted, which is determined by the difference of the incident and diffracted X-ray beam wave-vectors. It denotes the Bragg reflection that was measured. The isosurface plots here and in the other figures were generated using the 3D visualization software Paraview [33].

In analyzing the 3D diffraction data to obtain these BCDI reconstructions, it was found to be effective to arbitrarily cut clearly split diffraction peaks into two halves and to reconstruct the two peaks separately before reassembling them. The cropping of intermediary fringes between the two peaks did not seriously distort the resulting images, perhaps because the contribution of the fringes was at a low level relative to the peak centers. Further details of the influence of the cropping are presented in the Supplementary Information (SI). When the diffraction patterns of nanoparticle in Figures 1 was reconstructed without splitting, shown in Figure S3, there was found to be seriously misaligned with missing volumes in both cases. The combined double diffraction patterns, complete with the intermediary fringes, should still be the Fourier transform of the complete, assembled particle, so we would like to understand the reasons for this reconstruction failure. Similar misbehavior was reported for calculated diffraction patterns of a model nanocrystal containing an epitaxial interface between regions of different lattice constant [35]. We, therefore, undertook simulations of double diffraction patterns from known structures.

IV. Simulated BTO bicrystal nanoparticles

Simulations were performed to test this behavior of the reconstruction algorithms, which are shown in Figure 2. A model BTO nanoparticle, resembling that of Figure 1, with three domains was built in a 512×512×512 array. The two domains on the top and bottom have a hemispherical shape with a 32 pixels radius, while the middle domain has a cylinder shape that matches the two hemispheres with a height of 16 pixels. The object was Fourier transformed to generate its diffraction pattern, whose amplitude was then reconstructed using the usual algorithms [20]. The diffraction pattern and reconstructed images are presented in Figure 2(a) and 2(e). Then the object was split into separate arrays for the hemispheres and the cylinder, separately Fourier transformed and then recombined as complex diffraction patterns to preserve the interference between the parts. When the two centers were the same, the result is shown in Figure 2(a), while the split peak behavior was simulated offsetting the diffraction patterns before they were added together, using different gaps between the diffraction pattern from middle cylinder domain and the pattern from the two hemispheres, shown in Figure 2(b-d).

The 3D diffraction patterns in Figure 2(a-d) were recentered to their common center of mass (COM) before phase retrieval using the standard methods to give the images in Figure 2(e-h) [20]. Moving the two patterns apart from each other, making them misaligned from the array center, is equivalent to introducing phase ramps inside each of the particle segments in real space. From the definition of the discrete Fourier transform, it can be seen that each single pixel shift in reciprocal space corresponds to a 2π phase ramp across the array in real space. When the gap between two patterns was 5 pixels in Figure 2(b) and 2(f), the reconstruction was successful: the crystal still has the full shape, but there is an opposite phase gradient generated introduced in the different domains, positive for the cylinder and negative for the hemispheres. When the gap was increased to 15 pixels, in Figure 2(c) and 2(g), the ramp becomes stronger, as expected, but the middle domain becomes misaligned and displaced into one side. There are missing crystal volumes inside the middle cylinder domain. Finally, when the gap reached 40 pixels, in Figure 2(d) and 2(h), the middle domain becomes completely misaligned. Strong phase ramps and distorted density showed up in the middle cylinder domain and there is a phase gradient in two hemisphere domains.

This behavior of the reconstruction algorithms is presently unexplained, but the simulation results do reproduce the experimental behavior found in Figure S3. We have nevertheless confirmed that the peak splitting is the cause of the apparent misalignment of reconstructed domains. It also justifies our strategy of reconstructing the split peak diffraction patterns separately and manually overlaying the images, which also avoids removing the phase ramps, which would have appeared otherwise. For the nanoparticle in Figure 1, the splitting of two peaks, due to twin boundary, gave separate reflections at 101 and 110. The peak separation in reciprocal space is of order $0.02Å^{-1}$, which is considerably more than the 15 pixels needed to disrupt the correct reconstruction of the model ensemble nanoparticle in Figure 2(c). This double peak reconstruction failure using standard method is also reported in simulation works, where different algorithms are proposed to solve this problem [35].

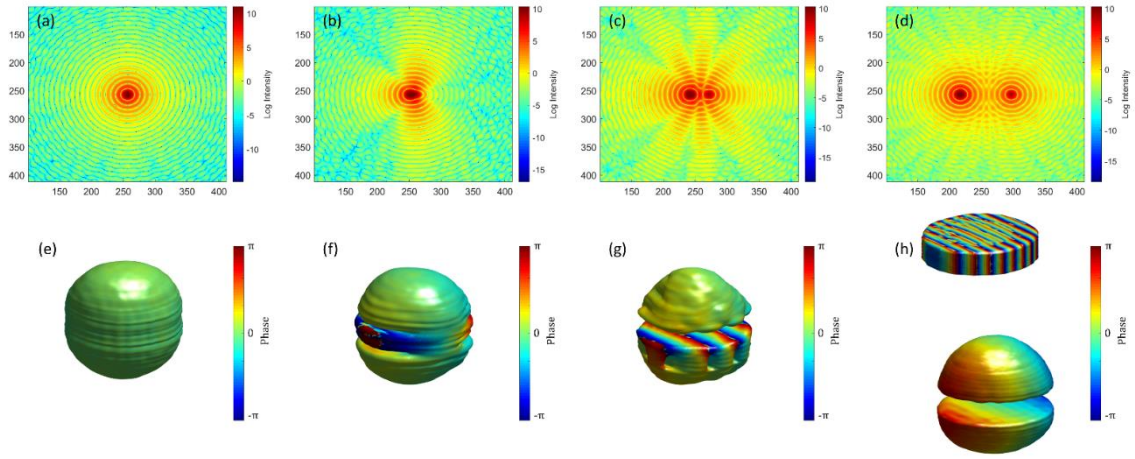

Figure 2. Simulation of split peak diffraction pattern reconstructions. A nanoparticle with three domains was used to generate a 3D diffraction pattern of which the central slice is shown in a 512×512 pixel array. The two peaks corresponding to the hemispherical sides and cylindrical center were given an extra gap offsetting the two diffraction patterns by 0, 5, 15, 40 pixels from (a) to (d). Their reconstructed images are shown as isosurfaces colored by the image phase in (e) to (h), respectively.

V. Evolution of ferroelastic domain walls under phase transition

A 200nm BTO nanoparticle showing the twin-peak diffraction pattern was selected at 387.2K. Similar to the example in Figure 1, it had its two peaks sitting on the 101 and 110 powder rings indicating the presence of an internal ferroelastic domain wall. Figure 3 shows the BCDI reconstruction, obtained directly from the double peak diffraction pattern, which clearly shows a 90° domain wall inside. At this elevated temperature, the peaks were close enough to reconstruct together without requiring separating. The cross-section view in Figure 3 shows the domain wall and two separated domains. The crystal planes of the two domains can be said to be parallel since they both have constant phase inside and there is a sharp jump of the displacement field across the twin boundary. The phase ramps caused by splitting peak is negligible compared with the large phase difference caused by domain walls, as indicated by standard error of average displacement in SI. This crystal also shows a small hole and spiral-shaped displacement distribution around the hole, which is an indication of a dislocation, whose details are discussed below. This nanoparticle was chosen to be tracked during heating across the tetragonal-to-cubic phase transition temperature, nominally at 393K.

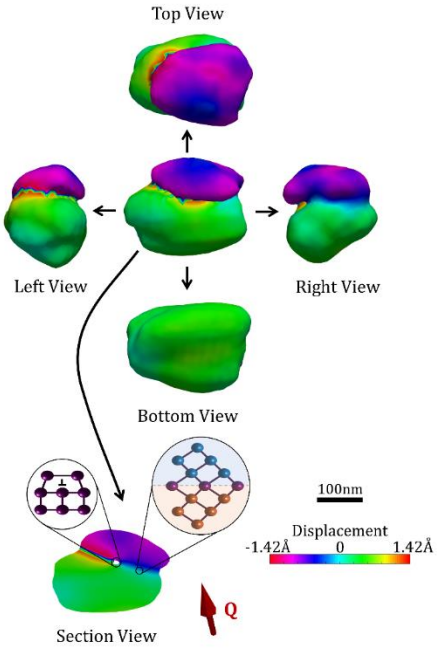

Figure 3. BCDI isosurface image of a $BaTiO_3$ nanoparticle containing two domains separated by a ferroelastic domain wall at 387.2K. Five orthogonal views and a cross-section are shown, as labelled, along with the Q vector for the section view.

Figure 4 shows a series of reconstructed images and corresponding slice of this nanoparticle bi-crystal going from tetragonal structure to cubic structure and back to tetragonal structure again by changing the temperature. When heating up the crystal before the phase transition, the shape of the crystal remains unchanged, but the relative displacement of the two domains (color) becomes small. After heating up to the cubic structure, the two domains are seen to merge into a single-color shape. Now in the cubic phase, the displacement differences have diminished, while new regions of both tensile and compressive strain have appeared on the surface of the image. When the crystal is cooled down back into the tetragonal phase, the twin boundary comes back at the same position, so this transformation appears to be reversible, showing that the domain wall location is remembered by the nanoparticle.

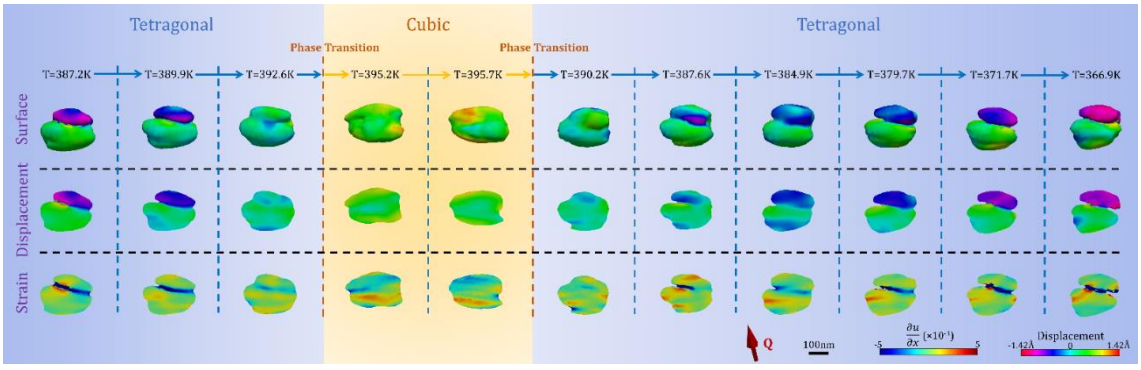

Figure 4. Images of a $BaTiO_3$ nanoparticle upon crossing through its tetragonal-cubic phase transition. The top row is a series of contour views of the isosurface. The second row shows phase (displacement) cross-section maps taken in the middle of the nanocrystal, while the bottom row shows strain (a derivative of displacement) maps as a function of temperature.

The measured relative displacement of the two domains during heating up and cooling down are shown in Figure 5(a) in solid line. The displacement field decreases when increasing the temperature and *vice versa*. The standard error of each point is discussed in the SI. Close to phase transition temperature, there appears to be a linear relationship of displacement difference with temperature on both heating and cooling. However, the slope during cooling is -0.21, which is steeper than -0.48 while heating up. The goodness of fit is discussed in the SI. The tetragonality of this crystal during heating and cooling, derived from the position of diffraction peak center, are shown in Figure 5(a) in dash line. Comparing with both, the tetragonality reproduces well. However, there is a clear delay in the displacement field between cooling and heating. This difference in slope can be thought of as a form of hysteresis, commonly observed in phase transitions, coupled with the experimental limitation of waiting a sufficient time for the structure to equilibrate at each temperature.

To estimate the width of the domain wall, the displacement is plotted along a line passing vertically in Figure 3 across the twin boundary in the region away from the dislocation, shown in Figure 5(b). The width of the domain wall, where the sharp displacement slope could be seen, is below 30nm, which is the estimated spatial resolution of the image. The change of the phase across the step between the two crystals has a clear temperature dependence as the phase transition at T=393K is approached.

The displacement inside a domain is interpreted as the crystal distortion projected onto the Q vector, or crystal plane displacement determined by the Bragg reflection. The average displacement between the ferroelastic domains is not caused by the accumulation of crystal distortion, but the structure of the ferroelastic domain wall instead. Because our spatial resolution is the same as the observed width of domain wall, the structure of the domain wall cannot be resolved and the displacement is smeared out at the domain wall position, as seen in Figure 5(b). However, the relative displacement between the two domains is a good way to quantify the influence of a ferroelastic domain wall when the temperature changes. In this case, the relative displacement between the two domains is seen to increase linearly near the phase transition temperature. The reason for this change is not clear. There are possibilities that this change is coupled with the changing of domain wall width, or the local distortion at the domain wall becomes sharper due to the change of tetragonality.

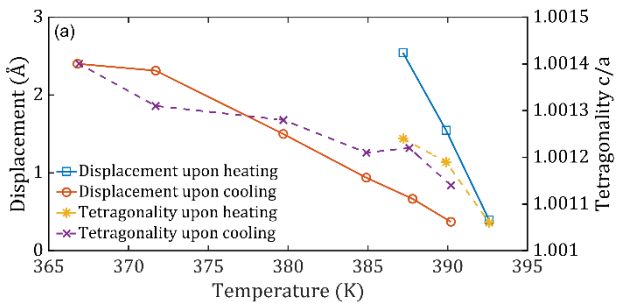

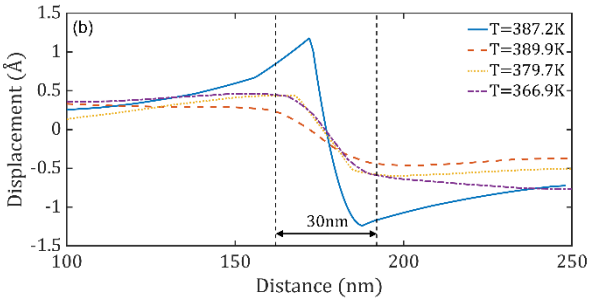

Figure 5. (a) Average displacement difference between the two domains upon heating and cooling are shown in solid line. Tetragonality of this crystal over heating and cooling are shown in dash line. (b) Line plot of displacement over distance across the twin boundary.

VI. Dislocation annihilation upon heating

Figure 6(a) and 6(b) show further details of the dislocation at the center of the ferroelastic domain wall inside the bicrystal. When the temperature is 387.2K, the dislocation is located at the center of crystal. The length of this dislocation is 178nm. Upon heating up to 389.9K, this dislocation is found to move to the left side and the length decreases to 125nm. Further heating up to 392.6K, although the crystal is still in the tetragonal phase, causes the dislocation to diminish again and then disappear. This dislocation does not come back during the cooling stage of the experiment.

To identify the type of dislocation, the displacement field surrounding the low electron density core is plotted as a function of rotation angle in Figure 6(c). The experimental data show a roughly linear trend of crystal displacement over angle superimposed with two clear modulations. This is the characteristic of an edge dislocation, for which is superimposed the simulated displacement field according to linear elastic theory (LET), with details provided in the Appendix. The experimental data give a reasonable match with the simulated results.

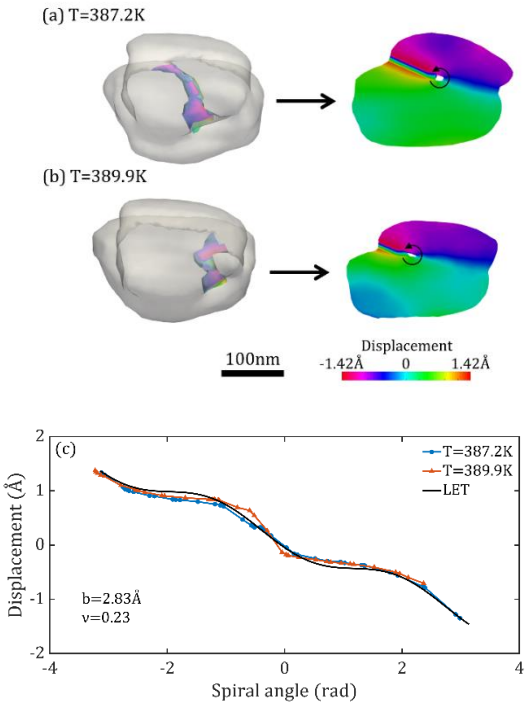

Figure 6. Dislocation annihilation upon heating. (a) Reconstructed crystal image at 387.2K. (left) A dislocation line through crystal is coloured. (right) A slice view across the dislocation line. (b) Same as (a), but temperature is 389.9K. (c) displacement field plotted vs rotation angle around the low-density core. Both experimental results and simulated curve from linear elastic theory are presented.

VII. Conclusion

We studied the structure and arrangement of domain walls in 200nm BTO nanoparticles by BCDI both at ambient temperature and across the tetragonal-cubic phase transition temperature. Domains and domain walls are commonly found in these particles, giving rise to split coherent diffraction peaks. For successful BCDI reconstruction with large peak split, it was necessary to separate the peaks and manually reassemble the reconstructed 3D images afterwards. Ferroelastic domain walls were identified and characterized at room temperature. At temperatures close enough to the tetragonal-cubic phase transition, the split peaks of a particle containing a ferroelastic domain wall were successfully reconstructed using both peaks together. This allowed us to determine the sub-Ångstrom relative displacement between two domains, tracking its disappearance on approaching the phase transition to cubic phase and reappearance when cooling back to tetragonal phase. We found a linear relationship between the relative displacement of the two 90° domains over heating and cooling close to the tetragonal-cubic phase transition. The domain wall location was reproducible in this 200nm BTO nanoparticle. An edge dislocation line was found at the center of the twin boundary inside this crystal close to the transition temperature. This dislocation annihilated upon ramping up the temperature and did not return upon cooling.

Acknowledgement

The work was supported by the UK EPSRC grant EP/I022562/1 and the China Scholarship Council (CSC). Work at Brookhaven National Laboratory was supported by the U.S. Department of Energy, Office of Science, Office of Basic Energy Sciences, under Contract No. DE-SC0012704. Work at the Advanced Photon Source (APS) was supported by the U. S. Department of Energy, Office of Science, Office of Basic Energy Sciences, under Contract No. DE-AC02-06CH11357. The beamline 34-ID-C was built with funds from U.S. National Science Foundation grant DMR-9724294.

Appendix A: Identification of dislocation in Figure 6

BCDI has the ability to locate the dislocation line inside a nanoparticle and identify the type of dislocation line by its characteristic strain field. The characteristic feature of any dislocation is a low-density core in the Bragg density map and a phase/displacement field around this core. A screw dislocation has a linear relation of displacement as a function of orientation angle given by [20]:

$$u_{screw} = \frac{b}{2\pi} * \theta$$

[u_{screw}: displacement field around screw dislocation; b: Burgers vector; θ: spiral angle around screw dislocation]

An edge dislocation has linear relation plus 2 modulations given by the extra atomic planes [21]:

$$u_{edge} = \frac{b}{2\pi} * \left(\theta + \frac{\sin(2\theta) - \cos(2\theta)}{4-4\nu} + \frac{(4\nu-2) * log^{r}}{4-4\nu}\right)$$

[u_{edge}: displacement field around the edge dislocation; b: Burgers vector; θ: spiral angle around the edge dislocation; r: radius of the circle around the edge dislocation; ν: Poisson's ratio of the material.]

In this case, the simulated edge dislocation displacement field is plotted in figure 7(c). The radial distance r is 30nm and Poisson's ration is 0.23. The value of the Burgers vector is 2.83Å, which is the d-spacing of the corresponding lattice plane.

Reference

[1] P. Zubko, S. Gariglio, M. Gabay, P. Ghosez, and J. -M. Triscone, Annu. Rev. Condens. Matter Phys. **2**, 141. (2011). https://doi.org/10.1146/annurev-conmatphys-062910-140445

[2] D. G. Schlom, L. Q. Chen, C. B. Eom, K. M. Rabe, S. K. Streiffer, and J. -M. Triscone, Annu. Rev. Mater. Res. **37**, 589 (2007). https://doi.org/10.1146/annurev.matsci.37.061206.113016

[3] A. R. Damodaran, J. C. Agar, S. Pandya, Z. Chen, L. Dedon, R. Xu, B. Apgar, S. Saremi, and L. W. Martin, J. Condens. Matter Phys. **28**, 263001 (2016). https://doi.org/10.1088/0953-8984/28/26/263001

[4] C. H. Ahn, K. M. Rabe, and J. -M. Triscone, Science **303**, 488 (2004). https://doi.org/10.1126/science.1092508

[5] P. Keller, H. Ferkel, K. Zweiacker, J. Naser, J. -U. Meyer, and W. Riehemann, Sensors and Actuators B **57**, 39 (1999). https://doi.org/10.1016/S0925-4005(99)00151-3

[6] J. Gao, D. Xue, W. Liu, C. Zhou, and X. Ren, Actuators **6**, 24 (2017). https://doi.org/10.3390/act6030024

[7] A. von Hippel, Rev. Mod. Phys. **22**, 221 (1950). https://doi.org/10.1103/RevModPhys.22.221

[8] K. J. Choi, M. Biegalski, Y. L. Li, A. Sharan, J. Schubert, R. Uecker, P. Reiche, Y. B. Chen, X. Q. Pan, V. Gopalan, L.-Q. Chen, D. G. Schlom, and C. B. Eom, Science **306**, 1005 (2004). https://doi.org/10.1126/science.1103218

[9] J. E. Spanier, A. M. Kolpak, J. J. Urban, I. Grinberg, L. Ouyang, W. S. Yun, A. M. Rappe, and H. Park, Nano. Lett. **6**, 735 (2006). https://doi.org/10.1021/nl052538e

[10] J. Hlinka, T. Ostapchuk, D. Nuzhnyy, J. Petzelt, P. Kuzel, C. Kadlec, P. Vanek, I. Ponomareva, and L. Bellaiche, Phys. Rev. Lett. **101**, 167402 (2008). https://doi.org/10.1103/PhysRevLett.101.167402

[11] Y. Isohama, N. Nakajima, H. Maruyama, Y. Tezuka, and T. J. Iwazumi, Electron Spectros, **184**, 207 (2011). https://doi.org/10.1016/j.elspec.2010.12.023

[12] E. A. Stern, Phys. Rev. Lett. **93**, 037601 (2004). https://doi.org/10.1103/PhysRevLett.93.037601

[13] M. B. Smith, K. Page, T. Siegrist, P. L. Redmond, E. C. Walter, R. Seshadri, L. E. Brus, and M. L. Steigerwald, J. Am. Chem. Soc. **130**, 6955 (2008). https://doi.org/10.1021/ja0758436

[14] M. Taherinejad, and D. Vanderbilt, Phys. Rev. Lett. **86**, 155138 (2012). https://doi.org/10.1103/PhysRevB.86.155138

[15] A. S. Everhardt, S. Matzen, N. Domingo, G. Catalan, and B. Noheda, Adv. Electron. Mater. **2**, 1500214 (2016). https://doi.org/10.1002/aelm.201500214

[16] A. Schilling, T. B. Adams, R. M. Bowman, J. M. Gregg, G. Catalan, and J. F. Scott, Phys. Rev. B **74**, 024115 (2006). https://doi.org/10.1103/PhysRevB.74.024115

[17] L. J. McGilly, A. Schilling, and J. M. Gregg, Nano Lett. **10**, 4200 (2010). https://doi.org/10.1021/nl102566y

[18] G. Catalan, Springer series in materials science, vol 198. Springer, Berlin, Heidelberg (2014). https://doi.org/10.1007/978-3-642-55375-2_9

[19] G. Catalan, J. Seidel, R. Ramesh, and J. F. Scott, Rev. Mod. Phys. **84**, 119 (2012). https://doi.org/10.1103/RevModPhys.84.119

[20] I. Robinson, and R. Harder, Nat. Mater. **8**, 291 (2009). https://doi.org/10.1038/nmat2400

[21] G. Xiong, O. Moutanabbir, M. Reiche, R. Harder, and I. Robinson, Advanced Materials **26**, 7747 (2014). https://doi.org/10.1002/adma.201304511

[22] T. A. Assefa, Y. Cao, J. Diao, R. J. Harder, W. Cha, K. Kisslinger, G. D. Gu, J. M. Tranquada, M. P. M. Dean, and I. K. Robinson, Phys. Rev. B **101**, 054104 (2020). https://doi.org/10.1103/PhysRevB.101.054104

[23] J. N. Clark, J. Ihli, A. S. Schenk, Y.-Y. Kim, A. N. Kulak, J. M. Campbell, G. Nisbet, F.C. Meldrum, and I. K. Robinson, Nat. Mater. **14**, 780 (2015). https://doi.org/10.1038/nmat4320

[24] U. Ulvestad, A. Singer, J. N. Clark, H. M. Cho, J. W. Kim, R. Harder, J. Maser, Y. S. Meng, and O. G. Shpyrko, Science **348**, 1344 (2015). https://doi.org/10.1126/science.aaa1313

[25] S. Labat, M. I. Richard, M. Dupraz, M. Gailhanou, G. Beutier, M. Verdier, F. Mastropietro, T. W. Cornelius, T. U. Schulli, J. Eymery, and O. Thomas, ACS Nano **9**, 9210 (2015). https://doi.org/10.1021/acsnano.5b03857

[26] X. Huang, W. Yang, R. Harder, Y. Sun, M. Lu, Y. S. Chu, I. Robinson, and H. K. Mao, Nano Letters **15**, 7644 (2015). https://doi.org/10.1021/acs.nanolett.5b03568

[27] M. Hytch, F. Houdellier, F. Hue, E. Snoeck, Nature **453**, 1086 (2008) https://doi.org/10.1038/nature01638

[28] D. Karpov, Z. Liu, T. dos Santos Rolo, R. Harder, P. V. Balachandran, D. Xue, T. Lookman, and E. Fohtung, Nat. Commun. **8**, 280 (2017). https://doi.org/10.1038/s41467-017-00318-9

[29] K. Ohwada, K. Sugawara, T. Abe, T. Ueno, A. Machida, T. Watanuki, S. Ueno, I. Fujii, S. Wada, and Y. Kuroiwa, Jpn. J. Appl. Phys. **58**, SLLA05 (2019). https://doi.org/10.7567/1347-4065/ab38dd

[30] R. Harder, and I. Robinson, JOM. **65**, 1202 (2013). https://doi.org/10.1007/s11837-013-0682-4

[31] M. Monteforte, A. K. Estandarte, B. Chen, R. Harder, M. H. Huang, and I. Robinson, J. Synchrotron Rad. **23**, 953 (2016). https://doi.org/10.1107/S1600577516006408

[32] J. R. Fienup, Appl. Opt. 21, 2758 (1982). https://doi.org/10.1364/AO.21.002758

[33] J. Ahrens, B. Geveci and C. Law, ParaView: an end-user tool for large data visualization. Elsevier, Visualization Handbook (2005) https://doi.org/10.1016/B978-012387582-2/50038-1

[34] J. Diao, M. Cherukara, R. Harder, X. Huang, F. Zhang, B. Chen, A. Ulvestad, S. Song, D. Zhu, D. Keen, I. Robinson, Crystals **10**, 365 (2020). https://doi.org/10.3390/cryst10050365

[35] Z. Wang, O. Gorobtsov, A. Singer, New J. Phys. **22**, 013021 (2020). https://doi.org/10.1088/1367-2630/ab61db

Supplement Information: Evolution of Grain Boundaries during Phase Transitions in Barium Titanate Nanoparticles

Jiecheng Diao[1,*], Xiaowen Shi[32], Tadesse A. Assefa[2], Longlong Wu[2], Ana Flávia Suzana[2], Daniel S. Nunes[1], Darren Batey[3], Silvia Cipiccia[3], Christoph Rau[3], Ross J. Harder[4], Wonsuk Cha[4] and Ian K. Robinson[1,2,*]

[1]*London Centre for Nanotechnology, University College London, London WC1E 6BT, UK*
[2]*Condensed Matter Physics and Materials Science Department, Brookhaven National Lab, Upton, NY 11793, USA*
[3]*Diamond Light Source, Oxfordshire, OX11 0QX, UK;*
[4]*Advanced Photon Source, Argonne National Lab, Lemont, IL 60439, USA*
Corresponding author: ucapiao@ucl.ac.uk; i.robinson@ucl.ac.uk

1. Robustness of fringe cropping and its influence on final reconstruction

We studied the influence of fringes between twin peaks (e.g. Figure 1b) on the quality of the final reconstruction.

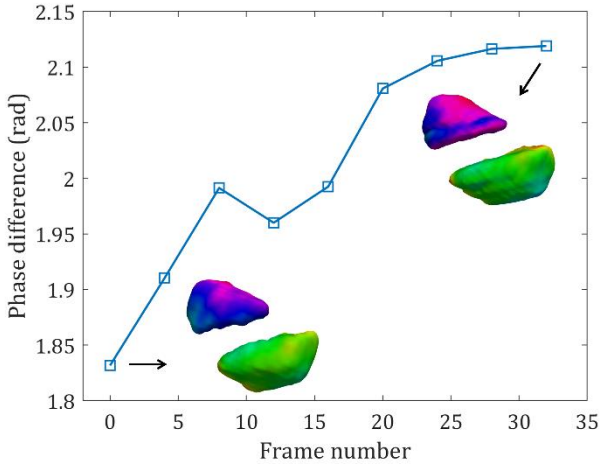

Figure S1. Phase difference of two domains after adding different numbers of frames containing intermediary fringe.

[2] Current affiliation: Department of Physics, New Mexico State University, Las Cruces, New Mexico 88003, USA

& Department of Materials Science and Engineering, Rensselaer Polytechnic Institute, 110 8th Street, Troy, NY, 12180, USA

In this case, by adding more of the intermediary fringe frames into the reconstruction, the shape of the crystal, which is defined by Bragg density, remains largely unchanged. However, the relative displacement between the two domains was found to increases gradually and approaches a maximum of 0.2873 rad difference when adding all the fringes. The resolution is expected to improve slightly with more fringes. In this case, however, the resolution was found to remain around 8.4nm.

A redrawing of Figure 1, after taking all the fringes into the reconstruction, is shown in Figure S2.

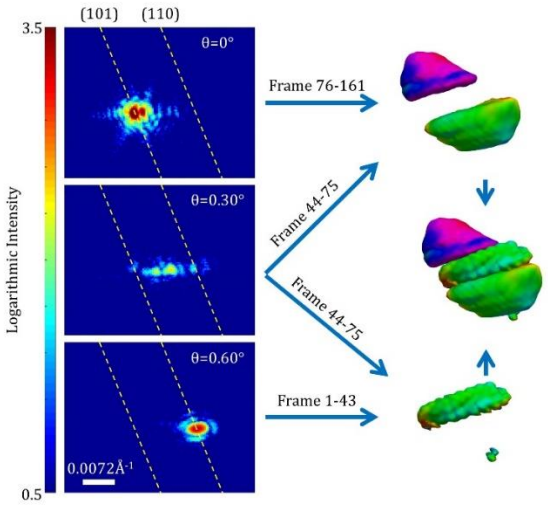

Figure S2. Reconstruction of the separated Bragg peaks with all the intermediary fringes added to both peaks.

2. Combine reconstruction of crystal in Figure 1.

The diffraction patterns in Figure 1 were reconstructed by separating the two Bragg peaks and manually merging the resulting images. If instead, the reconstructions were carried out on the full data without cropping or separating the peaks, the results are shown in Figure S3. For crystal 1 in Figure S3a, the middle domain is misaligned and moved to far side.

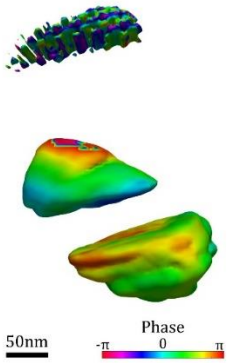

Figure S3. Full-data reconstructed images of the nanoparticles shown in Figure 1.

3. Displacement field difference of the nanoparticle in Figure 3.

To calculate the average displacement field of each grain, the nanoparticle is split at its twin domain boundary, as shown in Figure S4. Because of the discontinuity near the twin boundary, so the volume within 30nm of the boundary is not counted. The average displacement of each region and the displacement difference is listed in Table S1 along with its standard error.

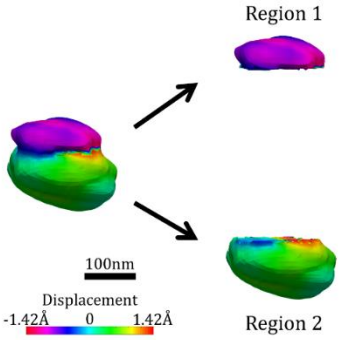

Figure S4. Splitting the nanoparticle into two regions at its twin boundary. The region near the twin boundary is omitted when calculating the average displacement of that region.

Table S1. Measured average displacement of the grains and their difference of the crystal in Figure 3.

	Temperature (K)	Average displacement of region 2 (Å)	Average displacement of region 1 (Å)	Displacement difference (Å)
Heating up	387.2	0.381±0.001	-0.764±0.003	1.145±0.003
	389.9	0.085±0.002	-0.612±0.003	0.697±0.003
	392.6	0.105±0.002	-0.072±0.005	0.177±0.005
Cooling down	390.2	0.113±0.002	-0.055±0.008	0.167±0.008
	387.6	0.137±0.003	-0.163±0.005	0.300±0.005
	384.9	0.075±0.003	-0.347±0.003	0.423±0.003
	379.7	0.240±0.002	-0.435±0.003	0.675±0.003
	371.7	0.316±0.002	-0.726±0.002	1.042±0.002
	366.9	0.201±0.003	-0.881±0.002	1.082±0.002

For the heating period, there is a linear relationship with slope $k=-0.48\pm0.26$ and coefficient of determination $R^2=0.9982$.

For the cooling period, the linear fitting gives $k=-0.21\pm0.10$ with $R^2=0.9427$.

Chapter 4. Unexpected observation of possible rhombohedral polar nanoregions in tetragonal barium titanate nanocrystals at room temperature

The BCDI experiments on BTO nanocrystals were done at APS 34-ID-C in both June, 2016 and April, 2019. Taking the advantage of the clear facets in appearing in some of the images of single-crystal nanoparticles, the full set crystallographic directions can be retrieved from the final reconstructed image. By mapping out the displacement field and proper mathematic derivations, some unexpected (111)-oriented 3D stripe networks have been discovered. These stripes are understood as internal boundaries within the crystal, which are confirmed by simulations. The possibility of 90° domain walls is ruled out in this case, because of the specific Bragg reflection chosen. We therefore explain these strain stripe networks as rhombohedral polar nanoregions (PNRs). This result aligns well with reports of local rhombohedral distortions in tetragonal BTO crystals, as indicated by other total scattering experiments [1-3].

4.1 Methods

The commercial 200nm Barium Titanate (BTO) nanocrystals were suspended in ethanol solution with 1% Tetraethyl Orthosilicate (TEOS) before drop-casting onto silicon wafers and calcined at 723K in air for 3h. BCDI experiments were carried out at APS beamline 34-ID-C, where the rocking curve scans were performed on the diffraction pattern at the partially overlapping 101 and 110 Bragg reflections. The measured three-dimensional (3D) diffraction patterns were inverted into real space images of the crystals, in which the phase was retrieved by a combination of error reduction (ER) and hybrid input-output (HIO) iterative algorithms [4]. The reconstructed crystal is coordinate-transformed to cubic crystallographic axes (see Appendix A) before taking the derivatives along each axis.

4.2 Discovery of (111) oriented strain stripes networks

Figure 1 is a schematic showing a BCDI experiment on BTO nanocrystals. The isolated single crystal is selected and measured by the area detector. The reconstructed crystal has at least four clear facets which are marked A to D in the figure.

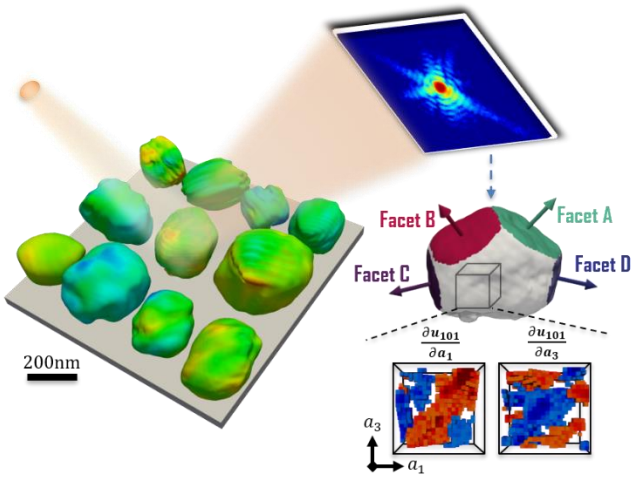

Figure 1. Schematic showing the BCDI experiment performed on BTO nanocrystals.

Figure 2(a) shows the central slice of a coherent diffraction pattern, which was measured at the 110 reflection. There are periodic fringes in all directions surrounding the diffraction centre, which contain the crystal size information in three dimensions. Several long tails of fringes can also be observed, which indicates the existence of strong surfaces or interfaces. This diffraction pattern was inverted into real space, along with advanced algorithms to retrieve the displacement field [4]. Because the rocking curve scan was measured at the 110 Bragg reflection, and not the 101 which has a slightly different position on the detector, only this Q direction is known in the final image. We note this is a good choice as it uniquely identifies the tetragonal c-axis. The missing crystallographic directions were therefore retrieved using the facets of single crystal, as described in Appendix A.

Figure 2(b) presents the reconstructed crystal image, after transformation into the orthogonal coordinate system of the crystal lattice. Three perpendicular crystallographic section views of displacement fields and their spatial derivatives are taken at the crystal centre positions, which are shown in Figure 2(c). In the displacement field map, there are small regions with different displaced values scattering around the slice. The size of these small regions spans from 10nm to 30nm, which is close the spatial resolution of our measurement. The derivatives of the displacement field are calculated along three crystallographic axes, which correspond to the linear combinations of strain tensors shown in equations below:

$$\frac{\partial u_{110}}{\partial a_1} = \frac{\partial(u_{100}\cos 45° + u_{010}\cos 45°)}{\partial a_1} = \frac{\sqrt{2}}{2}(\varepsilon_{11} + \varepsilon_{21}) \tag{4.1}$$

$$\frac{\partial u_{110}}{\partial a_2} = \frac{\partial(u_{100}\cos 45° + u_{010}\cos 45°)}{\partial a_2} = \frac{\sqrt{2}}{2}(\varepsilon_{12} + \varepsilon_{22}) \tag{4.2}$$

$$\frac{\partial u_{110}}{\partial c} = \frac{\partial(u_{100}\cos 45° + u_{010}\cos 45°)}{\partial c} = \frac{\sqrt{2}}{2}(\varepsilon_{13} + \varepsilon_{23}) \tag{4.3}$$

The derivatives of displacement over crystallographic a_1 and a_2 directions contain the sum of normal strain tensor and shear strain tensor. Shown in Figure 2(c), such displacement derivative maps display interesting networks of strain stripes. In the derivative over a_1 and a_2.(middle two columns of Fig 2(c)), the strain stripes can be seen to be 45° to all three crystallographic directions. Note from Eqs (4.1) and (4.2) that these derivatives are the sum of linear and shear strain tensors, while the displacement derivatives over c direction contain only shear. In Figure 2(c), two views of this derivative, where c-axis is in-plane, have 001 oriented strain stripes. The one view with c-axis out-of-plane still has 45° to the a_1 and a_2 axes. Animations showing the phase fields and strain stripes in three dimensions are available in Supplementary Information (SI).

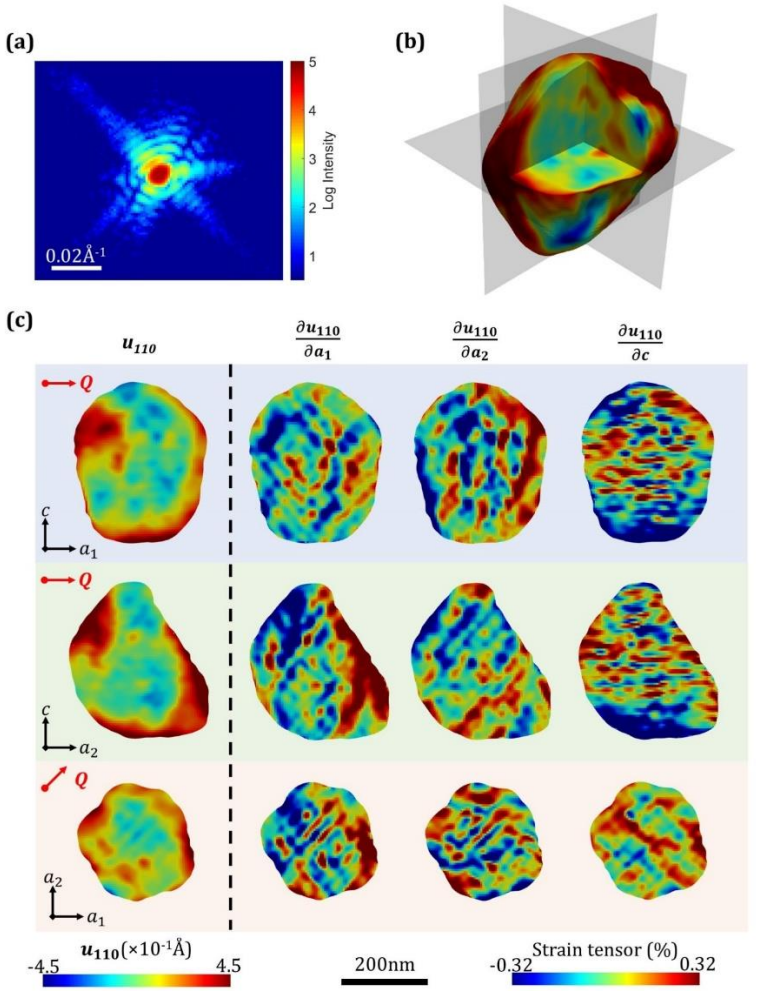

Figure 2. Coherent diffraction pattern and reconstructed images. (a) Central slice of one coherent diffraction pattern. (b) The orthogonal cut of the reconstructed crystal. The colour represents the displacement field, measured as the image phase signal. Three section views along crystallographic directions are indicated. (c) The first column presents the displacement field in three section views. The in-plane Q direction in each section views are denoted. The second to the fourth columns show the displacement derivatives along three crystallographic directions in three section views.

4.3 COMSOL simulation of domain walls

Simulations were performed to understand the origin of these strain stripe patterns. The first simulated model places a 100nm cube of material inside a 300nm cube of the same material. The thermal expansion coefficients were adjusted separately in each part of the model to introduce a strain pattern by change of temperature. The thermal expansion coefficients of the inner block were set to be $\alpha_x = \alpha_y = 0.00005$ and $\alpha_z = 0$. While for the outer shell, this thermal expansion coefficient was kept at 0C. Thermal stress was induced by setting the initial temperature to be 25C and heating the model to 300C. The inner block would expand along its x and y directions due to heating, leading to contact forces with the outer shell as shown in Figure 3(a). The external boundary of the outer block was constrained not to expand or contract upon heating.

The resulting displacement field in three directions are presented in Figure 3(b) to 3(d), which is seen to be confined to the internal domain wall boundaries of the model. The six independent strain tensors were calculated and shown in Figure 3(e) to 3(j). In the

maps of the two normal tensors ε_{11} and ε_{22}, the positions of the domain walls that experiencing thermal stress are clearly highlighted. These two strain tensors accumulated at the domain walls, and the two sides of the domain walls have opposite signs. The other four strain tensors, however, only accumulated at the vortex in slice views. The strain tensor combination in equation 4.1-4.3 were also calculated and shown in Figure 3(k) to 3(m). The two maps with normal tensors components indicated the domain wall positions properly, while the map of pure shear strain tensors only highlighted the vortex positions.

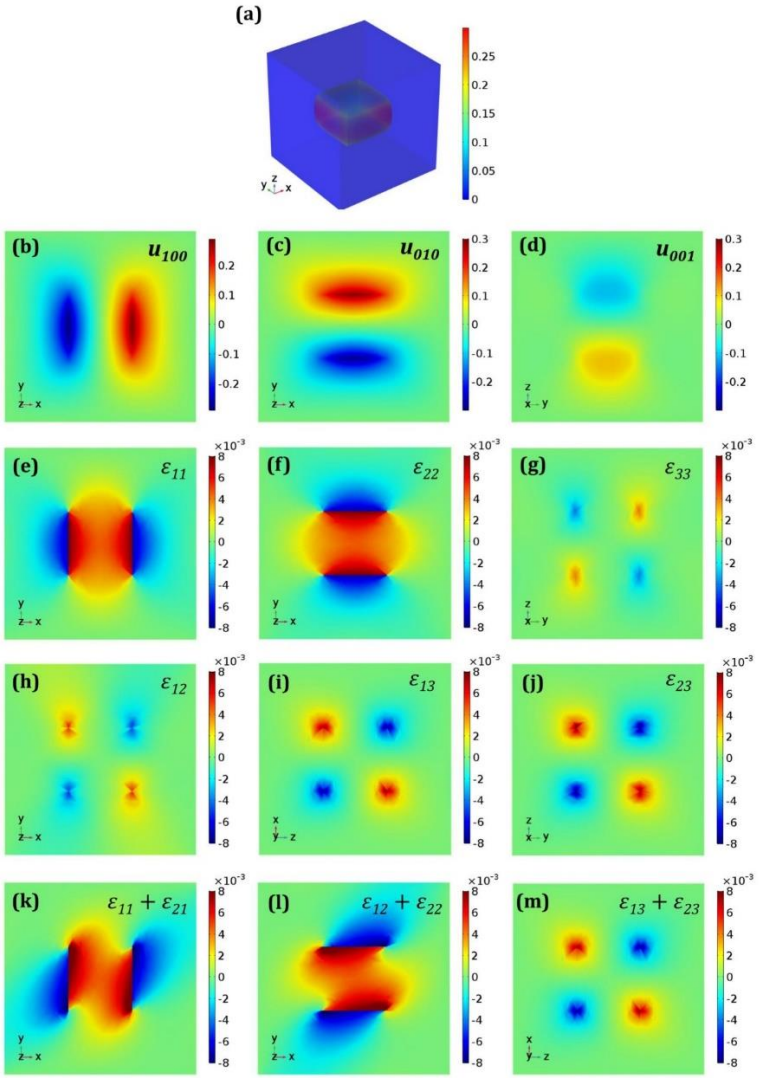

Figure 3. COMSOL simulation of a model of two cubes under thermal stress. The inner cube was 100nm in size while the outer cube was 300nm in size. The initial temperature is 0C. (a) The whole structure was heated to 300C. The inner block was expanded in x and y direction. Both blocks were coloured by the total displacement field ($u_{100}{}^2 + u_{010}{}^2 + u_{001}{}^2$) *(unit nm²). (b)-(d) The three section views of displacement field at the centre (unit nm). (e)-(j) The six independent strain tensors were calculated from the displacement map. (k)-(m) The combination of strain tensors was presented referred to Figure 2.*

4.4 Discussion

The first conclusion concerns the direction of the observed strain stripes, which guides us to understand what is their physical meaning. The simulations in Figure 3 shows that a combination of normal strain tensor and shear strain tensor allows the a_1 and a_2 derivatives to correctly identify the boundaries between regions of different strain. This suggests the strain stripes indicates there are inner boundaries, which have 45° to all the three crystallographic axes. The sum of pure shear strain tensors in simulations only show accumulations on the vertex, which corresponds to the derivatives over c axis in Figure 2. However, when the size of regions is close to the resolution, such vertex accumulations would give misleading stripes that are 45° to the real boundaries. Indeed, for the derivatives over c axis in Figure 2, the strain stripes are horizontally distributed, which is 45° to the boundaries indicated from other two derivatives. Therefore, we confirm the strain stripes been observed in Figure 1 are the inner boundaries lying at 45° to all three crystallographic axes.

The second conclusion concerns what kind of polarizations are suggested from this pattern of inner boundaries. The BTO nanocrystals studied at room temperature have tetragonal lattice system, where the 90° ferroelastic domain walls and 180° ferroelectric domain walls are normally considered to be favourable. However, because we only measured the 110 reflection of the single crystal in Figure 2, where there is no noticeable 101 twin peaks in the vicinity. This rule out the possibility of 90° domain walls [5-6]. The pure ferroelectric domain wouldn't give perpendicular stripes as shown in Figure 1. All other defects we could postulate, like dislocation arrays, were found to have different fingerprints, so are also ruled out as explanations.

We suppose the stripes in Figure 2 are the boundaries of the polar nanoregions (PNRs). The idea of PNRs are well-documented in relaxor ferroelectrics, where different models using PNRs have successfully explain the exotic frequency-dependent properties of the relaxors [7-9]. The definitions of PNRs are diverse for different systems and treated on case-to-case basis. For example, PNRs are defined in paraelectric $SrTiO_3$ thin film (STO) to be the small regions with local polarization and observed by high angle annular dark field scanning transmission electron microscope (HAADF-STEM) [10]. We propose the PNRs in this work are the small regions with tens of nanometers in size and have a {111} local polarization, which is the direction of inner boundaries we see in the experiment.

There are different scientific languages to explain the origin of the electric polarizations, such as the change of Wannier function of the occupied band in quantum mechanics [11]. In the viewpoint of crystallography, the polarization involves the displacement of barium and titanium cation relative to the oxygen. For barium titanate, with a tolerance factor is 1.06, the titanium cation has more space to move around in the oxygen octahedron. Therefore, the movement of titanium can be used to characterize the polarization in the unit cell level. Although both displacive and order-disorder features are observed in BTO, but in either case, the displacement direction of titanium cation from the centre of a unit cell reflects the symmetry breaking from cubic structure. The tetragonal lattice supports 001 displacement of titanium cation, while the orthorhombic and rhombohedral lattices have 110 and 111 displacements, respectively. The observed 111 strain stripes match with the rhombohedral lattices, though the global crystal structure is tetragonal.

Total scattering studies of BTO have revealed that the local structure of BTO is rhombohedral in all phases [1-3]. Such a conclusion usually stands at odds with the

conventional HAADF-STEM images of BTO thin film, where the Titanium cation is displaced along 001 direction instead of 111 [12]. However, the conventional STEM images are only projection views or surface views, which does resolve the structure in three dimensions. There are recent works using different techniques to confirm the existence of local rhombohedral nanostructures inside BTO single crystals [13]. The strain stripes showed in this work reveal the inherent 111 inner boundaries inside BTO nanocrystals. This support the local symmetry to be rhombohedral inside crystal and in three dimensions.

4.5 Future experiments

The temperature-dependent total scattering experiment on the 200nm BTO nanocrystals is underway at the Advanced Photon Source (APS) beamline 11-BM. The plan is to import the BCDI data into the atomic model and using Debye scattering equation to fit the scattering data and revise the atomic model back and forth.

The time-dependent BCDI experiments could also help to understand the behaviour of strain stripes when passing through phase transitions. The same experiment was carried out at the Diamond Light Source (DLS) beamline I13-1. However, the data quality was not good enough to resolve the strain stripes.

Appendix

A. Crystallographic realignment of the reconstructed crystals

For a typical powder sample, all the grains (nanocrystals) are randomly distributed so that the X-ray beam could hit more than one crystal at a time. One might consider making the X-ray beam size close to the sample crystal size and carefully aligning a specific crystal grain into the centre position. By keeping this crystal at the beam centre and searching at reciprocal space, different Bragg reflections from a single crystal can be achieved. Experimentally, however, it's more efficient to measure only one Bragg reflection of the ensemble of crystals naturally available in a powder sample. In such cases, without a secondary reference reflection, the crystallographic orientations are unknown. The only preserved direction is that of the the Q-vector, which is determined by the X-ray incident and diffracted direction in experiment and denote the corresponding crystallographic Bragg reflection.

To retrieve the correct crystallographic axes in the final 3D image, further information is required. In this work, we manage to get this additional information by identifying and calibrating the angles between the facets of the crystal morphology. Figure S1 (a) to (c) shows three orthogonal views of the crystal in laboratory coordinates. Several flat facets are observed and labelled A, B, C and D, as shown in Figure S1 (d) and (e). The Q vector is also plotted, which is the known crystallographic 110 direction.

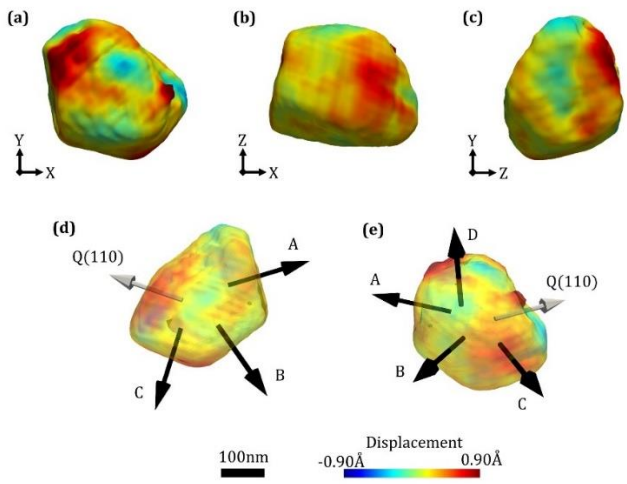

Figure S1. Different views of crystal show clear facets. (a)-(c) Three orthogonal views of the crystal shape in laboratory coordinates of the experiment. (d)-(e) The facets are marked with black arrows, while the Q vector is denoted by grey arrow.

In a single crystal, because of the symmetry of unit cells, there are fewest surface defects along "low-index" directions and these tend to show the largest facets in the crystal morphology. From low temperature to high temperature, BTO has rhombohedral, orthorhombic, tetragonal and cubic structure, respectively. All these crystal structures tend to have pseudo cubic {100}, {110} and {111} facets. To determine the facet coordinates, the three-dimensional direction matrix between these facets are mapped out and shown in Table S1. The reference angle between pseudo cubic {100}, {110} and {111} are also presented.

Table S1. Direction matrix between different facets and crystal planes.

	A	B	C	D	Q	{100}	{110}	{111}
A		109.00°	54.39°	90.56°	35.60°	-	-	-
B	-		54.65°	90.37°	144.59°	-	-	-
C	-	-		89.04°	89.98°	-	-	-
D	-	-	-		90.52°	-	-	-
Q	-	-	-	-		-	-	-
{100}	-	-	-	-	-	90.00°	45.00°/90.00°/135.00°	54.74°/125.26°
{110}	-	-	-	-	-	-	60.00°/90.00°/120°	35.26°/90.00°/144.74°
{111}	-	-	-	-	-	-	-	70.53°/109.47°

Because the Q direction is exactly 110, facet A and B have the reference angle with Q between {111} and {110}. Facet C has characteristic angle with A and B between {111} and {100}. If the facet A is marked as 111, then facet B, C, D can be identified as -1-11, 001 and 1-10, respectively.

After identifying the crystallographic direction of each facet, the rotational relation between the laboratory coordinates and crystallographic coordinates can be determined. Mathematically, there are a few matrices can represent such relations: rotational matrix, Euler angle, homogeneous transformation matrix and quaternion. In this case, the Euler angle was first calculated for coordinate transformation. Then the data in rec file with laboratory coordinates was loaded and performed coordinate transformed before saved into vtk file and visualized by paraview. The scripts to calculate the directional relation between planes and to do coordinate transformation are available upon request.

Reference

[1] Keen, D. A., & Goodwin, A. L. (2015). The crystallography of correlated disorder. Nature, 521(7552), 303–309. https://doi.org/10.1038/nature14453

[2] Senn, M. S., Keen, D. A., Lucas, T. C. A., Hriljac, J. A., & Goodwin, A. L. (2016). Emergence of Long-Range Order in BaTiO3 from Local Symmetry-Breaking Distortions. Physical Review Letters, 116(20), 1–5. https://doi.org/10.1103/PhysRevLett.116.207602

[3] Neilson, J. R., & McQueen, T. M. (2015). Representational analysis of extended disorder in atomistic ensembles derived from total scattering data. Journal of Applied Crystallography, 48, 1560–1572. https://doi.org/10.1107/S1600576715016404

[4] Fienup, J. R., Appl. Opt. (1982). Phase retrieval algorithms: a comparison, 21, 2758-2769. https://doi.org/10.1364/AO.21.002758

[5] Aranda, M. A. G., Berenguer, F., Bean, R. J., Shi, X., Xiong, G., Collins, S. P., … Robinson, I. K. (2010). Coherent X-ray diffraction investigation of twinned microcrystals. Journal of Synchrotron Radiation, 17(6), 751–760. https://doi.org/10.1107/S0909049510039774

[6] Diao, J., Shi, X., Assefa, T. A., Wu, L., Suzana, A. F., Nunes, D. S., Batey, D., Cipiccia, S., Rau C., Harder, R., Cha, W. & Robinson, I.K. (2020). Evolution of ferroelastic domain walls during phase transitions in barium titanate nanoparticles, Physical Review Materials, 4, 106001. https://doi.org/10.1103/PhysRevMaterials.4.106001

[7] Eremenko, M., Krayzman, V., Bosak, A., Playford, H. Y., Chapman, K. W., Woicik, J. C., … Levin, I. (2019). Local atomic order and hierarchical polar nanoregions in a classical relaxor ferroelectric. Nature Communications, 10(1). https://doi.org/10.1038/s41467-019-10665-4

[8] Fu, D., Taniguchi, H., Itoh, M., Koshihara, S., Yamamoto, N., & Mori, S. (2009). Relaxor Pb ð Mg 1 = 3 Nb 2 = 3 Þ O 3 : A Ferroelectric with Multiple Inhomogeneities, 207601(November), 2–5. https://doi.org/10.1103/PhysRevLett.103.207601

[9] Li, F., Zhang, S., Yang, T., Xu, Z., Zhang, N., Liu, G., … Chen, L. Q. (2016). The origin of ultrahigh piezoelectricity in relaxor-ferroelectric solid solution crystals. Nature Communications, 7, 1–9. https://doi.org/10.1038/ncomms13807

[10] Lee, D., Lu, H., Gu, Y., Choi, S. Y., Li, S. D., Ryu, S., … Eom, C. B. (2015). Emergence of room-temperature ferroelectricity at reduced dimensions. Science, 349(6254), 1314–1317. https://doi.org/10.1126/science.aaa6442

[11] Vanderbilt, D., & King-Smith, R. D. (1993). Electric polarization as a bulk quantity and its relation to surface charge. Physical Review B, 48(7), 4442–4455. https://doi.org/10.1103/PhysRevB.48.4442

[12] Jia, C. L., & Urban, K. (2004). Atomic-Resolution Measurement of Oxygen Concentration in Oxide Materials. Science, 303(5666), 2001–2004. https://doi.org/10.1126/science.1093617

[13] Tsuda, K., Yasuhara, A., & Tanaka, M. (2013). Two-dimensional mapping of polarizations of rhombohedral nanostructures in the tetragonal phase of BaTiO3 by the combined use of the scanning transmission electron microscopy and convergent-beam electron diffraction methods. Applied Physics Letters, 103(8), 1–5. https://doi.org/10.1063/1.4819221

Chapter 5. Future plan

5.1 BTO nanocrystal

As summarised in Chapter 3 and 4, we have been using BCDI to study the inner domain structures of BTO nanocrystals. We have shown that BCDI is applicable of imaging the ferroelastic domain walls and qualitatively study the changes in strain tensor between adjacent domains upon phase transition. We also found interesting stripe domains in a few tetragonal nanocrystals.

In the future works, we would like to explore the nature and behaviour of these stripe domains:

1. We need to develop a more comprehensive simulation to explain the stripe domain structures using COMSOL. We have been using thermal expansion model to simulate the domain structures and would like to extend to electrical charge model instead. The suggestion of a network of rhombohedral domain distortions can be tested with models.
2. We would want to see the behaviour of these stripe domains across tetragonal-cubic phase transition. We have conducted a 5-day experiment at ESRF ID01 in Apr. 2021, in which four crystals were tracked while crossing the tetragonal-cubic phase transition back and forth. Four crystals have two different shape changes in rocking curve scan across phase transition and we have seen stripe domains in at least one of the crystals as shown in Figure 5.1. We are still analysing the data so far and plan to turn these findings into publication.

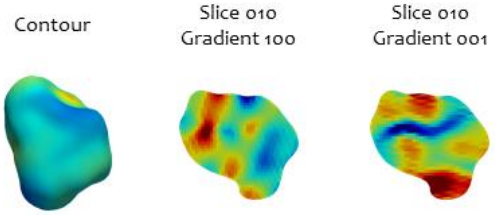

Figure 5.1 BCDI reconstruction of one BTO nanocrystal at 110°C.

5.2 BTO thin film

During the pandemic shutdown, I have been working in the lab of Prof Pavlo Zubko to learn how to prepare epitaxial BTO films in different strain states using a radio frequency sputtering system. With the strain films ready, we would like to carry out several studies:

1. Studying the changes of lattice constant across critical thickness. One of our colleagues has developed the code to accurately measuring the lattice constant from thin film or single crystal. The procedure involves measuring and refinement of 4 sets of symmetric reciprocal lattice points. We are interesting to see the lattice changes around the critical thickness of the films, where the clamping of epitaxial films starts to relax.
2. Mapping out the domain structure in BTO thin film by piezo forece microscopy (PFM) and X-ray ptychography. The phase diagram of misfit strain versus temperature has already been predicted by simulations and verified by multiple works. We would like to check the domain structures in the prepared thin films, comparing the structure difference caused by strain and thickness variations. This can be reached by conducting PFM available at LCN or a ptychography experiment at synchrotron.

3. Mapping out the strain of BTO blocks from different strain states. We plan to use RIE etching to prepare BTO blocks of different sizes and strain states as shown in Figure 5.2. Then we would use BCDI to map out the strains in different blocks. We would be interesting to see if there are any interesting domain structure within each block, but comparing different strain blocks is already an interesting result.

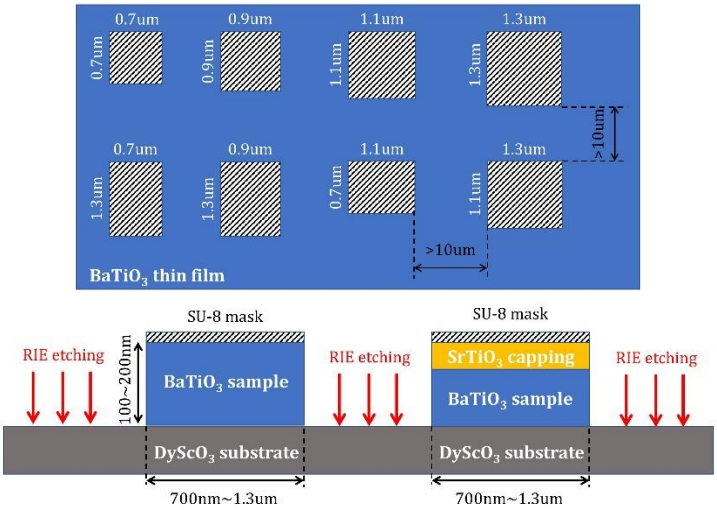

Figure 5.2 RIE etching of BTO blocks.

4. Exploring vortex structures in BTO sandwich structure. There are multiple works reporting regular distributed vortices in PTO//STO superlattice. We understand the Ti-based perovskite films are very different in their properties and behaviours, but potentially there is a chance to make BTO vortices with current condition. We plan to make STO//BTO//STO//SRO//XXX (XXX: STO, DSO, KTO, NSO) films. By varying the thickness of the BTO layers, we hope to discover some vortices in BTO systems.

5.3 Other collaboration works

1. Diamond I13-1 BCDI experiment on halide perovskite.
   We are collaborating with Sam's group in Cambridge and helping with the BCDI experiment on Halide perovskite. We have joined a previous beamtime experiment on Apr. 2021 and done the data analysis part. In one crystal, we found the crystal volume shrinkage upon time as shown in Figure 5.3, which is likely due to radiation damage.

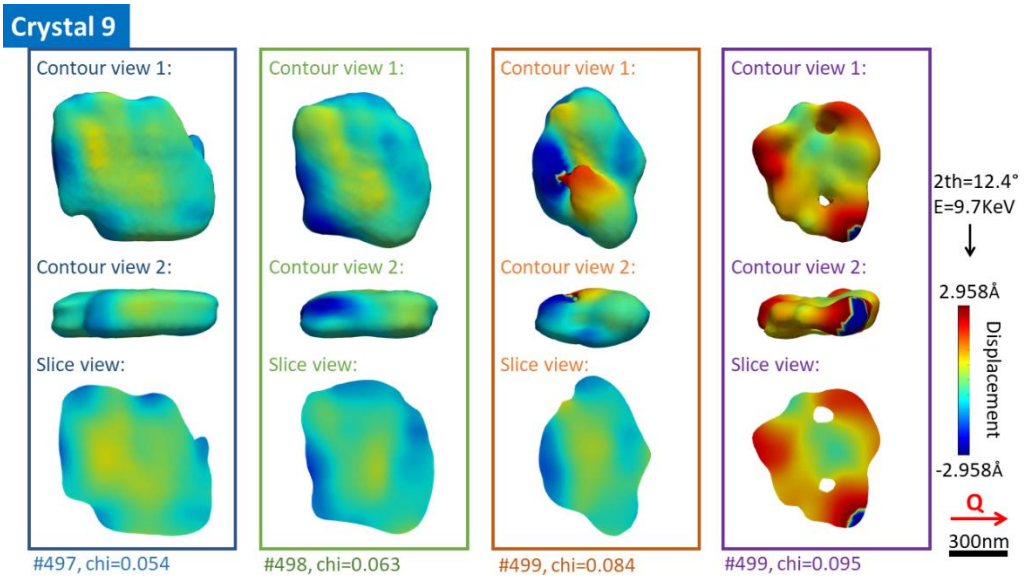

Figure 5.3 The evolution of strain within a $MAPbBr_3$ microcrystal.

We have done another in-situ BCDI experiment on Aug. 2021 at DLS I13-1 and we are currently dealing with the data analysis.

2. Hamburg XFEL XPCS experiment on LSCO superconductors, PMN relaxors and BTO thin films.
   We have done XPCS experiment on Aug. 2019 and Feb. 2020 to study the domain fluctuations in LSCO thin film at soft vibration mode near phase transition. We have an allocated beam time at XFEL on Nov. 2021 to study the fluctuating PNRs in PMN relaxors. There is a chance to look at BTO thin films if we had interesting vortices structure in as prepared films.
3. Diamond I13-1 and APS 34-ID-C BCDI experiment on battery
   We have been helping Paul Shearing's group at UCL to do BCDI on NMC nanocrystal in operando conditions. The experiment in 2019 has been published. We are still dealing with the data from Dec. 2020 at DLS and Jul. 2021 at APS, which have not been published yet.
4. Helping to restore BCDI at Diamond I16. We have a schedule beamtime from Sept.29th to Oct.5th at DLS I16 to do this. It will also be an introduction for the Zubko group to learn the capabilities of I-16 and plan future activities.

5.4 Time justification for the work

Although the work load seems too much for the last year of PhD, but the section 6.1 we have completed the experimental part. We have data analysis to do and try to form some results if possible. The main experimental works lies in section 6.2. There is no guarantee we could make good films and I will need to stop growing films at some point to finish the PhD thesis and find a postdoc position by Oct 2022. The collaboration works in section 6.3 are mainly helping others BCDI data analysis. It's always enjoyable for me to see diffraction patterns from different samples. I will try to carry on with it during free time.